SCUOLA DI DOTTORATO

UNIVERSITÀ DEGLI STUDI DI MILANO-BICOCCA

Department of Physics

PhD program in Physics Cycle XXXV

Development of a Sampling Calorimeter for the LHCb Upgrade

Surname: Martinazzoli Name: Loris

Registration number: 795652

Tutor: Prof. Marco Paganoni

Supervisor: Dr. Etiennette Auffray

Coordinator: Prof. Stefano Ragazzi

ACADEMIC YEAR 2021/2022

Riassunto

Dal 2008 il Large Hadron Collider (LHC) al CERN di Ginevra offre un contesto ideale per testare la conoscenza scientifica delle interazioni fondamentali. Ivi locato, l'esperimento LHCb esegue misure di precisione di violazione della simmetria CP e decadimenti rari degli adroni B.

LHCb verrà aggiornato per operare ad una luminosità di 1.5x10^{34} $cm^{-2}s^{-1}$. Ciò richiederà una modifica sostanziale del suo calorimetro elettromagnetico a causa delle alte dosi di radiazione nella sua regione centrale e dell'incremento del flusso di particelle.

Questa tesi di dottorato presenta una soluzione innovativa al problema, basata su calorimetri a spaghetti. Gli scintillatori candidati includono cristalli inorganici di granato, resistenti alle radiazioni per la regione a massima dose, e scintillatori organici basati su polistirene o siliconi.

La ricerca e sviluppo sui materiali scintillanti ha portato ad individuare dei granati resistenti fino a 1 MGy di dose di radiazione e con performance temporali vicine a quelle dei cristalli di LYSO:Ce. Si è poi studiata la loro composizione chimica per ridurre il loro tempo di decadimento al livello degli scintillatori plastici, pur mantenendo performance temporali competitive. Inoltre, dei campioni di scintillatori siliconici sono stati testati, ottenendo risultati promettenti.

Molteplici prototipi di calorimetro con assorbitore in piombo o tungsteno sono stati prodotti e testati nelle strutture di test su fascio a DESY e al CERN. Le risoluzioni energetiche ottenute hanno dei contributi stocastici e costanti pari a $\sim 10\%/\sqrt{E} \oplus 1\%$, al livello degli attuali moduli di LHCb. Le risoluzioni spaziali sono scese al di sotto di 1 mm, mentre le temporali hanno raggiunto i 15 ps ad alte energie. Inoltre, si è studiata la risoluzione temporale in diverse configurazioni con svariati PMT accoppiati agli scintillatori in contatto diretto o con una guida di luce, con o senza accoppiamenti ottici.

Un codice di simulazione Monte Carlo è stato sviluppato, validato con i risultati di test su fascio ed infine utilizzato per l'ottimizzazione dei prototipi. Il punto focale del codice è l'uso di un approccio ibrido alla simulazione dei fotoni ottici che mantiene

la precisione di una simulazione raytracing ma riduce il tempo computazionale di vari ordini di grandezza. Il codice è stato poi utilizzato per studiare la perdita di risoluzione temporale di uno SPACAL con assorbitore di tungsteno e cristalli inorganici scintillanti a causa del fondo atteso ad LHCb. Ciò ha permesso di decidere la direzione dello sviluppo futuro degli scintillatori.

Abstract

Since 2008 the Large Hadron Collider (LHC) at CERN, Geneva, has offered the ideal testing ground to probe the scientific knowledge of the fundamental interactions. There, the LHCb experiment performs precision measurements of CP violation and rare decays of B hadrons.

LHCb will be upgraded to run at a luminosity of 1.5x10^{34} cm^{-2}s^{-1}. This will require a substantial modification of its current electromagnetic calorimeter due to high radiation doses in the central region and increased particle densities.

This PhD thesis presents an innovative technological solution based on spaghetti calorimeters (SPACAL). The candidate scintillators include both radiation-hard inorganic crystal garnets, for the region with the highest radiation dose, and organic dyes in polystyrene or polysiloxane hosts.

The R&D on scintillating materials individuated garnets radiation-hard up to 1 MGy with timing capabilities close to LYSO:Ce. Their composition was then tuned to reduce their decay time at the level of plastic scintillators, keeping competitive timing. Samples of polysiloxane scintillators were tested with promising results.

Prototypes of SPACAL with lead or tungsten absorbers were produced and tested at DESY and CERN. The energy resolutions showed sampling and constant contributions of $\sim$ 10%/$\sqrt{E} \oplus$ 1% in line with the current LHCb modules. The spatial resolutions reached below 1 mm, and time resolutions at the level of 15 ps at high energies. Moreover, time resolution was studied with several PMTs coupled to the scintillators in direct contact or via light guides, with or without optical glues.

A Monte Carlo simulation framework was developed, validated with testbeam results, and used to optimise the prototypes. It relies on a hybrid approach to describe the transport of the optical photons, retaining the precision of ray tracing but reducing by orders of magnitude the computation time. The framework was employed to study the deterioration caused by the LHCb background to the time resolution of a SPACAL with tungsten absorber and inorganic crystals, giving further input to the scintillators R&D.

Contents

Part I

Introduction

Chapter 1

Ouverture

Quantum mechanics has changed dramatically our understanding of the laws of nature over the last century. The astounding scientific progress experienced was made possible by the interplay between new theoretical ideas and precise experimental data. In the field of fundamental interactions, the joint effort of the scientific community culminated with the Standard Model, the most complete description to date of the electromagnetic, weak, and strong forces.

Nonetheless, crucial questions remain unanswered. One such is the imbalance between matter and antimatter: the Standard Model cannot explain the abundance of former over the latter in the Universe. The Large Hadron Collider (LHC) at CERN produces proton-proton collisions at the highest energy ever reached by man. There, the LHCb experiment seeks hints of new physics via measurements of CP violation with unparalleled precision.

Higher precision means more data. Increasing the rate of collisions is the strategy to harvest those data and to improve the potential for the discovery of new physics. However, it entails technological challenges to discern in the flux of particles valuable signals from the background. To this purpose, LHCb must be upgraded, and an appropriate design of all its subdetectors is key to the future success of the experiment.

This PhD thesis is dedicated to the development of innovative solutions for the future upgrade of the LHCb electromagnetic calorimeter. The proposal is a spaghetti calorimeter (SPACAL), made of a dense absorber in which are inserted scintillating fibres.

The manuscript is divided as follows:

- Part I introduces the field of Calorimetry and discusses the upgrade plan of the LHCb detector;

- Part II presents the research on scintillators, starting with the current state of the art and the development of new compositions suiting the needs of LHCb;
- Part III shows the design, assembly, and testing of the prototypes. First, it focuses on achieving the best performance, then on compromising the minimum to reach a sustainable layout for the upgrade;
- Part IV describes the development and use of the Monte Carlo simulation software to understand the experimental observations, to predict the performance in the environment of the LHCb upgrade, and to propose further optimisation.
- Part V draws the conclusions and discusses the next steps.

The goal of this study is to prove the realism of an idea: a calorimeter resistant to extreme radiation environments, able to detect particles with a precision of a few tens of picoseconds, delivering the same performance of the current LHCb one. It lays the groundwork upon which starts the design and the optimisation of the detector that will keep the collaboration busy for the next years.

Chapter 2

Calorimetry

Calorimeters are detectors primarily designed to measure the energy of an incident particle. Traditionally, they consist of blocks of instrumented material in which particles are fully absorbed and their energy is converted into a measurable quantity. Calorimeters are sensitive to both charged and neutral particles, and can provide indirect detection of neutrinos via missing energy. Their energy resolution improves with the incident particle energy, in contrast with magnetic spectrometers [1, 2].

Calorimeters are divided by technology into sampling and homogeneous.

Sampling calorimeters comprise alternating layers of passive and active material. The passive material is dense and with large atomic number Z to maximise stopping power, whereas the active material samples the energy deposition. Examples are KLOE Lead/Scintillator fibres, ATLAS liquid Argon, or CMS hadron calorimeters [3, 4, 5].

Homogeneous calorimeters are entirely made of active material. This removes the sampling fluctuations and offers the best energy resolution, however at the expense of compactness and, ultimately, cost. Examples are the L3 BGO and CMS $PbWO_4$ calorimeters [6, 7].

Electron and photons interact with matter in a very different way than hadrons. For this reason, calorimeters are often longitudinally-segmented into an electromagnetic (ECAL) and a hadronic (HCAL) part. Such division allows optimising the two independently – e.g. homogeneous ECAL and sampling HCAL – However, segmenting a calorimeter can complicate its use, as discussed in Sec. 2.3 and in [8, 2].

All technologies come with strengths and weaknesses. Therefore, the calorimeter must be designed according to a clear physics case in harmony with the rest of the experiment.

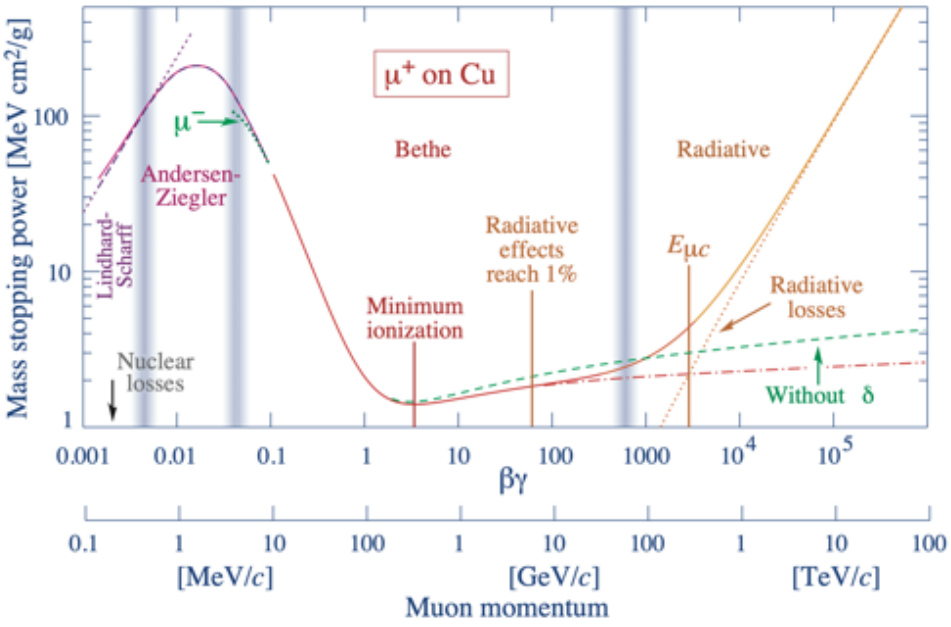

FIGURE 2.1: Mass stopping power $\langle dE/dx \rangle$ for μ^+ in copper. From reference [9].

The focus of this thesis is on electromagnetic calorimetry. The next sections provide an overview of the necessary physics to understand this thesis. Extensive reviews of both electromagnetic and hadronic calorimetry can be found in [2, 1, 9]

2.1 Radiation-Matter Interaction

2.1.1 Charged particles

Charged particles ionise the medium in which they travel. The mean energy loss per unit of distance is described by the Bethe-Bloch formula (Fig. 2.1):

$$\langle -\frac{dE}{dx} \rangle = Kz^2 \frac{Z}{A} \frac{1}{\beta^2} \left[\frac{1}{2} \ln \frac{2m_e c^2 \beta^2 \gamma^2 W_{max}}{I^2} - \beta^2 - \frac{\delta(\beta\gamma)}{2} \right]. \tag{2.1}$$

The particle energy is lost in single collisions. In thin materials, only a few take place, thus the energy loss distribution has large variance. The most probably energy loss differs from the mean, and it is described by the Landau-Vavilov distribution. [9]

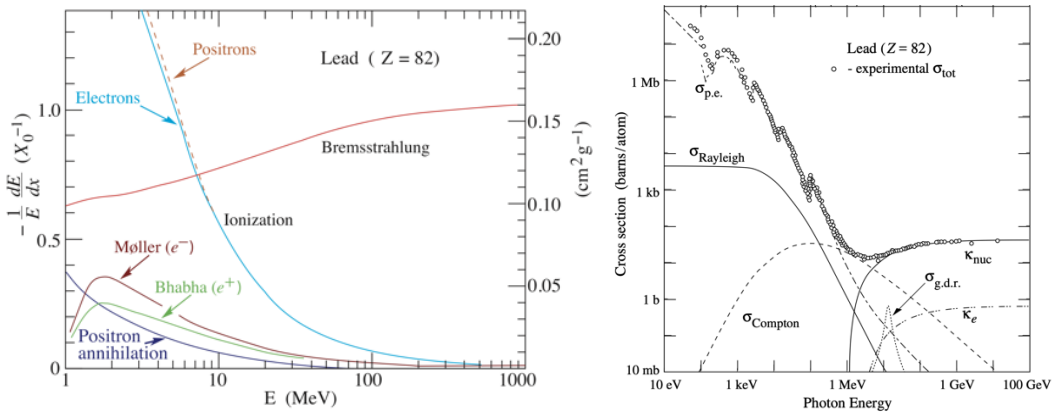

FIGURE 2.2: Energy loss processes for electrons and positrons (left) and photons interaction cross sections (right) as function of their energy. From reference [9].

The ionisation loss for electrons differs from Eq. 2.1 due to their small mass and their indistinguishability:

$$\langle -\frac{dE}{dx} \rangle_{ion} \propto \log(E), \tag{2.2}$$

where E is the electron energy. Beyond ionisation, electrons lose energy via multiple processes, shown in Fig. 2.2. Of them, the most important is **bremmstrahlung**, i.e. photon emission by the electron accelerated in the nucleus Coulomb field. The energy loss for Bremmstrahlung increases linearly:

$$\langle -\frac{dE}{dx} \rangle_{brem} \propto E, \tag{2.3}$$

thus dominating at higher energies.

The **critical energy** ϵ_c is often defined as the energy at which the ionisation and radiation losses are equal. Rossi's definition is the energy at which the ionisation loss per radiation length X_0 equals the electron energy [10]:

$$\langle -\frac{dE}{dx} \rangle_{ion} X_0 = E. \tag{2.4}$$

The two definitions match at high energies where the ionisation losses are negligible. According to the latter definition, the critical energy can be empirically calculated as:

$$\epsilon_c = \frac{610\,\text{MeV}}{Z + 1.24} \qquad \text{for solids and liquids} \tag{2.5}$$

$$\epsilon_c = \frac{710\,\text{MeV}}{Z + 0.92} \qquad \text{for gases} \tag{2.6}$$

precise at a few percent level. It is worth noting that for a particle of mass m the critical energy is higher by $\left(\frac{m}{m_e}\right)^2$ where m_e is the electron mass. Consequently, bremmstrahlung becomes relevant at much higher energies for other particles.

2.1.2 Photons

Photons lose energy via several processes. Fig. 2.2 right shows:

$\sigma_{p.e.}$ Photoelectric effect, in which the photon is absorbed by the atom and an electron is consequently ejected carrying the excess kinetic energy;

$\sigma_{Rayleigh}$ Rayleigh coherent scattering, in which the photon changes direction scattering elastically;

$\sigma_{Compton}$ Compton scattering, in which the photon changes direction scattering on an electron, yielding part of its energy;

k_{nuc}, k_e Pair production on nuclei or electrons, in which the photon produces an electron-positron e^-e^+ pair;

$\sigma_{g.d.r.}$ Photonuclear interactions leading to the breaking of the nucleus.

While photoelectric effect dominates the low-end of the energy spectrum, below a few hundreds of keV, the cross section for Compton is highest between a few hundreds of keV to a few MeV, depending on the Z of the material. At higher energy, pair production cross section dominates. The total cross section can then be approximated by:

$$\sigma = \frac{7}{9}\frac{A}{X_0 N_A} \tag{2.7}$$

where N_A is the Avogadro number and X_0 the radiation length.

2.1.3 Radiation length

The radiation length emerges as the characteristic scale on which both high-energy electrons and photons lose energy: it is the average travel length for an electron to reduce its energy to $\frac{1}{e}$ and $\frac{7}{9}$ of the average travel length for a photon to produce an e^-e^+ pair. It can be parameterised as:

$$X_0 = \frac{716.4 \cdot A}{Z(Z+1) \cdot \log(287/\sqrt{Z})} \quad [\mathrm{g/cm^2}] \tag{2.8}$$

The radiation length of a chemical compound is:

$$\frac{1}{X_{0,eff}} = \sum_i \frac{m_i}{X_{0,i}}, \tag{2.9}$$

where m_i and $X_{0,i}$ are the fraction by mass and the radiation length of the i-th element, while for an object made of several materials:

$$\frac{1}{X_{0,eff}} = \sum_i \frac{V_i}{X_{0,i}}, \tag{2.10}$$

where V_i and $X_{0,i}$ are the fraction by volume and the radiation length of the i-th material.

2.2 Electromagnetic Showers

Energetic particles lose energy in matter producing a cascade of secondaries, called shower.

High-energy electrons and positrons lose energy by producing photons, while photons by producing electron-positron pairs. This circular relation generates electromagnetic showers[1].

Since the radiation length and the critical energy depend on the properties of the material in which the particles travel, so does the development of an electromagnetic shower.

[1] Hadronic showers, instead, differ in physics processes and secondaries composition due to nuclear interactions. They include electromagnetic showers due to decays like $\pi^0 \to \gamma\gamma$. However, part of the energy carried by hadrons is either invisible to the detector, e.g. nuclear breakup energy, or delayed, e.g. if carried by neutrons. The fraction of energy deposited via electromagnetic shower f_{em} fluctuates from 0 to 1 on an event-by-event basis, leading to energy misestimation. The measurement of f_{em} for each event constitutes the modern problem of hadronic calorimetry (see for instance [11]).

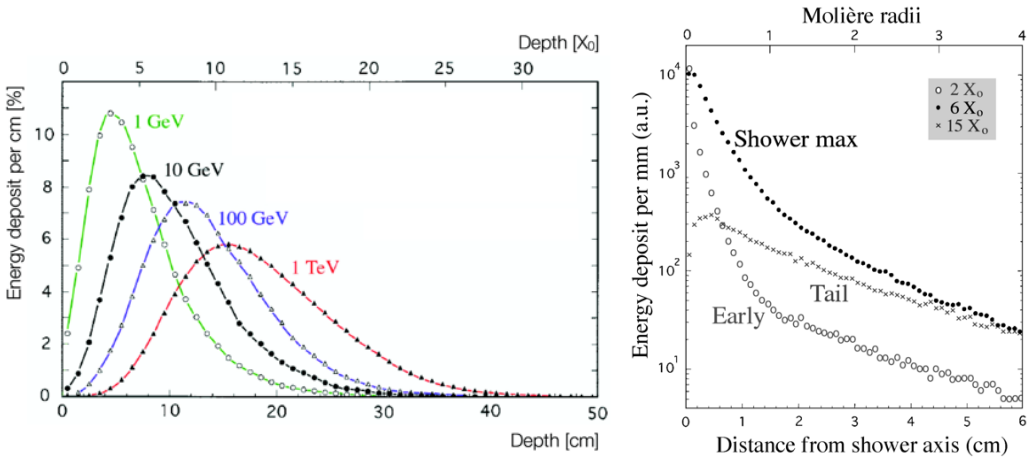

FIGURE 2.3: Left: longitudinal shower profile for electron showers in copper at different energies. The vertical axis gives the energy deposit per cm of copper as a percentage of the energy of the showering particle. Right: radial distributions of the energy deposited by 10 GeV electron showers in copper at three depths. From reference [2].

However, in first approximation material-dependent effects can be eliminated by using the following scale variables:

$$\epsilon = \frac{E}{\epsilon_c}, \qquad t = \frac{x}{X_0}, \qquad R_M = E_s \frac{X_0}{\epsilon_c}, \tag{2.11}$$

where R_M is the Molière radius, and $E_s = m_e c^2 \sqrt{4\pi/\alpha} = 21.2$ MeV.

The longitudinal development of the shower (Fig. 2.3) is dominated by energetic particles, which propagate for several radiation lengths producing secondary particles. Eventually, their energy falls below the critical energy ϵ_c and the rest is dissipated via ionisation or Compton and photoelectric effect. An analytical description of the average longitudinal profile of energy deposition was proposed by [12]:

$$\frac{dE}{dt} = E_0 b \frac{(bt)^{a-1} e^{-bt}}{\Gamma(a)}, \tag{2.12}$$

where E_0 is the start energy. The shower maximum occurs at:

$$t_{max} = \ln \epsilon - 0.5 \qquad \text{for } e^{\pm}, \tag{2.13}$$

$$t_{max} = \ln \epsilon + 0.5 \qquad \text{for } \gamma, \tag{2.14}$$

which shows that the shower maximum penetrates deeper in the calorimeter only logarithmically with increasing energy. Note that photon-induced showers penetrate on average $1X_0$ deeper.

The scale unit for the transversal size of the shower is the Molière radius:

$$R_M = E_s \frac{X_0}{\epsilon_c} \tag{2.15}$$

where $E_s = m_e c^2 \sqrt{4\pi/\alpha} = 21.2$ MeV. The strong dependence of the radiation length on the Z is paired by the critical energy, making the Molière radius less material dependent. The Molière radius of mixtures or compounds can be computed as in Eq. 2.10 and Eq. 2.9 replacing X_0 by R_M.

Second order effects of materials beyond the scale variables are discussed in [2].

Electromagnetic showers are complex objects best described by statistical approaches. The analytical description of the average behaviour provides practical insights, however, event-by-event fluctuations constitute the performance limit of a detector and the main challenge in the development of a calorimeter. This is true in particular for irregular geometries, such as in sampling calorimeters. The electromagnetic processes are well known, and reliable Monte Carlo simulation packages like EGS4 implemented in GEANT4 exist [13]. These are essential tools for the development of calorimeters.

2.3 Measuring the Energy

Calorimeters determine the energy of incident particles by measuring the total track length T, defined as the sum of the tracks of all the charged particles in the shower, which is converted into a detectable quantity, e.g. electron-ion pairs, or Cherenkov photons. [16]

For a set of incident particles of monochromatic energy E_0, any calorimeter will output a distribution of a measurable quantity, due to its finite precision. The **calorimeter response** is defined as the average calorimeter signal divided by the energy of the particle that caused it. The calibration is the procedure to reconstruct the calorimeter response.

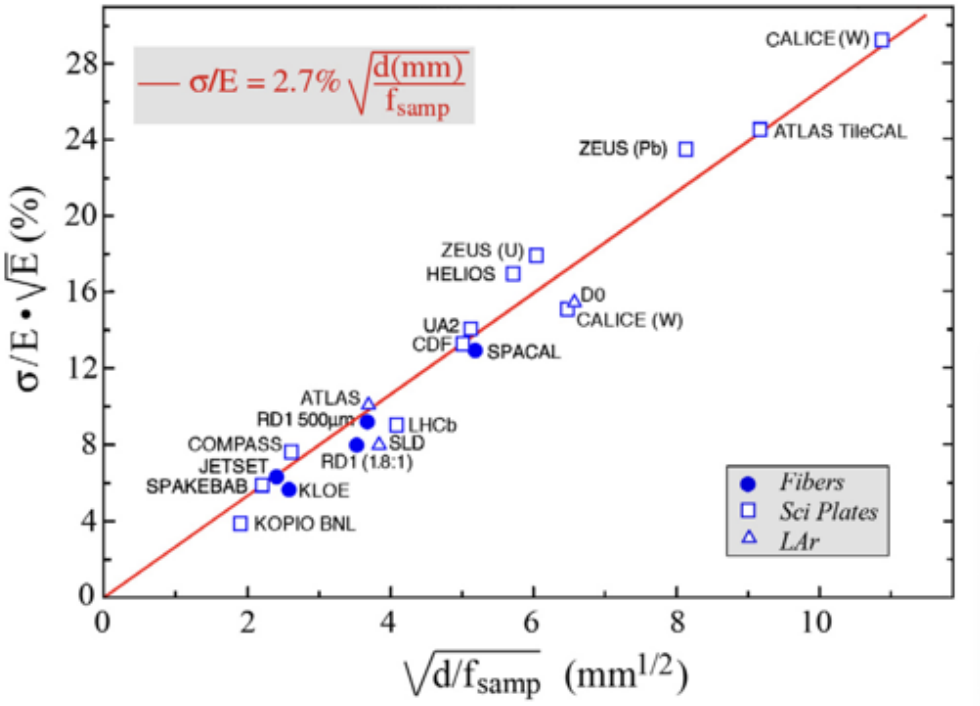

FIGURE 2.4: The sampling term of notable sampling ECALs as a function of $\sqrt{d/f_{samp}}$ (see Eq. 2.19). Energy is expressed in units of GeV. From reference [14].

Once done, it allows computing the incident particle energy with the calorimeter output information.

There are two key figure of merits of a calorimeter: **linearity** and **resolution**.

A calorimeter whose response is constant as a function of energy is said to be linear. **Linearity** is necessary to avoid systematic mismeasurements: for instance, in a non-linear calorimeter a π^0 of energy E_0 decaying $\pi^0 \rightarrow \gamma\gamma$ produces a different signal from a single γ of the same energy E_0.

Erroneous calibration can be a source of non-linearity, in particular in longitudinally-segmented calorimeters. The shower composition and the interaction of its components with the calorimeter evolve during the shower development: the tail of the shower, more than the start, features soft γ photons, whose cross-section favours the dense and high-Z materials of the absorber. As a result, the electromagnetic shower is sampled

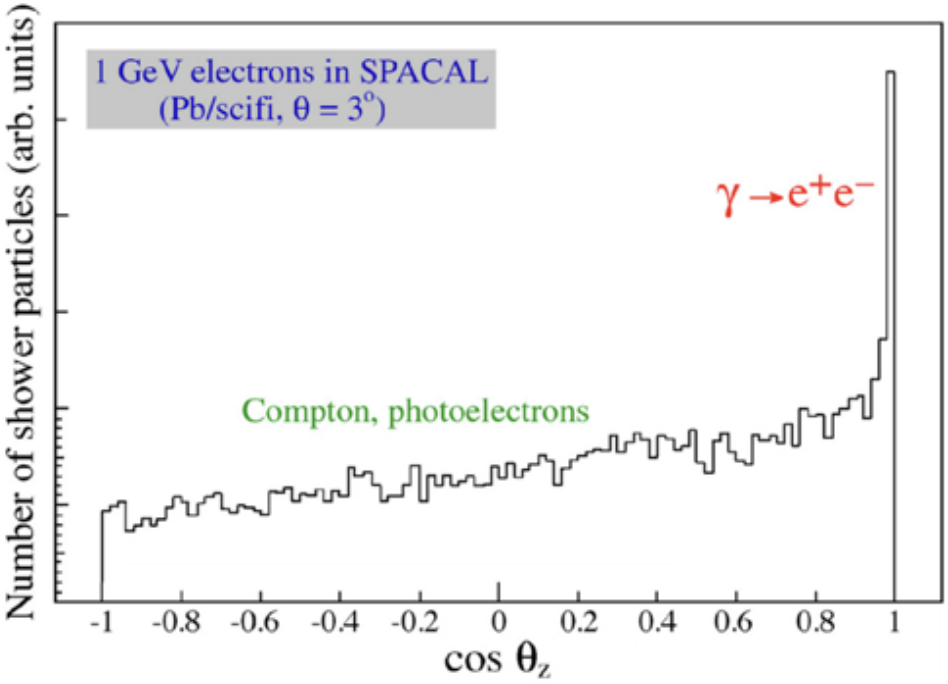

FIGURE 2.5: Distribution of cosine of the angles at which secondary particles travel in a Lead and scintillating fibres calorimeter. It demonstrated that the emission angle with respect to the shower axis is rather homogeneous. From reference [14], originally from [15].

less as it develops, and, consequently, the relationship between energy deposited and signal output differs between the longitudinal segments. Moreover, the average shower shape varies extending deeper inside the calorimeter at higher energies of the primary particle and for γ photons than for electrons. [8, 17, 18]

Non-linearity can also be due to instrumentation. PMTs have a limited dynamic range in which the produced charge is proportional to the incident number of photons; exceeding it induces space charge effects on the last dynodes, limiting the current output [19].

The **resolution** of a calorimeter is quoted as the ratio between the standard deviation and the average of the measured distribution $\frac{\sigma}{\langle E \rangle}$. It is parameterised as a function of

the true energy of the incident particle E by:

$$\frac{\sigma}{\langle E \rangle} = \frac{n}{E} \oplus \frac{s}{\sqrt{E}} \oplus c \tag{2.16}$$

where $\oplus$ is a sum in quadrature and E is in GeV.

The term n accounts for a fluctuation source independent of the particle energy. It is usually associated with the electronic **noise**: the thermal agitation of the charge carriers causes fluctuations in the electronics pulse output which are independent of the input pulse; increasing the signal improves the S/N ratio reducing its relative contribution $\propto 1/E$.

The term s is called **stochastic** or sampling and it represents statistical fluctuations like [16]:

Photostatistics : is the contribution due to production, transport, and detection of optical photons in light-based calorimeters. Photostatistics fluctuations decrease with the number of photons detected N_{pe}, and, thus, the incident particle energy, as:

$$\frac{\sigma_E}{\langle E \rangle} \propto \frac{\sigma_{N_{pe}}}{N_{pe}} \propto \frac{1}{\sqrt{N_{pe}}} \tag{2.17}$$

due to Poisson statistics [20];

Sampling fluctuations : in sampling calorimeters only a fraction of the total track length T crosses active layers. Amaldi demonstrates that [16]:

$$\frac{\sigma_E}{\langle E \rangle} \propto \sqrt{\frac{t}{E}} \tag{2.18}$$

being t the thickness of the active layer in radiation lengths. Recent approaches correct the above dependency by adding the concept of the sampling fraction f_{samp}, the ratio of active to passive material, finding [14]:

$$\frac{\sigma_E}{\langle E \rangle} \propto \sqrt{\frac{t}{f_{samp}} \cdot \frac{1}{E}} \tag{2.19}$$

Eq. 2.19 is helpful for a qualitative understanting of performance of sampling calorimeters, as shown by Fig. 2.4.

Tracklength fluctuations : particles in the shower travel at different angles, effectively experiencing different sampling fraction and frequency. Fluctuations in the angular distribution of the secondaries affect the total track length. This effect is not described by the sampling contribution of Eq. 2.19.

Landau fluctuations : the energy loss probability distribution for particles travelling through moderately thin layers is well described the highly-skewed Landau-Vavilov distribution, showing a long tail due to high-energy-transfer collisions [9]. Such Landau tail is an additional contribution in particular for gaseous detectors where it can add up to $\geq$10% [16].

The **constant** term c includes contribution that are proportional to the particle energy, like shower leakages and response non-uniformities. The former are parts of the electromagnetic shower leaking out from the calorimeter volume, either longitudinally, e.g. at the back, or transversally, e.g. outside of the volume used to reconstruct a particle energy in an experiment. Response non-uniformities can be due to miscalibration of channels, inhomogeneities in the light transport efficiency of a scintillator, or mechanical imperfections. It is the dominant component at high energy, and it is typically kept $\leq 1\%$.

Chapter 3

LHCb

The LHCb detector is one of the four main experiments at the Large Hadron Collider (LHC) at CERN [21]. The detector is a single-arm forward spectrometer with a bending plane (Fig. 3.1). It is designed to study flavour physics performing precise measurements of CP asymmetries and of rare decays of b and c hadrons. The experiment covers the region $2 \leq \eta \leq 5$, where the pseudorapidity η is defined as:

$$\eta = -\log\left[\tan\left(\frac{1}{2}\theta\right)\right] \tag{3.1}$$

and θ is the angle with respect to the beam axis z. The choice of a single arm is justified by the fact that the high-energy proton-proton collisions at the LHC produce b and $\bar{b}$ hadrons predominantly in the same forward cone.

LHCb was operated successfully for Run 1 and Run 2 of the LHC operation, from the first proton-proton collisions in 2009 till the end of 2018, when the Long Shutdown 2 (LS2) started. During the LS2, LHCb underwent large-scale modification, the Upgrade I. The experiment is now in its Run 3 phase with the next Long Shutdown planned for the end of 2025. Plans for future upgrades are discussed in Sec. 3.2.

LHCb is made of sub-detectors dedicated to specific tasks. They can be roughly divided into tracking and particle identification (PID). In the latter group lies the Calorimeter system.

3.1 The Calorimeter System

The LHCb Calorimeter system is designed to identify electrons, photons, and hadrons, measuring their energy and their impact position. It is a key component of the LHCb

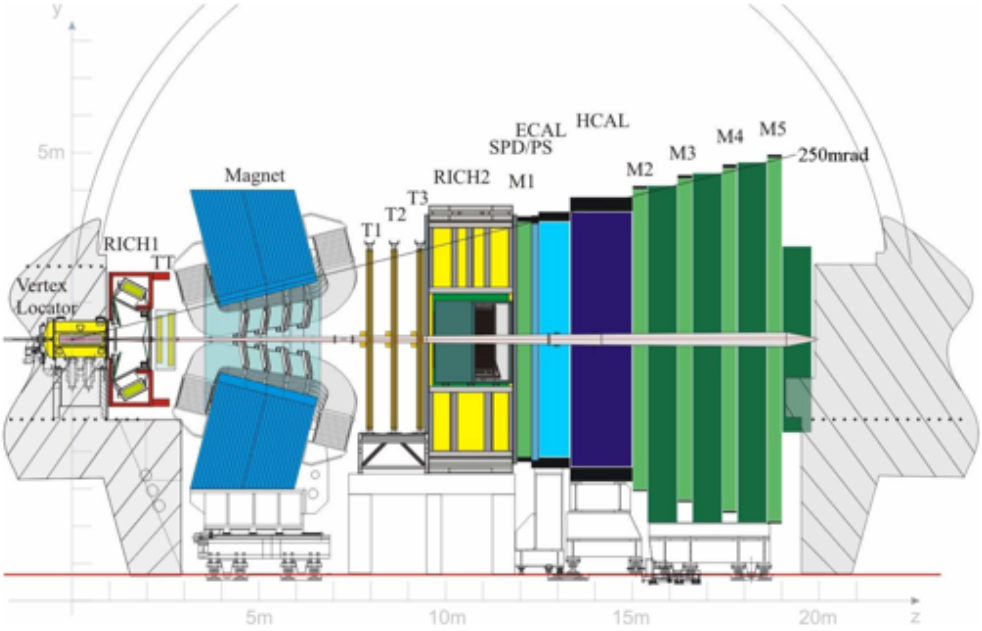

FIGURE 3.1: Schematics view of the Run 1 and 2 LHCb detector at the LHC (2009-2018). From reference [21].

PID strategy and its performance allowed high-impact studies with neutrals and electrons such as the observation of the photon polarisation in the $b \to s\gamma$ [23], the measurement of CP violation in $B^0 \to K^+\pi^0$ [24], and tests of lepton flavour universality [25].

The Calorimeter system was used in Run 1 and 2 in the first trigger level (L0) to propose online a particle type. To do so, the calorimeter was originally divided into the 4 subdetectors (Fig. 3.2, left) here described from the closest to the interaction point to the furthest:

SPD The Scintillator Pad Detector (SPD) is a wall made of scintillator pads with a WLS fibre coiled inside it (Fig. 3.2, right) and coupled to multi-anode photomultipliers (MA-PMT) Hamamatsu 5900 M64;

PS The PreShower detector (PS) is identical to the SPD wall, but placed after a 15 mm (2.5 X_0) thick Lead curtain;

ECAL The electromagnetic calorimeter consists of a sampling layout of alternating

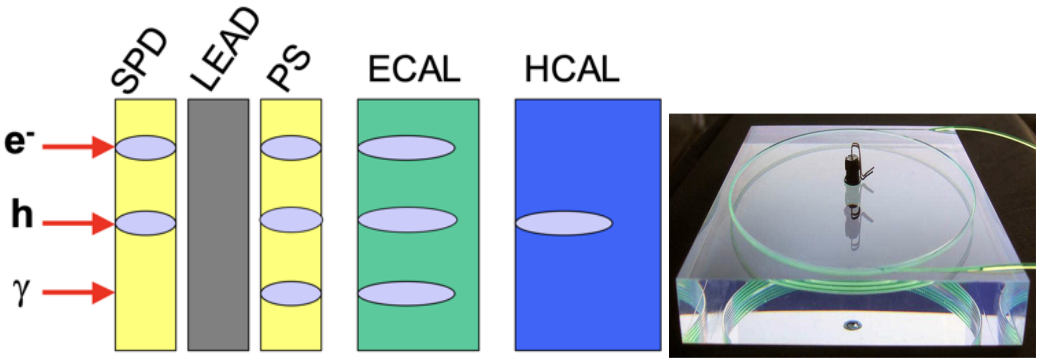

FIGURE 3.2: Left: sketch of the PID strategy of the LHCb Calorimeter system. The grey droplets represent energy deposition in a subdetector. Right: picture of a SPD/PS detector cell. From reference [22].

lead and scintillating tiles orthogonal to the beam axis called Shashlik. It is discussed later in detail.

HCAL The hadron calorimeter is a sampling device comprising iron and scintillating tiles. Unlike in a Shashlik, HCAL tiles run parallel to the beam axis. Wavelength-shifting fibres (WLS) collect and transport the light to the Hamamatsu R7899-20 PMT at the back.

During the LHC LS2, LHCb underwent its first major upgrade. Amongst many novelties, the L0 trigger was discarded. Regarding the calorimeter system, the SPD and the PS, mainly used for L0 triggering, were removed. The readout electronics was replaced [26]. The HCAL was maintained for Run 3, but its usefulness beyond LS3 is under study [27]. The ECAL emerged as the crucial component of the system for the physics case of LHCb. The rest of the section – and of the thesis as well – focuses on the ECAL.

The **LHCb ECAL** is a wall of 7.76x6.30 m^2 located 12.5 m from the interaction point. Its outer dimensions match projectively those of the tracking systems, namely $\theta_x <$ 300 mrad and $\theta_y <$ 250 mrad, while the inner acceptance is $\theta_{x,y} <$ 25 mrad.

The ECAL is made of Shashlik modules, a sampling layout alternating 4 mm thick scintillator and 2 mm thick lead tiles orthogonal to the beam axis (Fig. 3.4). The tiles are interleaved with 120 μm thick TYVEK white reflective paper. The modules are 121.2x121.2 mm^2 and 25 X_0 deep, with a Molière radius of 35 mm. The particle flux varies by two orders of magnitude over the calorimeter surface and, for this reason, the calorimeter is divided into three sections – inner (176 modules), middle (448), outer

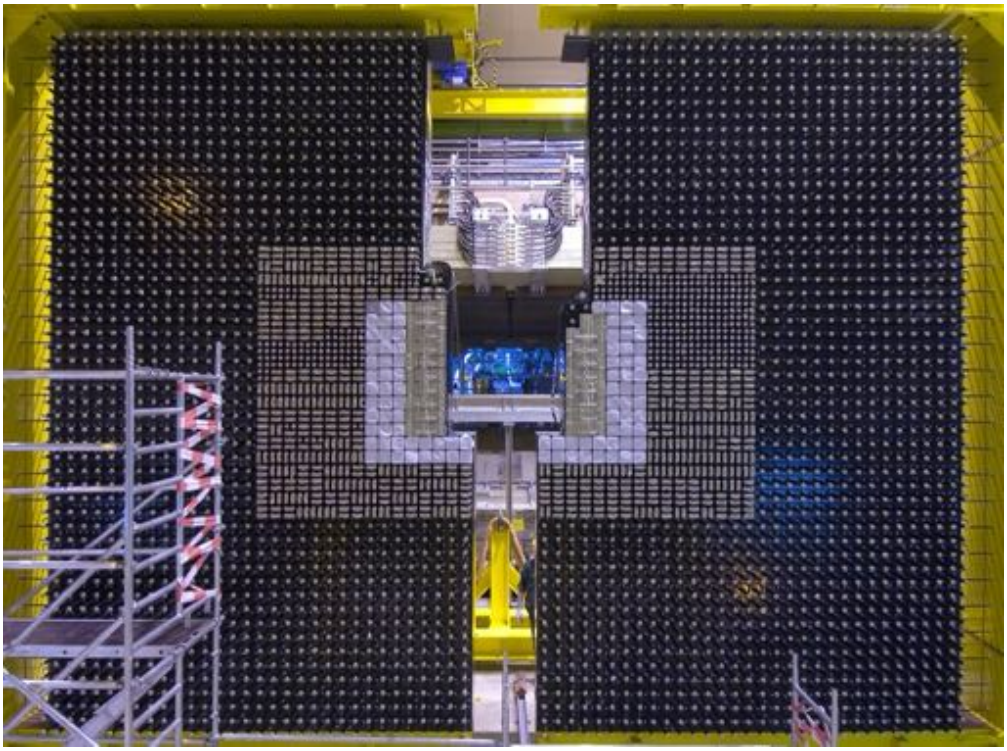

FIGURE 3.3: Picture of the LHCb ECAL from the back during the assembly, the two halves slightly separated. The 3 sections with different cell size can be distinguished by the number of PMTs per module.

(2688) – defined by the granularity of the elementary cells in a module: the inner modules are divided into 3x3 cells, the middle in 2x2, and the outer is only 1 cell. [21, 28]

The scintillating tiles are made of polystyrene doped with 2.5% PTP and 0.01% POPOP. Tile-to-tile fluctuations in light yield are below 2.5% RMS. The scintillation light is collected by 1.2 mm diameter Kuraray Y-11(250) MSJ WLS fibres running along the module to the back, where those assigned to the same cell are bundled and coupled to a Hamamatsu R7899-20 PMT via a polystyrene light mixer. The high voltage is provided to the PMT by a Cockroft-Walton base. The light output was measured being about 3000 photoelectrons/GeV. The radiation hardness was evaluated placing Shashlik modules near the beam pipe on the side of the interaction point opposite to LHCb. The study concluded that the Shashlik can remain operational till 30-40 kGy, albeit with a significant

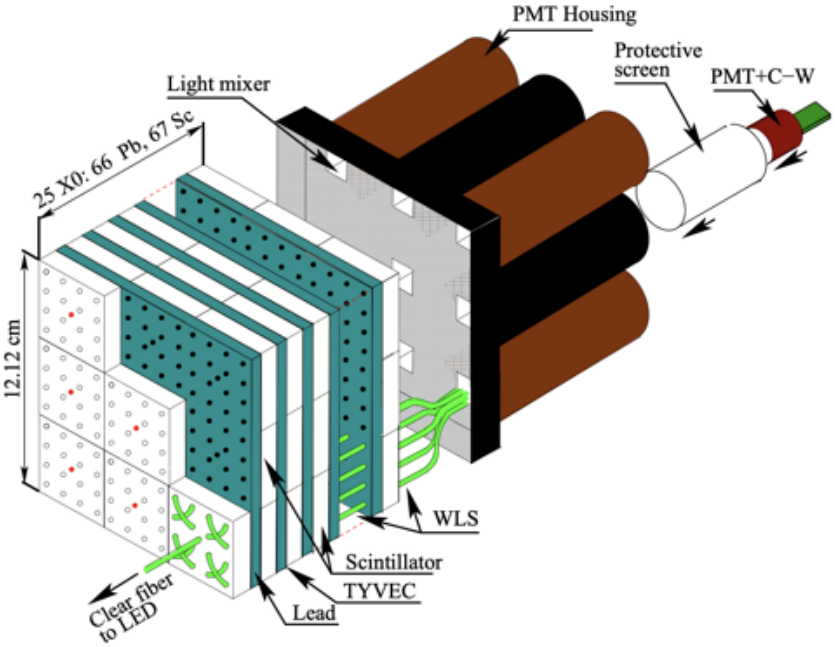

FIGURE 3.4: Schematics of a Shashlik calorimeter module, illustrating the different components. From reference [28].

reduction in light output. [29, 28, 30]

The performance of the Shashlik modules was studied in several testbeam, as in [31], with the energy resolution being [21]:

$$\frac{\sigma_E}{\langle E \rangle} = \frac{[8.5, 9.5]\%}{\sqrt{E}} \oplus \sim 0.8\%, \tag{3.2}$$

depending on the type of module. Nevertheless, several additional factors contribute to the effective energy resolution of the whole LHCb ECAL. Using electrons from converted photons, the effective ECAL resolution in Run 1 and Run 2 was [28]:

$$\frac{\sigma_E}{\langle E \rangle} = \frac{(13.5 \pm 0.7)\%}{\sqrt{E}} \oplus \frac{(0.32 \pm 0.03)}{E} \oplus (5.2 \pm 0.1)\%, \tag{3.3}$$

where the significant increase was due to reconstruction effects issues like pile-up and, in particular, the material budget in front of the ECAL, including the SPD/PS system.

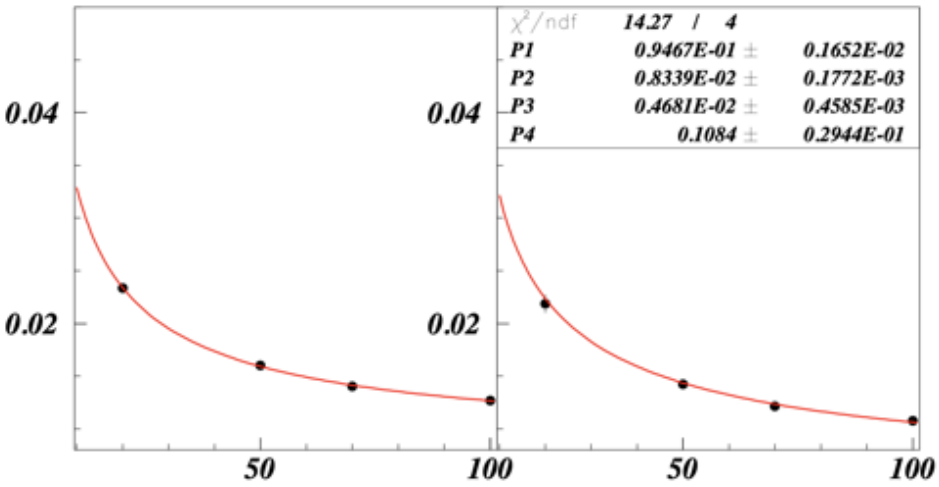

FIGURE 3.5: Energy resolution of an inner-region Shashlik measured in testbeam. $P1$ is the sampling term, $P2$ and $P3$ are the constant term corresponding to data acquisition with a 30x60 mm^2 or a 2x2 mm^2 beam, respectively, $P4$ is the noise term. From reference [31].

3.2 Future and Upgrades

The quest for new physics demand ever increasing collisions to seek experimental deviations from the theoretical predictions of the Standard model. This requires increasing the instantaneous luminosity of Run 1 and 2 and upgrading the detector to cope with the consequent harsher environment.

Fig. 3.6 shows the schedule of LHCb. The experiment ran at luminosity of $2x10^{32}cm^{-2}s^{-1}$ for Run 1 and 2. It is scheduled to run at $2x10^{33}cm^{-2}s^{-1}$ for Run 3 and Run 4 and at $1.5x10^{34}cm^{-2}s^{-1}$ for Run 5 and Run 6.

During LS2 it underwent the Upgrade I to improve precision and remove limitation imposed by the hardware trigger [33]. In the Calorimeter system, the SPD and PS were removed and the readout electronics upgraded to run at 40 MHz. No modification to the ECAL modules took place.

The LHCb Upgrade II is scheduled for LS4 to cope with the additional increase in the particle flux. The new environment will demand:

Radiation hardness : the radiation dose will reach order of 1 MGy and $6x10^{15}$ 1 MeV neq/cm^2

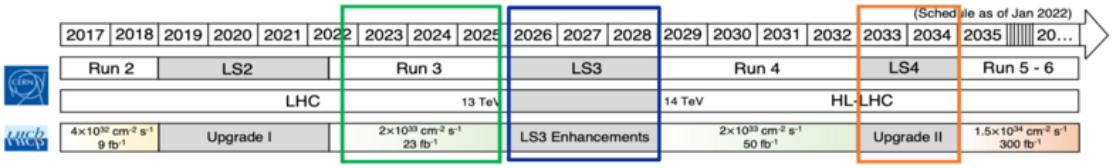

FIGURE 3.6: Timeline of the LHCb future runs and updates. Highlighted are the current run (Run 3), the LS3 and LS4, when the consolidation works and the full Upgrade 2 will take place, respectively.

in the innermost part of the ECAL (Fig. 3.7). At least 176 modules will be above the 40 kGy limit of current Shashliks, thus requiring a new technology;

Increased granularity : the Molière radius of the modules must be shortened using materials like Tungsten and the number of cells increased to mitigate the overlap of neighbouring showers. Additionally, longitudinal segmentation is being considered. Segmenting the modules into a front and a back section mitigates the effects of radiation damage [34], improves PID, and could prove useful to separate overlapping clusters;

Timing : time resolution of a few tens of ps counteracts the larger number of primary vertices per bunch crossings mitigating the combinatorial background during reconstruction;

Performance : to profit from the increased luminosity it is necessary keeping at least the same performance of Run 1. The new technology must target an intrinsic resolution of $\sim \frac{10\%}{\sqrt{E}} \oplus 1\%$.

Moreover, performance studies show that already by LS3 a large number of ECAL Shashliks will lose efficiency due to radiation damage, with the innermost becoming not operational (Fig. 3.8). Consolidation work is thus required even before the Upgrade II. Ideally, any modification taking place in LS3 should be compatible with the upgrade of LS4.

This thesis discusses the R&D performed on the technologies to replace Shashliks in the high-dose central area. The baseline solution are modules of spaghetti calorimeter (SPACAL, Fig. 3.9). A SPACAL is a sampling calorimeter wherein scintillating fibres are inserted into a dense absorber. The scintillating fibres convert the deposited energy into light and transport it to the photodetectors, avoiding wavelength-shifters which entail a reduction in light collection efficiency. At the same time, the electromagnetic shower

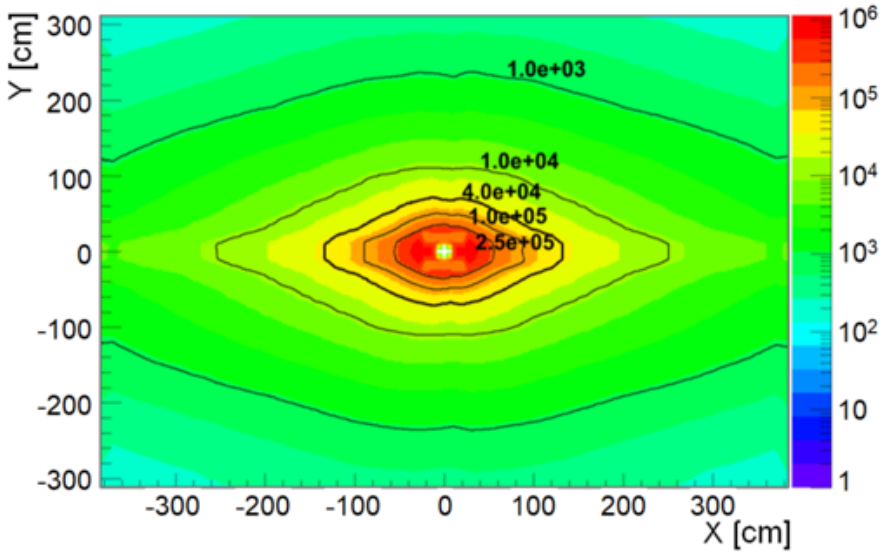

FIGURE 3.7: Map of the radiation dose in Gy expected on the ECAL in Run 5 and 6. From reference [32]

dimension can be tuned by selecting absorber materials with adequate radiation length and Molière radius.

Two different SPACAL configurations are foreseen for the upgrade. The modules in the high-radiation area will comprise Tungsten absorber and radiation-hard inorganic crystal fibres. This combination will provide a Molière radius of about 15 mm. However, Tungsten becomes more active over longer time than Lead, and the inorganic crystals are expensive and difficult to produce. For these reasons, the region from 40 to $\sim$100 kGy will be equipped with Lead absorber and radiation-tolerant plastic fibres.

The Upgrade II ECAL will be divided into 5 rhomboidal regions, matching the incident particle flux (Fig. 3.10). The regions are identified by the cell size, decreasing towards the centre:

15x15 mm^2 : 32 SPACAL modules with Tungsten absorber and inorganic crystal fibres;

30x30 mm^2 : 144 SPACAL modules with Lead absorber and plastic fibres;

40x40 mm^2 : 176 Shashlik modules of the current inner region type;

60x60 mm^2 : 448 Shashlik modules of the current middle region type;

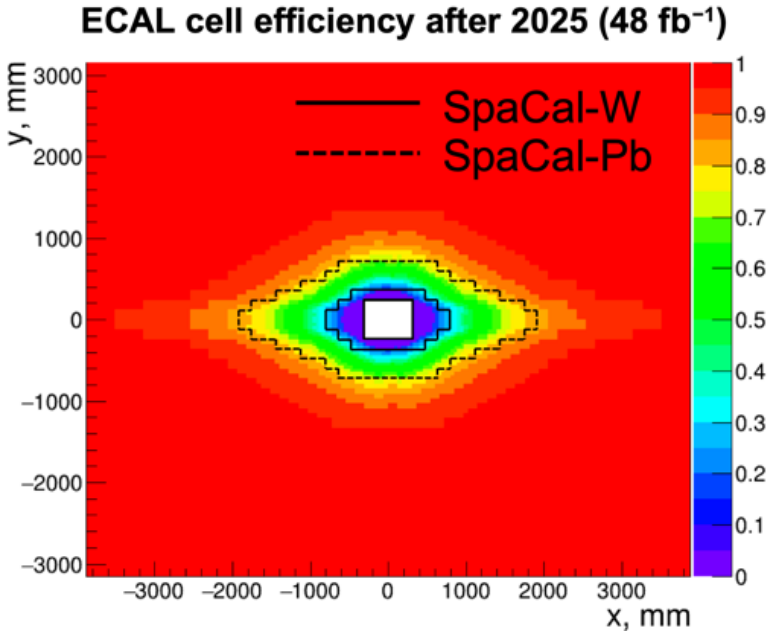

FIGURE 3.8: Expected efficiency of the current ECAL modules after Run 3. Efficiency drops in the central region due to radiation damage. The solid and dashed lines are the regions scheduled for replacement by the SPACAL (see Fig. 3.10 and text). Courtesy of Y. Guz.

120x120 mm^2 : 2512 Shashlik modules of the current outer region type.

All modules will be segmented into a front and a back section, with double side readout. The current Shashliks will be refurbished, if the accumulated radiation damage allows it, and upgraded with faster WLS. Otherwise they will be made anew.

The consolidation works during LS3 include re-arranging the modules in the rhomboidal shape and dividing the calorimeter into 5 regions. Both Lead and Tungsten SPACAL will be inserted. The Tungsten prototype will be temporarily equipped with plastic fibres, replaced by inorganic crystals for the Upgrade II. All the prototypes will be unsegmented and read out only at the back. Timing electronics will be tested in the SPACAL regions.

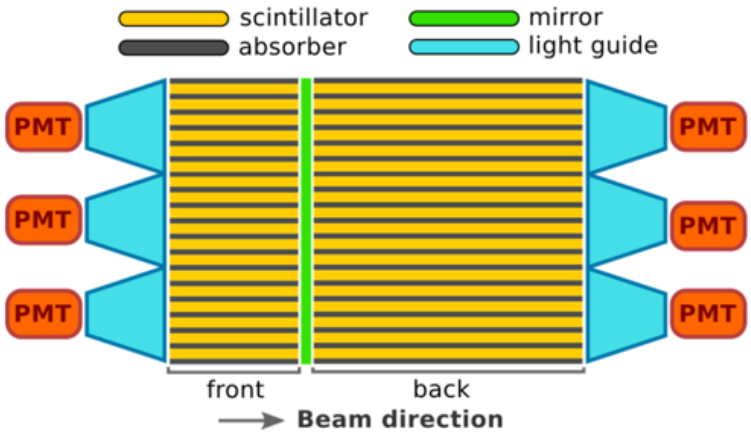

FIGURE 3.9: Schematic side view of a SPACAL. From reference [32].

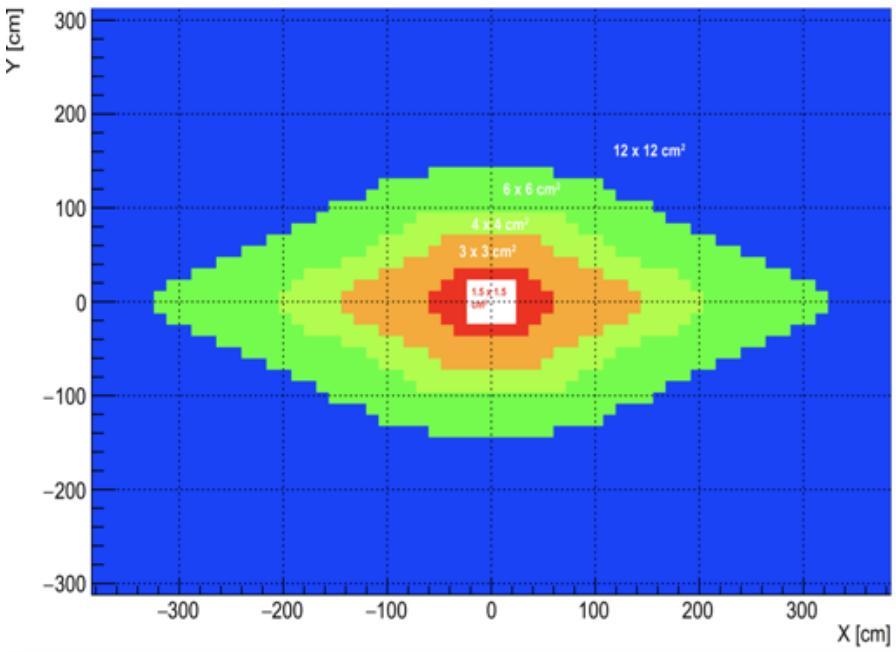

FIGURE 3.10: Planned layout of the Upgrade II ECAL, showing the multiple regions and their cell size. Courtesy of P.Roloff.

Part II

Characterisation and Development of Scintillators

Characterisation and Development of Scintillators

Although primary particles measured in high energy calorimetry cover several orders of magnitudes in energy – from hundreds of MeV up to the TeV scale – the electromagnetic showers by them produced comprise mainly secondary particles of energy below 1 MeV [2]. Common laboratory radioactive sources offer an accessible probe into the scintillators' properties and their contribution to the performance of the detectors.

The following sections present the R&D performed on scintillating materials:

- Chap. 4 offers a brief introduction on scintillation, the main quantities, and the materials;
- Chap. 5 describes the methods and the set-ups employed for the characterisation of the scintillators;
- Chap. 6 is dedicated to the studies on GAGG inorganic crystals: first, the state of the art was assessed, then, novel compositions were tested to suit high-rate environments;
- Chap. 7 discusses the preliminary work on organic scintillators for environments up to a few hundreds of kGy.

Chapter 4

Scintillation

Scintillation is a luminescence induced by ionising radiation in dielectric media. Scintillators contain luminescent centers that, when excited, relax radiatively, i.e. emitting a photon. These centers can be either extrinsic, e.g. doping ions/dyes, or intrinsic, e.g. molecular systems of the host matrix. [35]

The most widely used Scintillators are organic and inorganic scintillators. The chapter will first discuss the common characteristics of scintillators and then a few examples.

4.1 Characteristics of a Scintillator

4.1.1 Photoluminescence

Photoluminescence (PL) is the emission of light induced by the direct excitation of the luminescence centres caused by light. It differs from scintillation inasmuch as it is not induced by ionizing radiation, the former featuring additional kinetics like the thermalization of hot carriers and the transfer to the luminescent centres.

Measurements study the emission intensity wavelength-resolved $I(\lambda)$, called photoluminescence emission spectrum. Often, they are paired with excitation spectra, i.e. measuring the amplitude at a given emission wavelength varying the excitation. The two offer important information on the energy levels involved in the luminescence.

4.1.2 Transmission and Absorbance

Given a monochromatic light beam of intensity I_0 and wavelength λ, **transmission** is defined as the fraction of light intensity traversing a sample:

$$T(\lambda) := \frac{I(\lambda)}{I_0(\lambda)}, \tag{4.1}$$

being I the light intensity observed after the sample.

Absorbance is computed as the logarithm of the ratio of incident to transmitted light intensity:

$$A(\lambda) = \log_{10} \frac{I_0(\lambda)}{I(\lambda)} = -\log_{10} T(\lambda) \tag{4.2}$$

Combined with the photoluminescence it can offer insights into the material. For instance, the Stokes shift is the distance between the absorbance and the emission maximum of an energy level.

Ionizing radiation can alter the composition of a scintillator, possibly affecting its transmission. This transmission loss is quantified by the **radiation-induced absorption length**, computed as:

$$K = \frac{1}{L} \log \frac{T_{before}(\lambda)}{T_{after}(\lambda)} \tag{4.3}$$

being L the sample thickness traversed by the light beam.

Transmission and absorbance provide information on the energy levels of the material complementary to emission and excitation spectra. Moreover, it can assess quantitatively the surface state of a sample.

Transient Optical Absorption

The **transient optical absorption** (TOA or TA) technique in pump-probe configuration is a time-resolved measurement of the absorbance (probing) after some excitation (pumping). The latter is achieved via a laser burst displacing electron-hole pairs from an equilibrium state. The probing offers insights on the kinetics of the non-equilibrium carrier, which transport the energy to the luminescence centers in inorganic crystals.

The technique was first employed by Prof. R. T. Williams to study the non-linearity in the response of CsI:Tl, NaI:Tl, SrI_2:Eu scintillators [36], and then employed for scintillation kinetics and timing properties [37, 38].

4.1.3 Light Yield and Output

The **light yield** of a scintillator is defined as the average number of photons produced per MeV of energy deposited. The experimental measurement of light yield is complicated by the light trapping occurring to photons due to Snell's law:

$$n_1 \sin\theta_1 = n_2 \sin\theta_2 \tag{4.4}$$

being n_i and θ_i the refractive index of the i-th medium and the incidence angle of the photon in the i-th medium, respectively. Assuming $n_1 > n_2$, a photon incident on the interface between the first and second medium with an incidence angle smaller than

$$\theta_c = \arcsin\frac{n_2}{n_1}, \tag{4.5}$$

would be refracted toward incidence angles greater than 90° in the second medium and is thus reflected back inside the first. The phenomenon is called **total internal reflection**.

More often quoted is the **light output**, that is the photons output of the scintillator at one surface per MeV of energy deposited. The latter is proportional to the former via a coefficient called light transport efficiency (LTE). The LTE depends on several factors including the scintillator's index of refraction, geometry, and surface state.

4.1.4 Surface State and Wrapping

The surface state plays a huge contribution in the performance of a scintillator. Optical polishing of the side surfaces allows exploiting total internal reflection within the critical angle to transport efficiently the optical photons towards the readout.

Photons bouncing on the side surfaces with an incident angle below the critical one are refracted and exit the scintillator – barring Fresnel reflections. Samples are often wrapped in reflective materials like Teflon. Teflon is a diffusive reflector: it reflects the optical photons varying their incidence angle according to a statistical distribution[1]. In this way, part of the photons that would be lost on the sides is reflected back inside the scintillator with an incidence angle that could suit transport.

[1] An ideal diffuse reflector exhibits Lambertian reflection, i.e. the surface radiance is constant from any angle of observation.

Conversely, most photons ought to be extracted by the face coupled to the readout. High-refractive-index optical grease or glue can be employed in a bid to increase the critical angle and the extraction cone.

Wrapping and optical couplings increase the LTE significantly [39]. At the same time, they affect the spatial homogeneity of the LTE in long samples: for instance, increasing the extraction cone with optical grease reduces the attenuation length in inorganic fibres due to the photons at large angles that travel longer inside the fibre and are, thus, more attenuated by self-absorption [40].

4.1.5 Scintillation Kinetics

The scintillation kinetics is defined as the time evolution of the scintillation intensity $f(t)$. The function $f(t)$ is affected by the dynamics of the carriers and of the luminescence centers. It is often described by sets of differential equations solved numerically. A review of the topic in inorganic crystals is [41].

A common first-order approximation is to describe $f(t)$ as a sum of bi-exponential functions:

$$f(t|\theta) = \Theta(t-\theta) \sum_{i=1}^{N} \frac{e^{-(t-\theta)/\tau_{d,i}} - e^{-(t-\theta)/\tau_{r,i}}}{\tau_{d,i} - \tau_{d,r}} \cdot \rho_i, \tag{4.6}$$

where Θ is the Heavyside function and θ is the onset time of the scintillation. The parameters $\tau_{d,i}$, $\tau_{r,i}$, ρ_i are called decay time, rise time, and abundance, respectively, of the i-th component.

Often scintillators feature a fast and a slow decay time components, which can differ even by an order of magnitude. The effective decay time $\tau_{d,eff}$ is a figure of merit for the fast part of the scintillation:

$$\frac{1}{\tau_{d,eff}} \equiv \sum_{i=1}^{N} \frac{\rho_i}{\tau_{d,i}} \tag{4.7}$$

4.1.6 Timing

Fast timing capability has emerged a new requirement for scintillators in the past few years. The possibility of time-tagging the arrival of a particle with precision of about 10 ps will be crucial to reject pile-up at high-luminosity colliders. Beside HEP, Time-of-Flight Positron Emission Tomography (TOF-PET) would greatly benefit from similar time resolutions, as discussed in Sec. 5.5.

Timing consists of assigning a timestamp to a signal marking the time of detection of the incident particle. Common techniques employed are leading edge discrimination, where the timestamp is given by the signal pulse crossing a fixed amplitude threshold, or constant fraction discrimination (CFD), where the threshold is set at a fixed fraction of the pulse amplitude. [42]

Computing the timestamp of a scintillation event is equivalent to the probability of detecting the k^{th} photon sufficient to cross the amplitude threshold. Using order statistics, the probability to observe the k^{th} photon of n between t and $t + dt$ is [43, 44]:

$$p_{k:n}(t) = n\binom{n-1}{k-1}F(t)^{k-1}(1 - F(t))^{n-k}f(t)dt \tag{4.8}$$

where $f(t)$ is given by Eq. 4.6 and $F(t)$ is the cumulative density function of $f(t)$. It can be demonstrated that the time resolution, defined as the standard deviation σ_t of the timestamps for a set of events, is:

$$\sigma_t \propto \sqrt{\frac{\tau_d \tau_r}{LO}} \tag{4.9}$$

where LO is the light output of the scintillator. Eq. 4.9 shows that scintillator for fast timing need both high light output and fast rise and decay times, and in particular that the time resolution is determined by the ratio of the latter to the former, called photon time-density.

4.2 Organic Scintillators

Organic scintillators are divided into plastic, liquid, and crystalline. Plastic scintillators are the most widely used due to their cost-effectiveness and their ease of manufacturing. They consist of a polymer matrix, such as polystyrene (PS) or ponyvinyltoluene (PVT), in which organic dyes are embedded. Having typical densities between 1.03 and 1.20 g cm^{-3} and low Z, they are usually employed for detection of charged particles or in sampling calorimeters, being unsuitable for applications requiring large stopping power, e.g. gamma spectroscopy or homogeneous calorimeters.

A charged particle traversing the scintillator ionises molecules along its path. The excitation is transferred to a primary fluor added in quantities of order 1% via Förster mechanism – a local non-radiative dipole-dipole energy transfer. The primary fluor emits light, usually in the UV. A secondary (and sometimes a third) fluor is added in $\sim$ 0.1% to absorb and re-emit the light at longer wavelengths.

The scintillation of plastics can vary significantly with different particles. For instance, the light output decreases with increasing ionisation density, according to Birks' law [45]:

$$\frac{dL}{dx} = L_0 \frac{dE/dx}{1 + k_B \cdot dE/dx}, \tag{4.10}$$

where dL/dx is the luminescence per length unit, L_0 the luminescence at low ionisation density, dE/dx the ionisation per length unit, and k_B Birks' constant, to be determined empirically for each scintillator. Differences happen also for the scintillation kinetics. Such features can be employed to discriminate γ, α, or neutrons via pulse shape analysis.

Light output upon γ photons excitation is up to 10000 photons/MeV, with fast decay times ranging from a few ns down to $\leq$1 ns.

4.3 Inorganic Scintillators

Inorganic scintillators come in two forms: single crystals of polycrystalline ceramics. A single crystal is a material in which the crystal lattice is periodic and continuous until the edges. Single crystals have better optical properties than ceramics, but are more expensive to grow. Inorganic crystals have higher stopping power than organic scintillators, with density between 4 and 8 g cm^{-3} and high-Z elements.

The light yield per E_0 of ionising radiation absorbed is [46]:

$$Y = \frac{E_0}{\beta \cdot E_g} \cdot S \cdot Q \tag{4.11}$$

where E_g is the material band gap, $\beta \cdot E_g$ is the mean energy necessary for the creation of an electron-hole pair[2], $S \leq 1$ is the efficiency of energy transport to the luminescence centers, and $Q \leq 1$ the radiative efficiency of the luminescence center at a given temperature. It must be noted that Eq. 4.11 neglects some second order effects like the recombination of the e-h pairs due to surface effects.

The light yield and scintillation kinematics of inorganic crystals can depend on the ionisation density; for instance, low-energy photoelectrons produced by X-rays are more densely ionising than γ photons, which can reduce S due to Auger-like effects [47].

Scintillation in inorganic materials can be either intrinsic or extrinsic. In $PbWO_4$, scintillation is predominantly due to excitations of the oxy-anyonic complexes WO_4^{2-} [48].

[2] β is between 2 and 3 for oxides [46].

On the contrary, scintillation in YAG:Ce is due to the radiative transition $5d_1 \rightarrow 4f$ of Cerium [49].

A recent trend in inorganic scintillators are mixed crystals (or solid solutions), in which elements of the composition are replaced with isovalent ions [50]. Examples are Lu-Y substitutions in LYSO:Ce, or $CsRbCaEuBr_3$ [51]. While the complete periodicity of the crystal lattice is lost, a short range order is preserved as clusters of the different substitutional ions appear. These clusters are not larger then a few tens of nm. They can limit the diffusion of e-h pairs and enhance their probability of reaching a luminescence center [52]. Consequently, the light yield is significantly increased, as in the case of Ga-Al and Gd-Y in GYAGG:Ce reaching 52000 photons/MeV [53] with respect to YAG:Ce (20000-30000 photons/MeV).

Chapter 5

Materials and Methods

5.1 Photoluminescence

The emission spectra of photoluminscence were measured with a Perkin Elmer LS55 spectrofluorometer. The spectrofluorometer emits a tunable monochromatic beam of light onto a sample and measures the light intensity at 90° as a function of its wavelength.

In Sec. 6.1, time-resolved PL measurements were performed at the Institute of Physics of the Czech Academy of Sciences. A pulsed nanoLED 450 nm (Horiba IBH Scotland) excited the samples whose emitted light was detected by a custom-made spectrofluorimeter based on 5000M Horiba Jobin Yvon with single photon counting capabilities (see Sec 5.4).

5.2 Transmission and Transient Absorption

Transmission was measured with a Perkin Elmer Lambda 650 spectrophotometer. A monochromatic light beam is split into two beams: one traverses the sample under test, the other beam is employed to monitor drifts of the instrumentation.

Transient absorption measurements were performed at the Institute of Photonics and Nanotechnology, Vilnius, Lithuania. The output of a Yb:KGW laser (Pharos, Light Conversion) – delivering 250 fs pulses at 1030 nm – was split into a pump and a probe beam. The pump beam was equipped with an optical parametric amplifier and a harmonic generator to tune the pump photon energy for resonant excitation of Ce^{3+} activator ions to their excited levels $5d_1$ and $5d_2$. The TA amplitude is proportional to the population of the photoexcited electrons and was probed by the second beam converted to

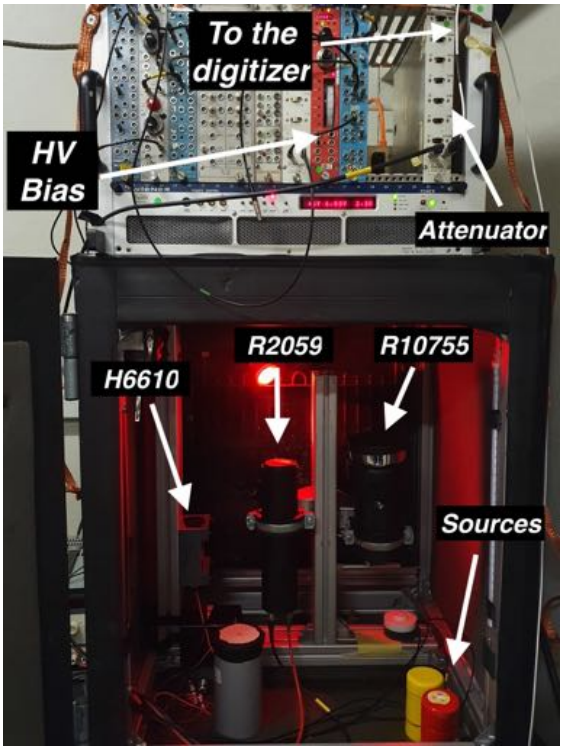

FIGURE 5.1: Picture of the light output bench with the dark box open.

a white light supercontinuum in the range from 1.3 to 2.7 eV (950–460 nm) after sharp focusing in a sapphire plate. The probe beam was equipped with an optomechanical delay stage enabling a delay up to 10 ns with a subpicosecond precision. Thus, the set-up enabled measuring the time evolution of the TA spectrum with a subpicosecond time resolution. More details in [54, 55].

5.3 Light Output

The test bench comprises a Hamamatsu R2059 photomultiplier tube placed in a dark box at 18 °C (Fig. 5.1) and connected to a DT5720A CAEN digitizer performing charge integration. The PMT is biased at 2500 V, providing sufficient gain to resolve the charge of single photoelectron pulses. That allows to convert the total charge of a scintillation event to photoelectrons produced. The number of photons impinging on the PMT is obtained correcting for the average quantum efficiency of the PMT, computed as

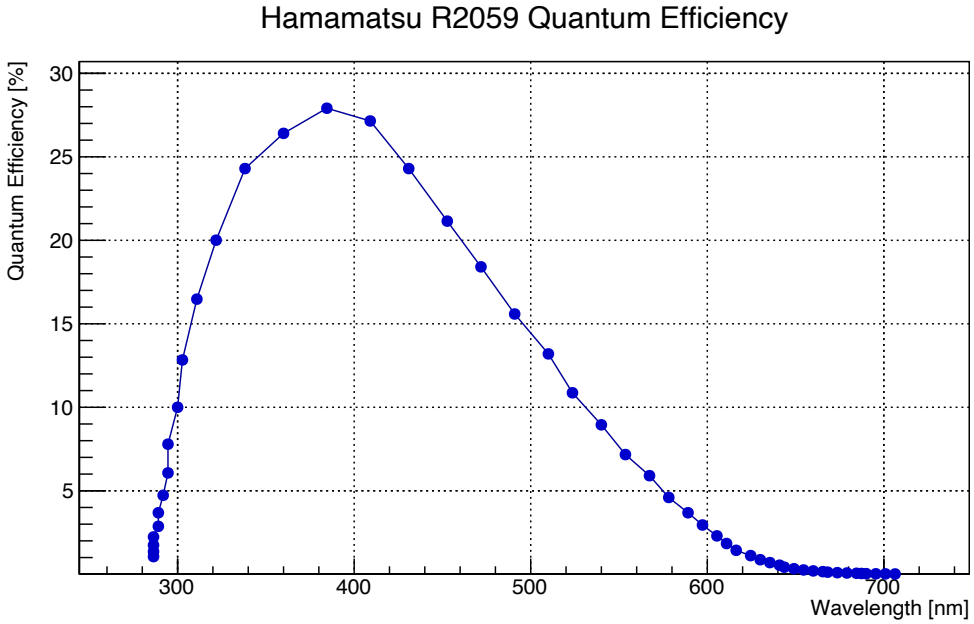

FIGURE 5.2: Quantum efficiency of the Hamamatsu R2059 PMT.

the weighted average of the scintillator's emission and the PMT's quantum efficiency (Fig. 5.2).

All the light output measurements were performed wrapping in Teflon the samples on all faces but the one coupled to the PMT.

5.4 Scintillation Kinetics

Time Correlated Single Photon Counting (TCSPC) is a technique to compute the time distribution of the emission of the scintillation photons by measuring the time of emission of single scintillation photons. [56]

A start signal gives the moment in which the event takes place. A photodetector, called stop detector, outputs a timestamp when it detects a photon produced in the sample under test. The distribution of the delays between stop and start is a convolution of the scintillation time distribution and the IRF of the set-up. The IRF is the experimental limit of the measurement and it is often dominated by the single photon time resolution

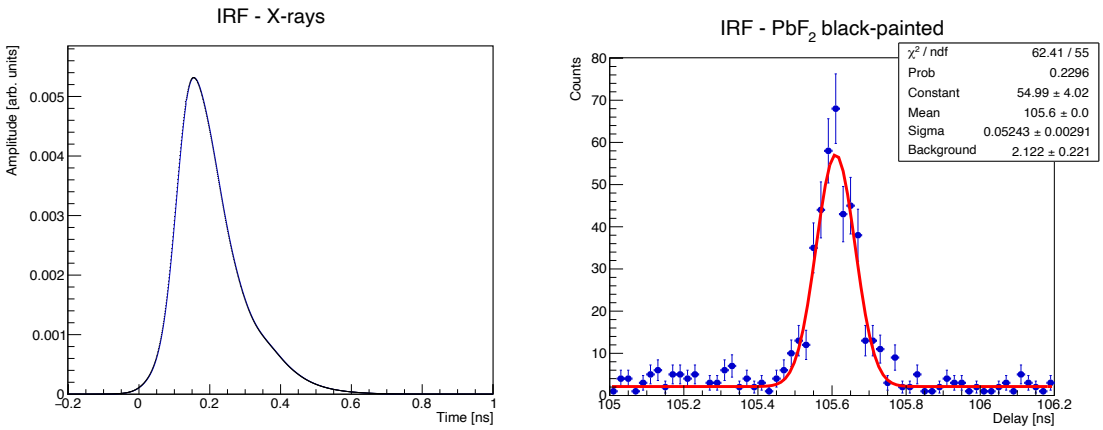

FIGURE 5.3: Impulse response functions of the pulsed X-rays (left) and of the 511 keV TCSPC (right, from reference [59].) test benches. The latter is well-described by a gaussian distribution over a constant background (red curve fitted to the data).

of the detector employed. Modern SPADs or hybrid PMTs offer IRFs a few tens of ps wide.

The single photon counting technique requires the probability to detect an impinging photon to be constant in time. Were that not the case – e.g. due to dead time of the detector – the measured distribution would be biased in favour of the earliest photons, artificially accelerating the decay times. For this reason, the following measurements were performed reducing the solid angle covered by the detector with a shutter to detect approximately 1% of the total interactions in the sample under test. This suppress the probability to detect 2 optical photons per event, eliminating the bias. [57, 58]

Two test benches were employed. In the first, a pulsed X-rays tube with Tungsten anode biased at 40 kV is driven by a picosecond laser. The laser driver provides the start signal. The samples are placed in front of the tube exit window and a hybrid photomultiplier tube HPM 100-07 Becker & Hickl is used to detect the scintillation photons' time of arrival. The IRF of the system is given by the convolution of the laser driver response, the X-rays tube response and the hybrid PMTs single photon time resolution (Fig. 5.3, left). See [60] for more details.

The second test bench (Fig. 5.4) relies on the two back-to-back 511 keV gamma photons produced in the positron annihilation of the β^+ decays of a ^{22}Na source. The start signal is measured by a 2x2x5 mm^3 LSO:Ce crystal co-doped with 0.4% Ca wrapped in Teflon

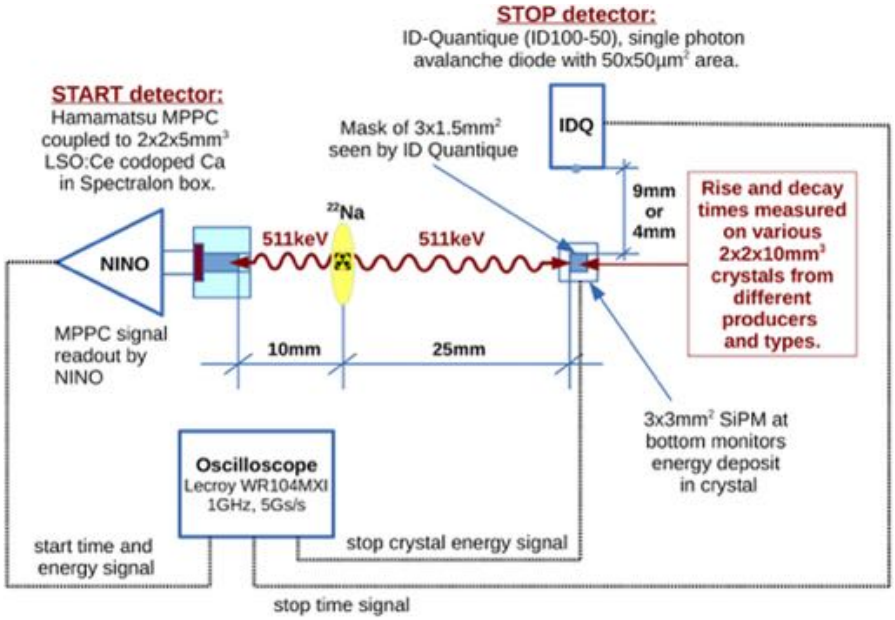

FIGURE 5.4: Time correlated single photon counting setup with 511 keV source. From reference [60].

and mounted on a Hamamatsu S13360-3050CS SiPM with Cargille Meltmount optical glue (n = 1.58). The SiPM signal was split, with one branch fed into a NINO ASIC ultra-fast discriminator [61] to get the timestamp of the event, and the other used to measure the energy deposition. As stop detector, a single photon avalanche diode (SPAD) with 50x50 μm^2 by ID-Quantique (IDQ) ID100-50 was selected for its low dark count rate down to 20 Hz. Additionally the sample under test was placed on a 3x3 mm^2 PM3350 SiPM from Ketek to evaluate the energy deposition for each coincidence. The IRF of the detection chain was measured exploiting Cherenkov photons produced by photoelectrons in a 2x2x5 mm^3 PbF_2 crystal painted black on all sides except that facing the IDQ. PbF_2 does not scintillate and it is a good Cherenkov radiator thanks to its high refractive index and wide transparency region. The black paint was used to shield stray light emitted by the Ketek SiPM, and to suppress reflections inside the crystal [62], thus allowing to precisely measure the IRF of the detection chain. The IRF was well-described by a Gaussian with 52 ps standard deviation (Fig. 5.3, right). See [63] for more details.

5.5 Coincidence Time Resolution

The Coincidence Time Resolution (CTR) is defined as the width FWHM of the distributions of time of arrivals of 2 back-to-back 511 keV gamma photons produced upon positron annihilation. It is a key figure of merit in time-of-flight PET: achieving 10 ps CTR would allow volume imaging without tomographic reconstruction. [64, 65]

CTR measurements probe the intrinsic time resolution of a scintillator. It is an accessible technique to evaluate and compare the timing performance of different materials.

Eq. 4.9 shows the relationship between time resolution and scintillation parameters of a material. However, it does not include contributions such as the scintillator geometry and the photodetector's resolution. The photon travel spread (PTS)[1] and the photodetector's single photon time resolution (SPTR) are included in [66], confirmed by experimental measurements [67]:

$$\mathrm{CTR} = 3.33 \sqrt{\frac{\tau_{d,eff} \cdot (1.57 \cdot \tau_r + 1.13 \cdot \sigma_{SPTR*PTS})}{\mathrm{PDE} \cdot \mathrm{LO}}} := \frac{3.33}{\sqrt{\mathrm{IPTD}}} \tag{5.1}$$

where $\sigma_{SPTR*PTS}$ denotes the convolution of the SPTR of the SiPM with the PTS of the scintillator, altogether defining the initial photon time-density IPTD.

Two test benches were employed. The first is based on the NINO ASIC [61], sketched in Fig. 5.5. [44]. A ^{22}Na source was placed between the sample under test and a reference 2x2x3mm^3 LYSO:Ce pixel wrapped with several layers of Teflon and coupled to a HPK S13360-3050PE SiPM with Cargille Meltmount optical glue. The tested crystal was wrapped with Teflon and coupled with Rhodorsil optical grease to another HPK S13360-3050PE SiPM. Both SiPMs were biased at 60 V, about 8 V overvoltage. As in the NINO bench of Sec. 5.4, the SiPMs' signals were split into two, with one branch fed into the NINO ASIC, whose leading edge delay was the timestamp of the channel, and the other used to measure the energy deposit. Only photopeak events were selected for the measurement. The pulses were digitized with a DRS4 board, 5 GS/s, bandwidth 700 MHz [69]. The histogram of the mutual time delay was produced and fitted with a Gaussian function and its full width at half maximum, once corrected for the reference contribution (77 $\pm$ 2 ps FWHM), was the contribution of the crystal measured. This, multiplied by $\sqrt{2}$ in the assumption of two identical crystals, is the resulting CTR. For each sample a threshold scan was performed to find the optimal settings.

[1] The PTS is defined as the combined influence of the gamma interaction point fluctuation in the crystal and the time spread of a scintillation photon since its production to the impingement on the photodetector.

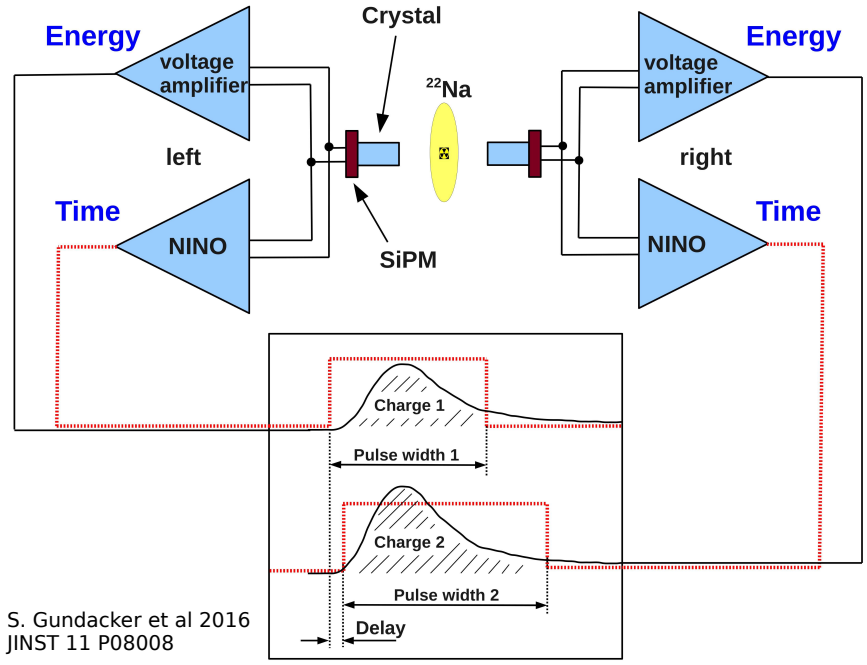

FIGURE 5.5: CTR setup with NINO ASIC. From reference [68].

In the second set-up, the NINO chip is replaced by a discrete high-frequency amplifier making the bandwidth of that circuit branch approximately 1.5 GHz. The larger bandwidth allows for better slew rate and higher signal-to-noise ratio, thus reducing the electronics contribution to time resolution. The output signals were digitized by a 4-channel LeCroy DDA735Zi oscilloscope (3.5 GHz bandwidth, 20 Gs/s sampling rate). [70]

Chapter 6

Garnet Crystals

6.1 State of the Art

Amongst the cerium-doped multicomponent garnets, GAGG stood out because of the high light yield, large density, and fast timing capabilities [71]. Moreover, the melting temperature, lower than both the other garnets and Lutetium oxyorthosilicates, made the material appealing for mass production compared to L(Y)SO:Ce.

In primis, it was necessary to assess the state of the art of the commercial GAGG single crystals. A characterisation campaign was launched involving several producers worldwide. The results are described in Sec. 6.1 and published in "*Scintillation Properties and Timing Performance of State-of-the-art* $Gd_3Al_2Ga_3O_{12}$ *Single Crystals*" on Nuclear Instruments and Methods in Physics Research Section A, reference [59].

6.1.1 Samples

The samples characterised are listed in Table 6.1. Being mostly commercial products, precise information on the composition was lacking.

The crystals were grown with the Czochralski technique and cut from the ingot to pixels of 2x2x3 mm^3 and 2x2x10 mm^3 (Fig. 6.1). All of them were mirror-polished, but for the C&A samples chemically etched. The polishing of the GFAG samples was improved mechanically at CERN albeit not sufficiently to carry out transmission measurements; as an alternative, a 10x10x10 mm^3 mirror-polished cube of the same GFAG ingot was used to measure transmission.

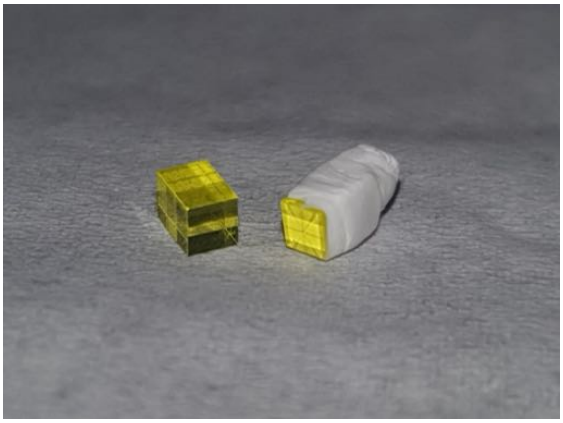

FIGURE 6.1: Two GAGG 2x2x3 mm^3 pixels used for the study of Sec. 6.1, the right one wrapped with Teflon.

6.1.2 Absorption and Photoluminescence Spectra

Photoluminescence spectra are reported in Fig. 6.2. The spectra span 470 and 700 nm, peaking in the 520-540 nm range. Differences between samples are due to variations in self-absorption and Stokes shift, influencing the shape and the peak position of the spectrum [72, 73]. The radiative transition to the spin-orbit-split doublet 4f state $5d_1 \rightarrow (^2F_{5/2}, ^2F_{7/2})$ is not resolved at room temperature, so the two peaks expected are merged into one. [49]

The tested crystals showed a vast transparency region towards the red end of the spectrum starting at approximately 475 nm. Emission and absorption overlap in the 450-500 nm region producing self-absorption.

Typical absorbance spectra of the crystals are shown in Fig. 6.3. The two Cerium $4f \rightarrow 5d_{1,2}$ transition peaks are visible at about 440 and 340 nm. At shorter wavelengths (below $\sim$320 nm) the absorption increases, but differently amongst the samples: the solely Cerium-doped Siccas sample shows a mild slope which steepens for the other samples; because of that, the Gadolinium transition peaks below 320 nm become unresolved. The increased absorption can be attributed to the charge transfer process of stable Ce^{4+} ions — achieved for instance through divalent-ions co-doping [74, 75]. The $4f \rightarrow 5d_2$ peak is not resolved for the samples featuring the strongest absorption (see Epic fast sample in Fig. 6.3).

The presence of the charge transfer absorption leads to profound differences in scintillation properties which are discussed in the next sections.

TABLE 6.1: Table of the GAGG crystals characterised in this study, including producers and geometries. The doping is explicitly stated when known.

Name	Producer	Dopants	Geometries
C&A :Ce:Mg	C&A	Ce, Mg	2x2x3 mm^3
C&A GFAG	C&A	N/A	2x2x3-10 mm^3, 10x10x10 mm^3
C&A Test 1	C&A	Ce, Mg	2x2x3 mm^3
C&A Test 2	C&A	Ce, Mg	2x2x3 mm^3
Crytur	Crytur	N/A	2x2x3 mm^3
ILM	Institut Lumière Matière	N/A	2x2x3-10 mm^3, 10x10x10 mm^3
EPIC	Epic-Crystal	N/A	2x2x3 mm^3
EPIC Fast	Epic-Crystal	N/A	2x2x3-10 mm^3, 10x10x10 mm^3
Fomos	Fomos-Materials	Ce, Mg, Ti	2x2x3 mm^3
Siccas :Ce	Siccas	Ce	2x2x3 mm^3
Siccas :Ce:Mg	Siccas	Ce, Mg	2x2x3 mm^3
Sichuan Tianle	Sichuan Tianle Photonics	N/A	2x2x3 mm^3

N/A = Information not available

6.1.3 Light Output

The measured light outputs ranged from 27900 $\pm$ 1100 up to 49500 $\pm$ 2000 photons per MeV, spanning almost a factor 2. They are reported in Table 6.2, whilst the energy spectra of two samples are plotted in Fig. 6.4. Variations are mainly due to differences in composition and quality of the samples: crystals with stronger charge transfer absorption showed a reduced light output. The GFAG's light output was measured before and after the additional mechanical polishing done at CERN, finding no difference within the experimental uncertainty.

Energy resolution varies amongst the samples. No strong correlation is observed with light output (see for instance the two Siccas). Three contributions determine the energy resolution, namely photostatistics, inhomogeneity of the sample and non-proportionality of the material [76, 77]. The photostatistics contribution lies between 5% and 7% for the samples with highest and lowest light output respectively. All the measurements yielded values above that, marking the presence of the other 2 contributions.

Although the samples are small, inhomogeneities in some of them that could lead to local variations in the light output cannot be excluded. Additionally, surface state effects are mitigated by the Teflon wrapping and grease coupling, but non-uniformities of the wrapping could play a role in deteriorating the resolution.

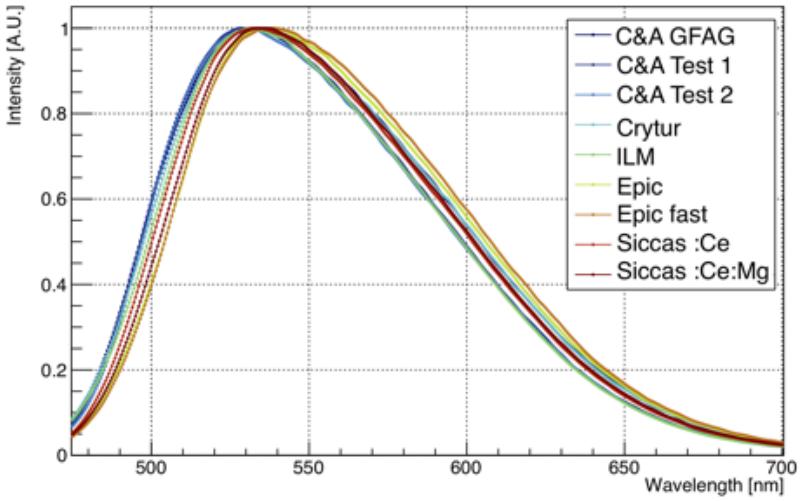

FIGURE 6.2: Photoluminescence emission spectra of all the 2x2x3 mm^3 samples tested. The spectra span 470 to 700 nm, all peaking in the 520-540 nm range. From reference [59].

Finally, the non-proportionality in GAGG is influenced by the composition of the crystal: for instance, reducing Gallium to a stoichiometric value of 2.4 reduces the non-proportionality and improves energy resolution but slows scintillation [78][1].

6.1.4 Scintillation Kinetics

Scintillation time profiles were measured selecting only events within the photopeak (511 keV) of the tested crystal. They were adequately described by Eq. 4.6 with 2 decay times and 1 rise time. Results are reported in Table 6.3. Fig. 6.5 shows the scintillation time profile for the C&A's GFAG crystal. C&A's GFAG, Epic's fast, and ILM's crystals featured the fastest scintillation, with a decay component close to 40 ns accounting for about two thirds of the emitted light and a slow decay component well below 200 ns, resulting in an effective decay time of about 55 ns; rise time was below 100 ps.

[1]The overall better resolution observed in the publication cited can be due to a better match of the photodetector QE to the crystal emission, reducing the photostatistics contribution.

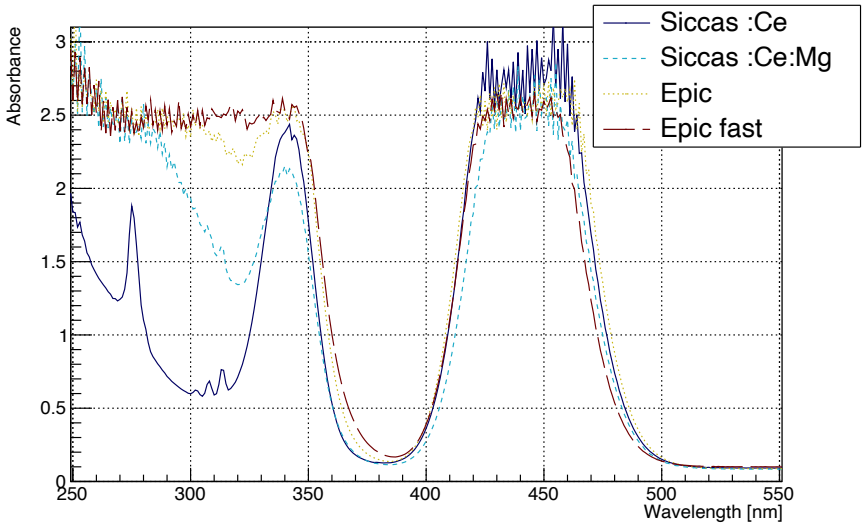

FIGURE 6.3: Absorbance spectra of four typical 2x2x3 mm^3 samples. Stabilisation of Ce^{4+} increases absorption below 350 nm: Gd-transition peaks are only resolvable for the Siccas sample without magnesium. From reference [59].

The scintillation kinetics of garnets can vary at lower excitation energies, in the X-ray range [79], however selecting only Compton events down to 200 keV no appreciable difference was found in these measurements.

TABLE 6.2: Light output and energy resolution of the 2x2x3 mm^3 crystals, upon 661.7 keV excitation with a ^{137}Cs gamma source. The relative uncertainties are $\pm$ 3% for the light output and 4% for the energy resolution.

Crystal	Photons output [MeV^{-1}]	Resolution (FWHM)
C&A :Ce:Mg	37 280	9.4%
C&A GFAG	32 140	11.3%
C&A Test 1	42 770	7.1%
C&A Test 2	43 100	6.8%
Crytur	29 310	9.9%
ILM	27 900	12%
EPIC	37 760	11.5%
EPIC Fast	30 330	11.5%
Fomos	37 700	11.3%
Siccas :Ce	49 500	8.5%
Siccas :Ce:Mg	41 840	6.8%
Sichuan Tianle	38 582	10.8%

TABLE 6.3: Scintillation rise and decay times and relative abundances under 511 keV gamma excitation. The effective decay time is defined in Eq. 4.7.

Crystal	τ_r [ps]	τ_{d1} [ns]	R_1 [%]	τ_{d2} [ns]	R_2[%]	$\tau_{d,eff}$ [ns]
C&A :Ce:Mg	70 ± 15	57 ± 3	61 ± 3	196 ± 15	39 ± 3	79 ± 4
C&A GFAG	63 ± 15	41 ± 3	65 ± 3	172 ± 15	35 ± 3	56 ± 4
C&A Test 1	720 ± 30	81 ± 3	62 ± 3	296 ± 15	38 ± 3	112 ± 4
C&A Test 2	501 ± 30	85 ± 3	62 ± 3	302 ± 15	38 ± 3	117 ± 4
Crytur	73 ± 15	49 ± 3	65 ± 3	207 ± 15	35 ± 3	67 ± 4
EPIC	65 ± 15	64 ± 3	67 ± 3	199 ± 15	33 ± 3	82 ± 4
EPIC Fast	60 ± 15	42 ± 3	63 ± 3	139 ± 15	37 ± 3	57 ± 4
Fomos	77 ± 15	60 ± 3	58 ± 3	220 ± 15	42 ± 3	86 ± 4
ILM	78 ± 15	42 ± 3	65 ± 3	145 ± 15	35 ± 3	56 ± 4
Siccas :Ce	1178 ± 50	119 ± 3	72 ± 3	306 ± 15	28 ± 3	144 ± 4
Siccas :Ce:Mg	114 ± 15	72 ± 3	62 ± 3	239 ± 15	38 ± 3	98 ± 4
Sichuan Tianle	148 ± 15	62 ± 3	68 ± 3	128 ± 15	32 ± 3	74 ± 4

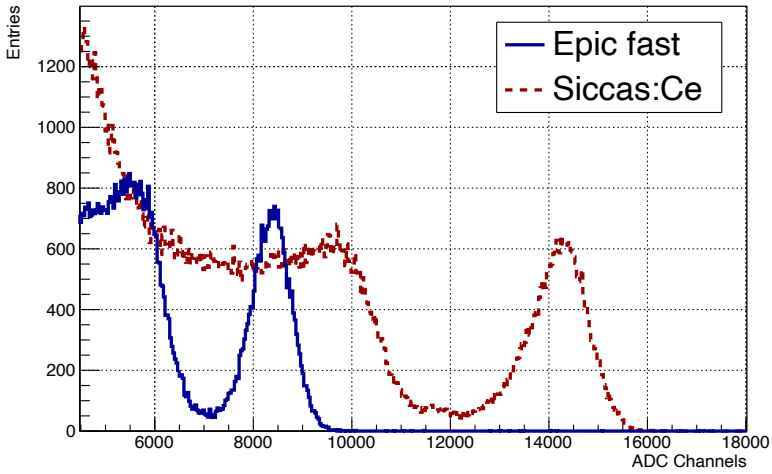

FIGURE 6.4: Light output spectra of the Epic fast and Siccas Cerium-doped sample. The crystal with only Ce-doping shows the highest light output, whilst the stabilisation of Ce^{4+} centres speeds up scintillation at the expense of light output. From reference [59].

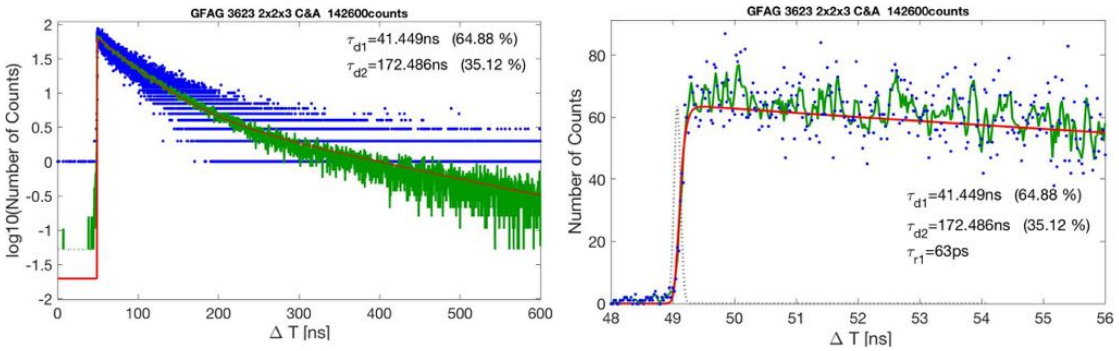

FIGURE 6.5: TCSPC measurement of the GFAG 2x2x3 mm^3 sample. Blue dots are the measured entries, the red solid line the fitting curve, and the green solid line is a running average of the blue data points as a guide for the eye. The IRF of the system is shown as a black dotted line. Left: log scale plot, highlighting the decay. Right: zoom on the rising edge. From reference [59].

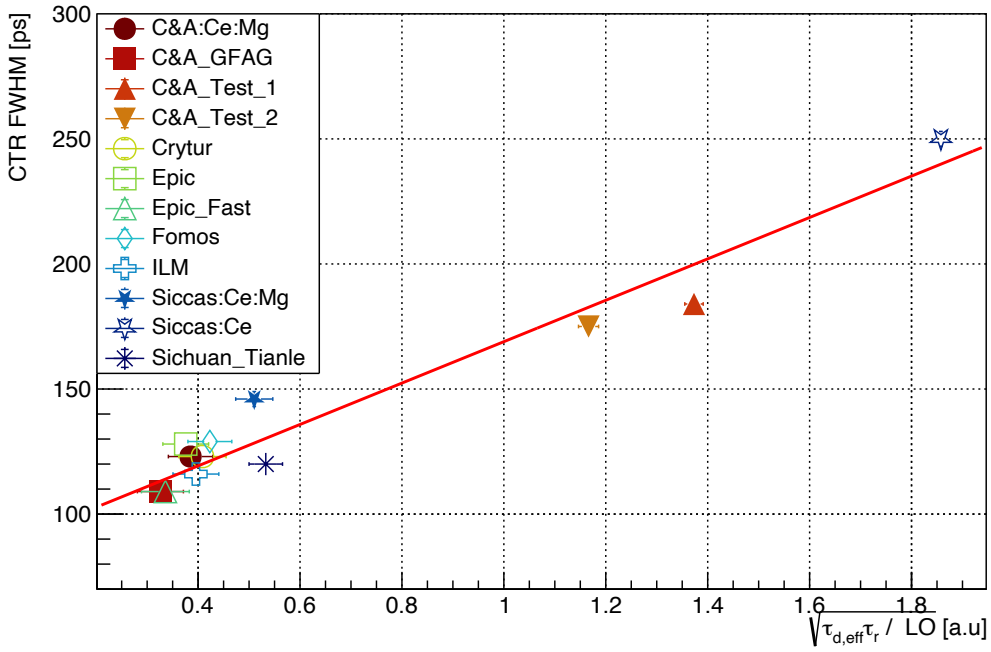

FIGURE 6.6: CTR measured with NINO readout against characteristic rise and decay times and light output as in Eq. 4.9. The red line is a linear fit to the data (slope 95 ± 2, intercept 80 ± 2), confirming the correlation. From reference [59].

6.1.5 Coincidence Time Resolution (CTR)

CTR varied largely between samples, and values are reported in Table 6.4. Epic's fast GAGG and C&A's GFAG showed a CTR as low as 109 ± 3 ps, whereas the non-codoped Siccas sample reached 250 ± 3 ps. The difference, greater than a factor 2, is due to the increase number of optical photons per time unit and is discussed in Sec. 6.1.6. Fig. 6.6 shows the CTR measured against the photon time-density. The two quantities are correlated, as predicted by Eq. 4.9.

CTR with High-Frequency Readout and 10 mm Long Crystals

In addition to the NINO-based campaign, the samples showing the best CTR were measured with the HF-CTR bench.The results are shown in Table 6.5; Epic's fast GAGG,

TABLE 6.4: Table of the CTR measurements performed with the NINO set-up (see Sec. 6.1.5). The samples were measured wrapped in Teflon and coupled with Rhodorsil optical grease to HPK S13360-3050PE. The error of the measurement is ± 3 ps.

Crystal	CTR [ps] 2x2x3 mm^3
C&A :Ce:Mg	123
C&A GFAG	109
C&A Test 1	184
C&A Test 2	175
Crytur	123
ILM	116
EPIC	128
EPIC Fast	109
Fomos	129
Siccas :Ce	250
Siccas :Ce:Mg	146
Sichuan Tianle	120

C&A's GFAG, and ILM's GAGG performed similarly within the measurement uncertainty, reaching 90, 87 and 90 ps ± 2 ps. To put these values in context, a CTR of 86 ± 2 ps for LYSO:Ce was measured in the same configuration [80]. The overall improvement in CTR is due to the better slew rate of the signal granted by the larger bandwidth.

Additionally, the CTR of three 2x2x10 mm^3 GAGG pixels was measured. The average CTR degradation observed moving from 3 mm to 10 mm long scintillators was 36 ps ± 3 ps (corresponding to a contribution of 87 ps ± 4 ps added in quadrature). A compatible degradation was observed in LYSO:Ce crystals, discussed in [81]. This degradation is due to the lower light transfer efficiency, effectively reducing the number of photons detected, and the larger PTS, increasing the time spread of the optical photons.

6.1.6 Correlations between Light Output and Scintillation Kinetics

In Fig. 6.7, the measured light outputs and effective decay times are plotted over constant-ratio lines drawn for reference. According to Eq. 4.9, shifts along one of these lines do

TABLE 6.5: Table of the CTR measurements performed with the HF readout [70]. The samples were measured wrapped in Teflon and coupled with Cargille Meltmount optical glue to HPK S13360-3050CS SiPM.

Crystal	CTR (HF) [ps] 2x2x3 mm^3	CTR (HF) [ps] 2x2x10 mm^3
C&A :Ce:Mg	99 ± 2	-
C&A GFAG	87 ± 2	124 ± 6
Crytur	101 ± 2	-
ILM	90 ± 2	126 ± 6
EPIC Fast	90 ± 2	124 ± 6
Sichuan Tianle	102 ± 3	-
LYSO:Ce [80]	86 ± 2	-

not modify the intrinsic CTR of the material and can be seen as design choices, wherein balance between light output and decay time is sought.

Light output and effective decay time are correlated, showing that the techniques employed to speed up scintillation entail a loss in light output. Notably, the samples do not lay along constant-ratio lines but move towards higher light output-decay time ratios at smaller decay times, improving the photon time-density and, thus, the time resolution (see Sec 6.1.5).

The three samples with fastest kinetics — C&A GFAG, Epic's fast GAGG and ILM's GAGG — share compatible absorption spectra, with high charge transfer absorption below 400 nm and unresolved 4f-$5d_2$ peak (see Fig. 6.3 and 6.8). The results show that stabilisation of Ce ions in their 4+ state quenches the light output accelerating scintillation and improving the time resolution.

Crytur's GAGG, the fourth sample of the bottom left group in Fig. 6.7, features slightly slower scintillation. This could be explained by lower charge transfer, given the lower absorbance below 350 nm (Fig. 6.8). Additionally, the $5d_{1,2}$-4f Ce peaks are less pronounced, suggesting less Ce overall.

6.1.7 Radiation Induced Absorption

The radiation hardness of the three compositions with fastest kinetics was tested. Samples of 10x10x10 mm^3 were irradiated with a hadron beam at the CERN IRRAD facility. 24 GeV/c protons were delivered in spills of approximately $5x10^{11}$ particles with a spot

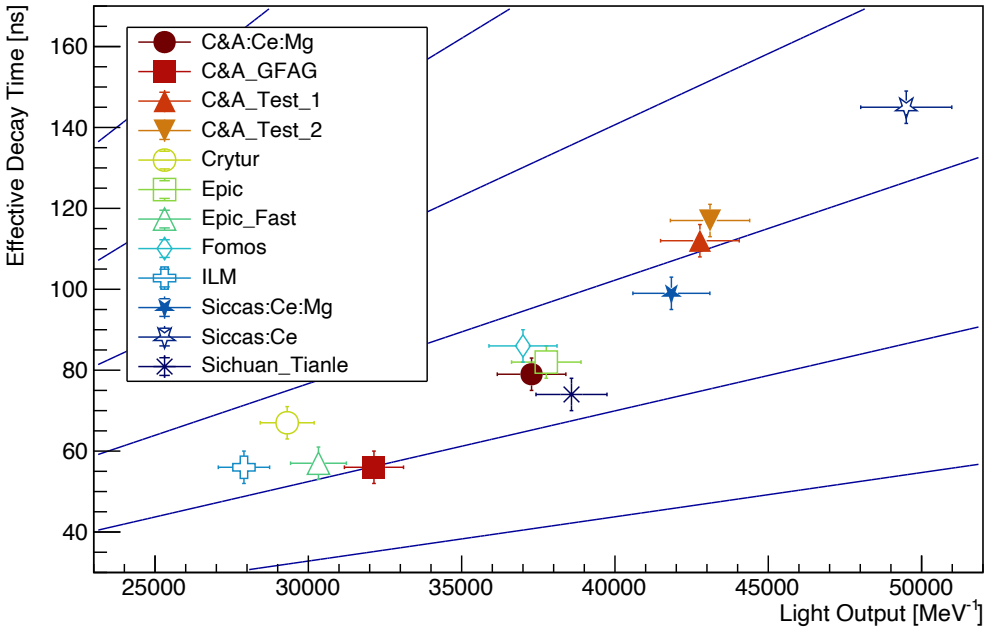

FIGURE 6.7: Left: Effective decay time and light output of the crystals. The blue lines are constant ratios: moving along them grants the same decay time-light output ratio, hence similar timing performance assuming the same rise time. Speeding up scintillation entails a loss of light output, although improving the photon time density. From reference [59].

of 12x12 mm^2 FWHM and an average rate of to 1x10^{14} proton cm^{-2}h^{-1}. Two Aluminium dosimeters were placed before and after the samples. The fluences achieved were 1.17x10^{15} p/cm^2 in the 5x5 mm^2 centre of the beam (a dose of approximately 280 kGy) and 0.95x10^{15} p/cm^2 in the neighbouring 10x10 mm^2 region.

The transmission of the samples was measured before and after the irradiation in the same configuration. Fig. 6.9 shows the Epic's sample; C&A and ILM's GAGG are similar. The induced absorption at 530 nm is compatible with zero. Some damage is visible in the gap between the $5d_1$ and $5d_2$ states. The results are in line with literature [82] and further tests at higher doses are planned.

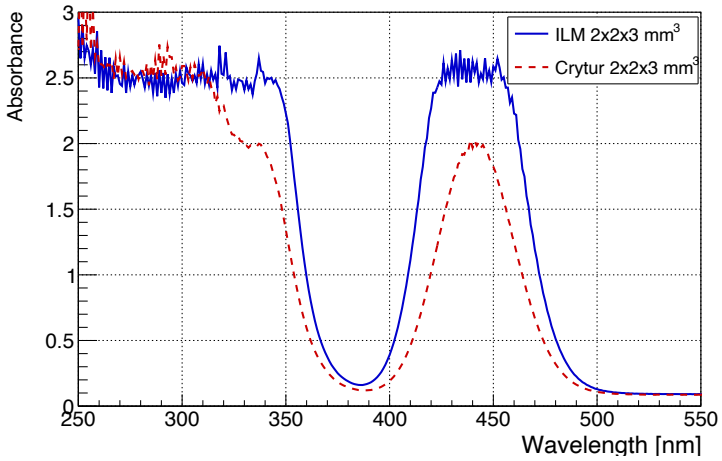

FIGURE 6.8: Absorbance spectrum for the ILM and Crytur 2x2x3 mm^3 crystals. The $5d_1 \rightarrow 4f$ Ce peak (440 nm) is less pronounced for the Crytur's sample and the $5d_2 \rightarrow 4f$ peak (340 nm) resolved, suggesting a lower concentration of Cerium overall, both in Ce^{3+} and Ce^{4+} state. From reference [59].

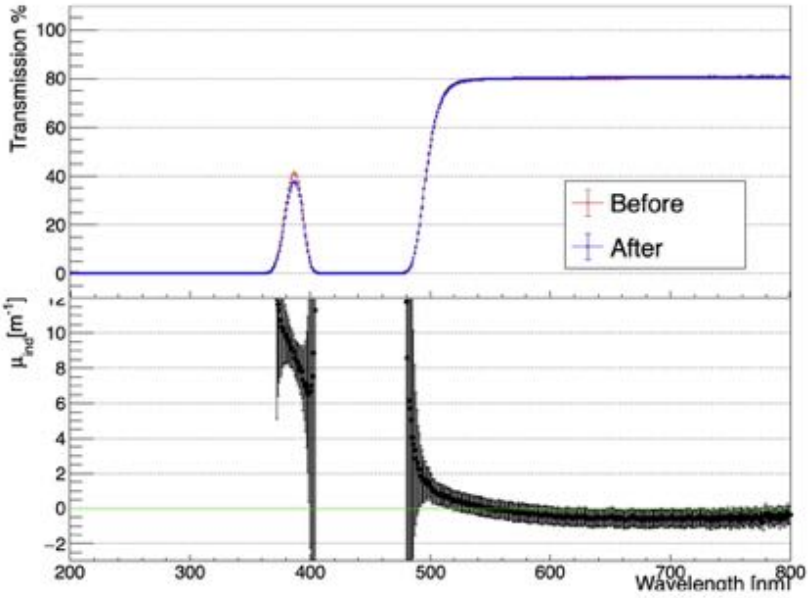

FIGURE 6.9: Transmission before and after the irradiation (top) and induced absorption length (bottom) for the Epic Fast GAGG.

6.2 Accelerating the Scintillation

The previous results demonstrated the outstanding qualities of GAGG, combining fast timing at the level of LYSO single crystals with better radiation hardness [83]. However, decay times above 40 ns with slow components of a few hundred are incompatible with the high-rate environment of the upgraded LHCb experiment and future colliders: the 40 MHz rate of the High-Luminosity LHC means that a hit cell would have a dead time of several collisions. Ideally, the decay time should be reduced to contain the whole scintillation inside a 25 ns (40 MHz) window.

Tuning the composition and dopants of GAGG allowed to vary the light output and decay time by more than a factor 2. An R&D effort was launched in collaboration with the Institute of Physics of the Czech Academy of Sciences and the Institute of Photonics and Nanotechnology in Vilinius to accelerate the scintillation of GAGG to the level of plastic scintillators. The results are discussed in the following sections and published in "*Compositional engineering of multicomponent garnet scintillators: towards an ultra-accelerated scintillation response*", Materials Advances, reference [84].

6.2.1 Samples

TABLE 6.6: Composition of plates AL1-6. "SC" stands for starting composition of the melt, the content values correspond to the stoichiometric coefficients in the chemical formula (e.g., $Gd_{2.955}Ce_{0.015}Mg_{0.03}Ga_3Al_2O_{12}$ for SC), and "g" is the fraction of melt volume consumed in the growth process at the position of the plate.

	g	Gd	Ce	Mg	Ga	Al
SC		2.955	0.015	0.03	3	2
AL1	0.065	2.917	0.0065	0.0051	2.787	2.284
AL2	0.155	2.944	0.0063	0.0053	2.813	2.231
AL3	0.416	2.978	0.0096	0.0058	2.845	2.160
AL4	0.618	2.954	0.0131	0.0039	3.043	1.986
AL5	0.703	2.959	0.0164	0.0060	3.108	1.982
AL6	0.789	2.952	0.0279	3.2510.0112	1.7583.251	1.758

A GAGG:Ce,Mg single-crystal ingot with a diameter of about 12.5 mm (see Fig. 6.10) was grown at the Institute of Physics of the Czech Academy of Sciences in Prague (FZU Prague) using the Czochralski method in a Cyberstar Mini-oxypuller machine in an iridium crucible under an atmosphere of nitrogen (2% oxygen). A set of plates, PL1

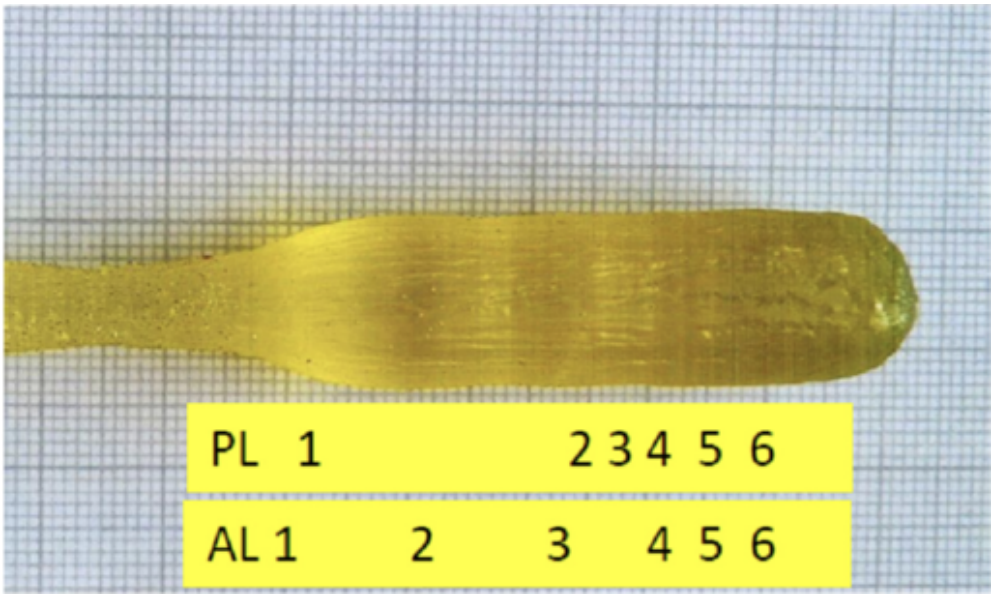

FIGURE 6.10: Photograph of the GAGG:Ce,Mg crystal grown using the Czochralski method. Positions of plates used for characterization experiments (PL1–6) and compositional analysis (AL1–6) are indicated. From reference [84].

to PL6, was cut from the ingot at the positions indicated in Fig. 6.10. The plates were used in optical, luminescence and scintillation measurements. Another set of plates, AL1 to AL6, was prepared for composition analysis, done at FZU Prague. Plates AL4, 5, 6 were the same as PL4, 5, 6. All the plates were 1.2 mm thick with both faces polished. Starting from PL3, towards the crystal end, tiny, hardly visible inclusions appear in the crystal volume. The chemical analysis of AL1–6 plates (Table 6.6) was made using the electron microanalyzer Jeol JX-8230 with energy-dispersive spectrometer Bruker QUANTAX 200 using software Esprit 2.2. X-Ray diffraction (XRD) analysis of a sample cut just behind the AL6 plate confirmed that the cubic garnet structure matches the 04-023-5738 card in the database PDF4+, corresponding to composition $Gd_{2.985}Ce_{0.015}Ga_3Al_2O_{12}$ without the presence of any parasitic phases.

The detailed Rietveld fitting in the crystallographic computing system Jana2020 revealed two garnet phases with very close elementary cell parameters:

- a1 = 12.28279 $\pm$0.00005 Å (80% volume)
- a2 = 12.29436 $\pm$0.00013 Å (20% volume)

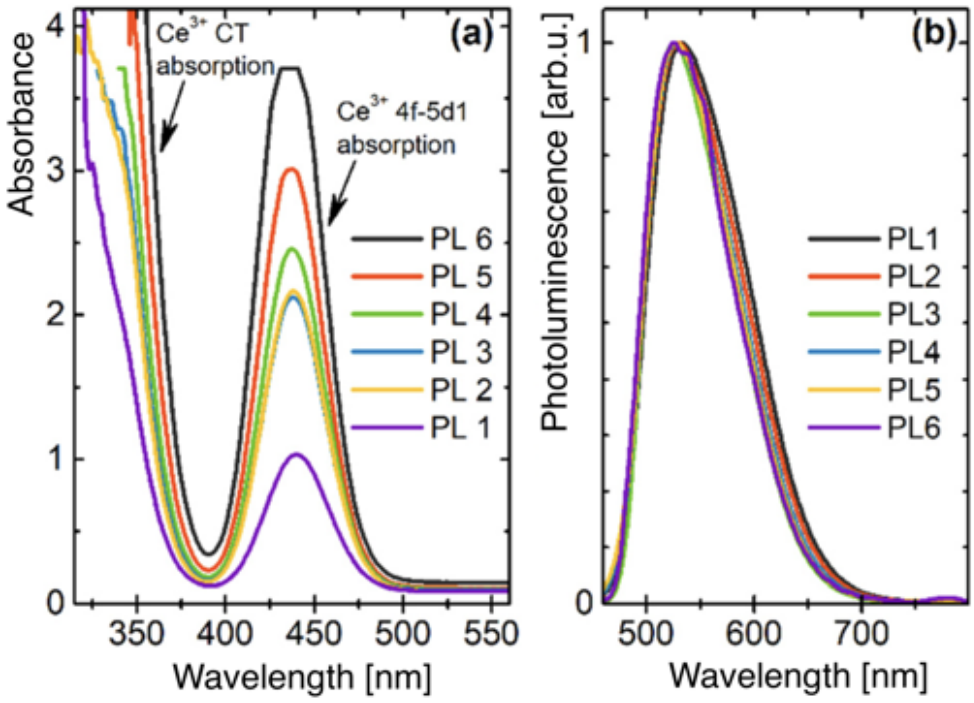

FIGURE 6.11: Photoluminescence spectra (left) and absorbance spectra (right) of the samples tested. From reference [84].

The XRD analysis performed in the crystal ingot at the end part adjacent to the position of AL6 did not reveal any parasitic phases. This might indicate the presence of micron-scale regions with two certain Al/Ga ratio which has been discussed in literature [52, 50, 85]. The results obtained would, thus, constitute the first experimental confirmation.

Consuming nearly all the melt in the growth process, the content of the Ce dopant and Mg codopant along the ingot growth axis increased due to their segregation coefficients in the GAGG host being lower than 1. That allowed fabricating a set of GAGG:Ce,Mg samples with the content of Ce increasing in samples from PL1 to PL6 in a wide range up to heavy doping corresponding to the substitution of ∼1% of cations by Ce and Mg.

6.2.2 Absorption and Photoluminescence Spectra

The measurements of this section were performed by the Institute of Physiscs of the Czech Academy of Sciences.

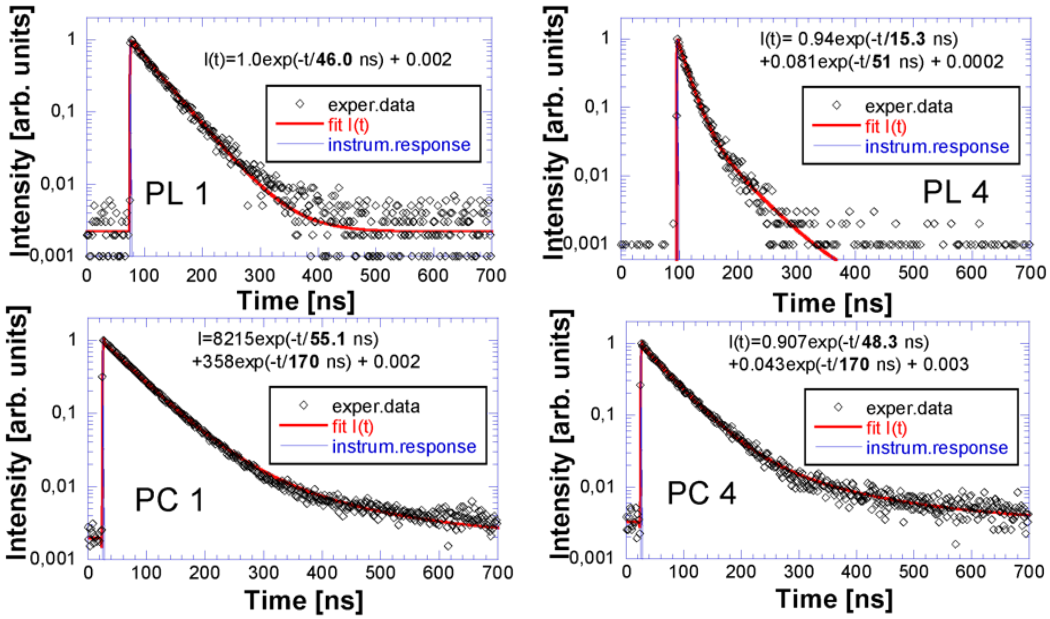

FIGURE 6.12: Top row: time-resolved photoluminescence of PL1 (left) and PL4 (right). PL1 has an exponential scintillation whereas PL4 shows 2 components, one much faster down to 15 ns. Bottom row: time-resolved photoluminescence of two samples with similar composition to PL1 and PL4 but without Mg co-doping. the two do not show any reduction of the $\sim$ 50 ns component, while exhibiting an additional long decay component of 170 ns. From reference [84].

The photoluminescence and absorbance spectra are presented in Fig 6.11. Along the ingot, there is a progressive increase in both the Ce^{3+} 4f-5d_1 absorption and the Ce^{4+}-related charge transfer absorption band. This is in line with the increase of Ce and Mg observed along the ingot (Table 6.6).

The photoluminescence spectra with excitation of 452 nm are compatible with the literature values discussed in Sec. 6.1.2. The emission blue-shift observed along the ingot is due to the increase in Ga content [73].

The time-resolved photoluminescence of PL1 and PL4 are visible in Fig. 6.12, top row. The profile of PL1 is exponential with a characteristic decay time of 46 ns, whereas that of PL4 is strongly non-exponential with a fast and a slow component of 15 ns and 51 ns, respectively.

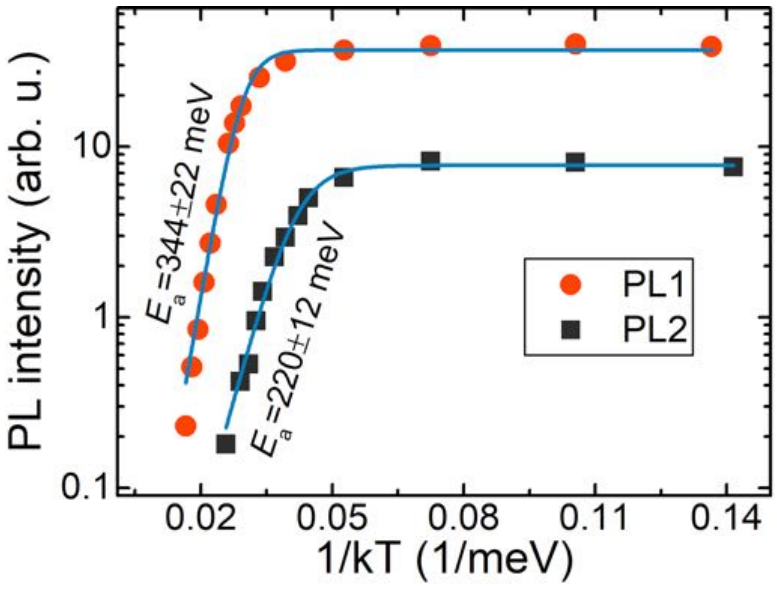

FIGURE 6.13: Temperature dependence of the photoluminescence intensity of plates PL1 and PL6 under 442 nm excitation. From reference [84].

To exclude the Cerium alone being the cause of this acceleration, a new set of samples were prepared with the same Cerium concentration but without Magnesium, labelled PC1,2,3,4,5,6. The samples PC1 and PC4 do not show any reduction of the $\sim$ 50 ns component, while exhibiting an additional long decay component of 170 ns. Therefore, it is the increase of both Ce and Mg that leads to the acceleration of the photoluminescence time profile: as first observed and explained in [86, 87], the ions of Ce^{3+} perturbed by neighbouring Mg^{2+} offer fast non-radiative recombination channels, accelerating the scintillation.

Temperature Dependence of Photoluminescence

The temperature dependence of the photoluminescence was measured at the Institute of Photonics and Nanotechnology, Vilnius, Lithuania.

The photoluminescence intensity at different temperatures is presented in Fig. 6.13 for PL1 and PL6. It can be properly described by a single activation energy E_a according

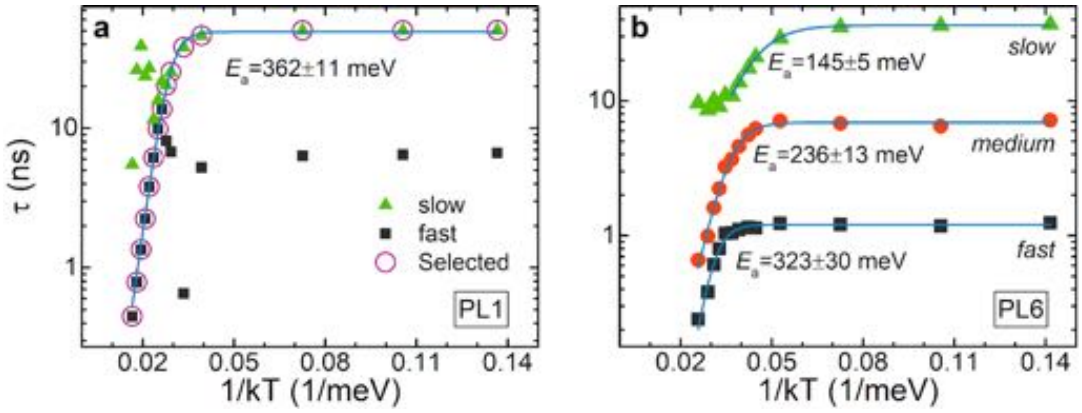

FIGURE 6.14: Temperature dependence of photoluminescence decay times in sample PL1 (a) and PL6 (b) as discussed in the text. Solid lines represent approximations using Eq. 6.1. The fitted activation energies are indicated. From reference [84].

to:

$$V(T) = \frac{V_{lowT}}{1 + A\, e^{-\frac{E_a}{k_B T}}}, \tag{6.1}$$

where V_{lowT} is the constant PL intensity at low temperature and A is a fitting constant. The activation energy E_a for emission quenching decreases along the ingot from 344 ± 22 meV to 220 ± 12 meV in PL1 and PL6, respectively.

The integrated photoluminescence decay of PL1 can be parameterised by a single exponential component at room temperature (Sec 6.2.2, Fig 6.12) and above, whereas it requires 2 distinct components below that. Applying Eq. 6.1 to the component with the largest fraction of emitted photons (see Fig. 6.14, left) gives an activation energy E_a of 362 ± 11 meV, compatible with the one obtained for the integrated luminosity (344 ± 22 meV). Conversely, the photoluminescence decay of PL6 exhibits 3 components at all temperatures (Fig. 6.14, right), with activation energies of 145 ± 5 meV,

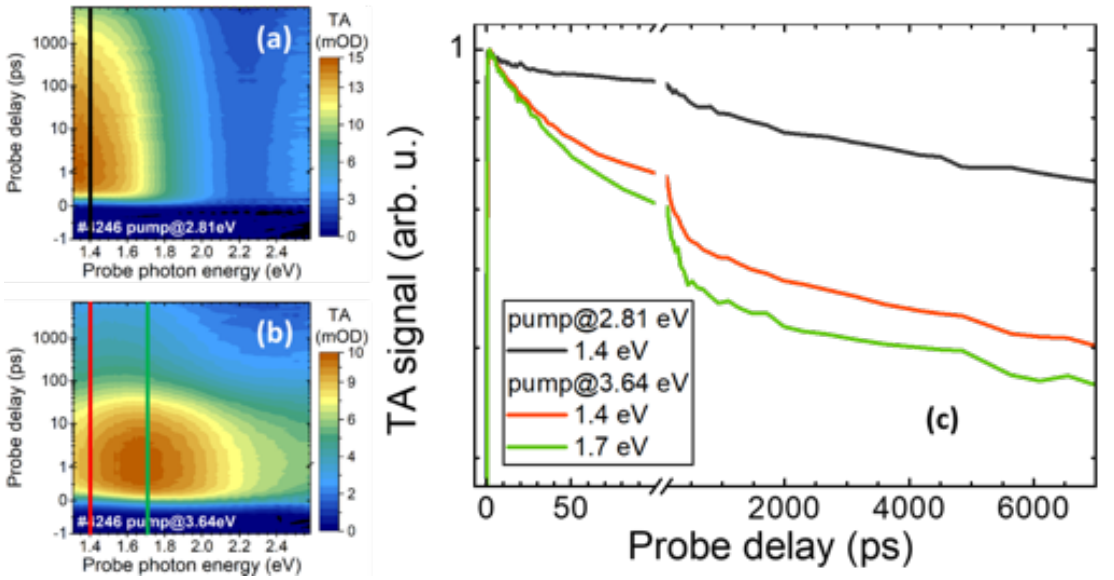

FIGURE 6.15: Left: data carpets for the transient absorption of PL2 as a function of the probe photon energy and the delay between pump and probe pulses at excitation of Ce3+ ions to their lowest excited level 5d1 (a) and the second lowest level 5d2 (b). Right: transient absorption decay kinetics (c) for pump and probe photon energies as indicated in the legend and marked by vertical lines of corresponding colour in (a) and (b). From reference [84].

236 ± 13 meV, and 323 ± 30 meV for the slowest, medium, and fastest component, respectively. Note that the medium component, which has the largest fraction of emitted photons at all temperatures, shows an activation energy compatible with the one obtained for the integrated luminosity.

The presence of multiple components at all temperatures excludes thermal quenching from the causes of the photoluminescence acceleration.

6.2.3 Transient Absorption

The transient optical absorption of the samples was measured at the Institute of Photonics and Nanotechnology, Vilnius, Lithuania.

Fig. 6.15 shows the measurement of PL2 for the excitation from Ce^{3+} 4f to $5d_1$ and $5d_2$ (a and b) and the time profile for a few selected probe energies (c).

Upon direct excitation from 4f to $5d_1$ (2.81 eV) a single absorption band is visible, peaking at approximately 1.4 eV. The rise time for all the samples is below the system resolution of 250 fs. This band is due to electrons populating the $5d_1$ state, which recombine radiatively on the timescale of ns leading to the photoluminescence.

Upon direct excitation from 4f to $5d_2$ (3.64 eV) the transient absorption features 2 bands, one at 1.4 eV and one at 1.7 eV extending towards higher energies with increasing Mg codoping. The first one is again due to electrons populating the $5d_1$ state, but it shows a measurable rise time (10%-100%) which decreases along the ingot from 2 ps to 1 ps. The slower rise time with respect to 4f-$5d_1$ pumping is due to the intracenter relaxation time necessary for electrons to transition from the $5d_2$ state to $5d_1$. The intrinsic decay time between the two states is 0.52 ps [54], but trapping of the carriers leads to larger rise times; Mg co-doping mitigates the effect of trapping reducing the rise time. These results are qualitatively in line with the literature on Mg-codoped GAGG, albeit the rise times are quantitatively faster. [54]

The second band (1.7 eV) is due to electrons relaxing via extended delocalised states in the conduction band. Due to this second band, the first band at 1.4 eV shows a time profile markedly non-exponential, decaying faster in the first tens of ps than in the case of 2.81 eV excitation (Fig. 6.15, (c)). Moreover, the second band disappears swiftly after a few tens of ps, leaving space to the tail of the first band, i.e. of the electrons relaxed to $5d_1$; at that point, the first band decays as in case of the 4f to $5d_1$ (2.81 eV) excitation. These results hint at the second band (1.7 eV) being related to electrons recombining non-radiatively, i.e. a luminescence quenching which.

6.2.4 Light Output

The samples were wrapped in Teflon and placed standing on their 1x1 mm^2 face coupled to the PMT via Rhodorsil optical grease. The photopeak of PL6 was not resolvable from the background spectrum due to the low output and poor intrinsic resolution, made worse by the PMT's QE not suiting the GAGG emission. However, plotting the events amplitude against their charge made possible separating the desired events from the background (Fig. 6.16). This approach was first tested and validated with the commercial samples.

TABLE 6.7

Sample	Photons Output [MeV^{-1}]	±	$\tau_{d,eff}$ [ns]	±	CTR [ps]	±
C&A GFAG	20 500	1 000	41	3	127	3
Fomos GAGG	28 300	1 400	73	3	154	3
ILM GAGG	21 000	1 100	40	3	133	3
PL1	12 000	600	26	3	143	3
PL2	7 600	380	14	2	149	3
PL3	5 200	260	12	1	141	3
PL4	3 900	190	9	1	136	5
PL5	2 300	230	5.2	0.5	148	5
PL6[a]	500	300	0.7	0.5	170	10

[a]photopeak not well-resolved

The measured light outputs are reported in Table 6.7. The difference in the commercial samples from Table 6.2 is mainly[2] due to the geometry. The tested samples feature light output between 2 and 40 times lower than commercial ones. The light output decreases with larger Ce-Mg concentration, confirming the light quenching predicted in Sec. 6.2.3.

It must be noted that the surface state of the PL samples was different from the commercial ones (see Sec. 6.2.1). Having only 2 polished lateral faces is expected to reduce the output, although by an unknown amount in GAGG; studies with LYSO observed up to a factor 2 [39].

6.2.5 Scintillation Kinetics

Scintillation kinetics was measured with the X-ray TCSPC set-up (Fig. 6.17, left) and the decay times are reported in Table 6.8. The decay is accelerated with the increasing doping level, in agreement with photoluminescence. All the PL samples exhibit decay times considerably faster than that of the commercial samples and no slow component is observed above 80 ns. The calculated rise time is below the instrumental time resolution for all the new samples.

The scintillation kinetics of the PL samples was additionally measured with 511 keV γ excitation, observing the same quenching (Fig. 6.17, right). The decay times (Table 6.8, below the X-rays values, in italic) are acceptably close to the X-ray values, but their

[2]The commercial samples tested here were not purchased at the same time as in Sec. 6.1, and it is not possible to exclude differences in composition.

TABLE 6.8: Scintillation rise and decay times and relative abundances under X-ray and excitation. The rise time uncertainty is 25 ps.
The values measured under 511 keV excitation are reported for each sample on a second line and italic.

Sample	τ_r	$\tau_{d,1}$	R_1 %	$\tau_{d,2}$	R_2 %	$\tau_{d,3}$	R_3 %	$\tau_{d,eff}$
C&A GFAG	32	6.0	4.5	45	69.2	222	26.3	41 ± 4
ILM GAGG	37	4.0	3.2	40	56.4	138	40.4	40 ± 4
Fomos GAGG	30	2.2	0.5	53	41.7	166	57.8	73 ± 4
PL1	< 25	2.5	3.3	25	48	79	48.8	26 ± 2
511 keV	-	-	-	*25*	*44.6*	*78*	*55.4*	*40 ± 4*
PL2	< 25	2.1	7.2	17	54.6	66	38.2	14 ± 1
	-	*3.0*	*5.4*	*21.3*	*64.5*	*76*	*30.1*	*19 ± 2*
PL3	< 25	1.6	6.2	13	47.5	46	46.3	12 ± 1
	-	*2.3*	*4.4*	*15*	*52.6*	*52*	*43.0*	*16 ± 1*
PL4	< 25	1.5	9.2	11	53.9	45	36.9	8.6 ± 0.8
	-	*2.3*	*10.7*	*12*	*60.8*	*55*	*28.5*	*9.9 ± 0.8*
PL5	< 25	1.0	11.0	7.1	51.8	41	37.2	5.2 ± 0.8
	-	*1.2*	*11.1*	*6.8*	*55.9*	*36*	*33.0*	*5.5 ± 0.8*
PL6	< 25	0.2	19.5	1.5	53.0	14	27.5	0.7 ± 0.5
	-	*0.4*	*1.5*	*1.7*	*56.6*	*15*	*41.9*	*2.4 ± 0.5*

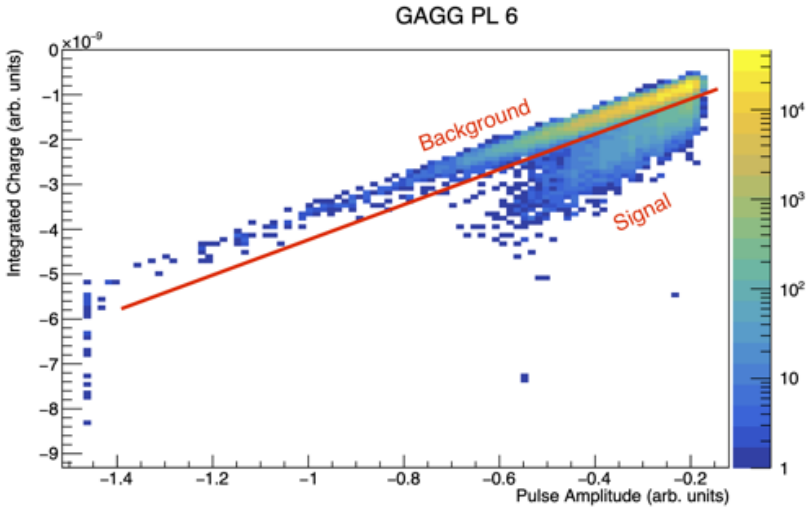

FIGURE 6.16: 2D-histogram of the integrated charge against the pulse amplitude upon ^{137}Cs excitation. The low output and poor intrinsic resolution of the PL6 sample did not allow a clear separation between signal and noise with only the integrated charge information.

fractions shift in favour of the slower components. No rise time is reported due to the insufficient statistics acquired.

Notably, X-rays produce a scintillation faster than 511 keV γ photons, and these, in turn, faster than the resonant excitation of 4f-5d$_{1,2}$ (Fig. 6.18). The effect was observed experimentally and explained theoretically [79, 88]: X-rays and 511 keV γ feature a reduced range of the primary photoelectron increasing the spatial density of e-h pairs and, therefore, the probability of dipole-dipole interaction and Auger processes between 2 excitons leading to the non-radiative recombination of one. The results are in line with literature inasmuch as the density quenching of the luminescence is most intense with few-keV X-rays. Photons of several hundreds of keV were found to produce the slowest scintillation in YAG:Ce [79], possibly due to the role of traps not compensated by the Auger quenching. The addition of Ga in GAGG lowers the bottom of the conduction band inhibiting such traps, which could explain why the decay times with 511 keV are faster than with resonant excitation.

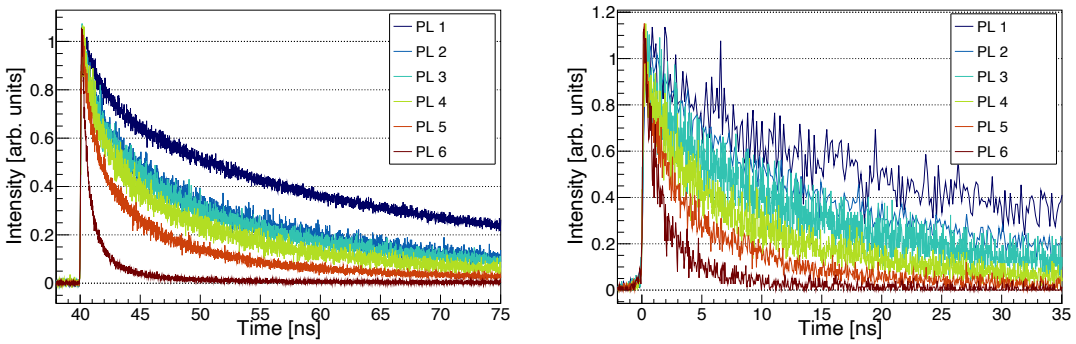

FIGURE 6.17: Scintillation kinetics of the 6 samples under X-rays (left) and 511 keV γ excitation. From reference [84].

6.2.6 Coincidence Time Resolution

The CTR measured on the NINO-based set-up is reported in Table 6.7. The PL samples from 1 to 5 achieve CTR between 136 and 149 ps. PL6 performs worse but the unresolved photopeak makes selection difficult and the poor signal-to-noise ratio increases the electronics contribution. C&A and ILM achieve 127 and 133 ps, respectively, whereas Fomos settles at 154 ps. The PL samples lie between the three, showing their competitive time resolution.

6.2.7 Scintillation Acceleration: Conclusions and Outlook

All the results demonstrate that the increase in both Ce and Mg dopants concentration accelerates the luminescence of GAGG. The acceleration was observed under X-rays, γ photons, and with laser excitation (see for instance Fig. 6.18). While part of the acceleration observed with X-rays is due to Auger effects between e-h pairs caused by the large ionization density, the power of the laser is not sufficient to induce such effects, nor local thermal effects. Since the acceleration was observed even with resonant 4f-5d_1 excitation at low temperature when no electron release from the 5d_1 state of Ce^{3+} can take place, the acceleration can only be explained by non-radiative transitions.

Recent studies point to the fact that Mg^{2+} ions neighbouring the Ce^{3+} could perturb the energy level and induce non-radiative recombination [87]. Transient optical absorption measurements support the hypothesis of additional recombination channels, manifesting in the band peaking at 1.7 eV and extending towards higher energies with increasing dopants content.

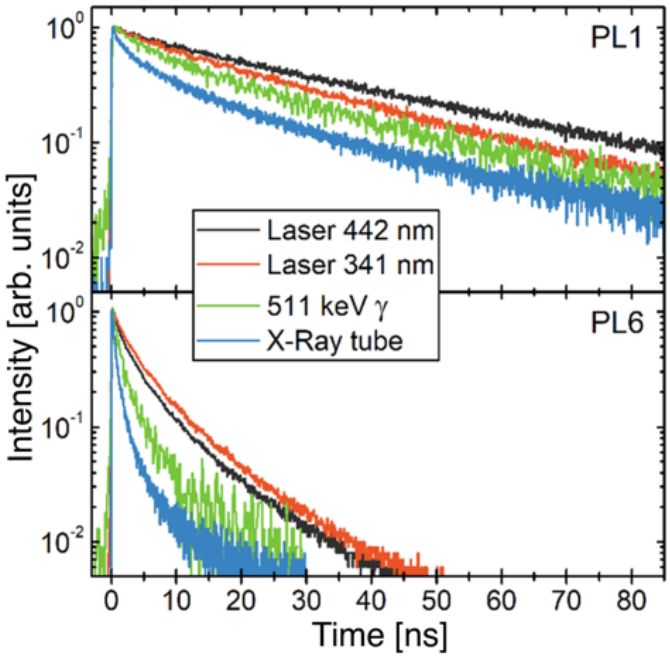

FIGURE 6.18: Decay kinetics of the PL1 and PL6 samples for the 4 excitation sources employed in the study. A significant acceleration in light output is visible with increasing doping. X-rays and 511 keV γ photons feature an additional acceleration of the decay time due to the larger ionization density of the photoelectrons produced, leading to non-radiative recombination of e-h pairs via Auger effect and giving access to the e-h pairs to alternative recombination channels. From reference [84].

The light output measurements confirm a reduction of the scintillation yield correlated with the acceleration.

The light output against the effective decay time with X-ray excitation are plotted in Fig. 6.19. The ILM and C&A samples feature a larger $\frac{\tau_{d,eff}}{LO}$ ratio (red dotted line) than Fomos' sample (blue dotted line), as already observed in Fig. 6.7. The PL samples lie between the two. This is in line with the CTR results of Table 6.7, where the PL samples achieved CTRs intermediate between the commercial samples.

Notably, the samples $\frac{\tau_{d,eff}}{LO}$ ratio are well described by a single line, meaning that the

light quenching does not improve nor worsen the timing performance of the PL sets[3]. Leaving the timing unaltered, the quenching observed appears as a useful tool to finely tune the scintillation properties according to the application.

Finally, it must be noted that the scintillation and photoluminescence time profiles of the PL samples require up to 3 components to be described. Additional components on top of the intrinsic Ce one were observed in CeF_3 [89]. There, the fast components with focused lasers are caused by the interaction of neighbouring Ce^{3+} ions, and the discrete number of decay components is related to the discrete set of distances available in the crystal lattice for Ce ions. Somewhat similarly, the additional components with different energy barriers observed in the study might be related to the set of possible distances of Ce^{3+}-Mg^{2+} pairs: at 1at% the average Ce-Ce pair distance is 13Å; Mg ions added at similar or lower concentration could constitute Ce-Mg pairs at 6 Å(see Sec. 3.8 of [84]).

Thinking about the applications, on the one hand, the light output reduction increases the Poisson contribution to the energy resolution. This could prevent the use of these compositions in low-energy applications. On the other hand, the energy deposition in HEP is often large enough to maintain a sufficient signal-to-noise ratio with the outputs observed so far. Moreover, large light outputs mean high currents through the photodetector, which can degrade the linearity in the response and reduce the detector's lifetime. Employing optical filters to dampen the the output would degrade the time resolution since the scintillation rise and decay time would be unchanged. It is thus clear that lower outputs could actually be favourable for HEP.

Outlook

The studies above confirmed GAGG as a solid candidate for the upgrade of the LHCb ECAL and detectors at future colliders. The intrinsic timing performance is competitive with LYSO crystals, while featuring higher radiation hardness, tested up to 1 MGy with protons. Moreover, GAGG has a melting temperature lower than other garnets (e.g. YAG, or LuAG), which helps preventing Magnesium evaporation from the melt, making GAGG suitable for heavy Ce-Mg codoping.

A few crucial points are still to tackle. First, segregation of Cerium and Magnesium in the melt mandates some optimisation of the growth procedure in order to grow uniform

[3]It is worth noting instead that the reduction in light output for the first study on the commercial samples was being followed by an even larger acceleration of scintillation, i.e. the photon time-density was increasing and the time resolution improving (Fig. 6.7).

and large-size ingots with high-doping compositions. As observed in the test ingot, Ce and Mg tend to stay in the melt, distributing inhomogeneously along the ingot axis.

Second, radiation hardness of these new compositions must be tested. Recent results highlighted that the irradiation by heavy nuclei could introduce F-type centres near the Ce ions inhibiting the hole re-charge thus shifting the Ce^{4+} valence back to Ce^{3+} and possibly modifying the scintillation properties [90]. Preliminary test of the commercial samples with 24 GeV protons at IRRAD did not show any significant change in the scintillation properties, but further tests are required.

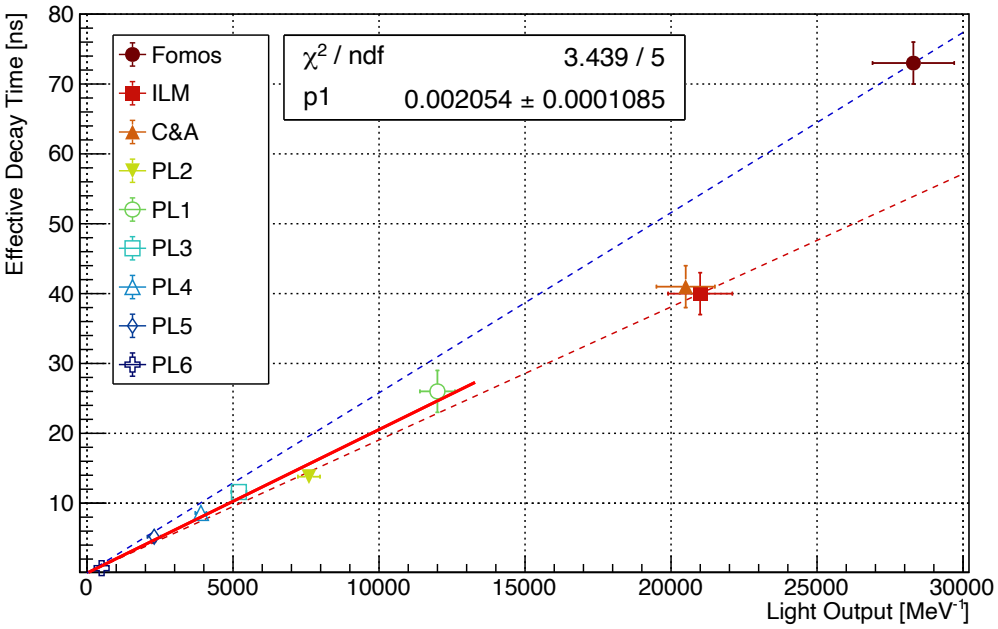

FIGURE 6.19: Effective decay time with X-ray excitation and light output of the crystals. The C&A and ILM samples feature a $\frac{LO}{\tau_{d,eff}}$ ratio (red dotted line) better than Fomos' (blue dotted line). The PL samples lie on the same isoline (see the linear fit), between the two of the commercial samples. The results suggest that the variation in the scintillation parameters of the PL samples does not affect the CTR, which is expected to be in between that of the commercial samples, as experimentally observed (Table 6.7).

Chapter 7

Polysiloxane Scintillators

7.1 Radiation Tolerant Plastic Scintillators

The inorganic scintillating garnets discussed in the chapter above offer radiation hardness up to 1 MGy matching the requirements of the innermost region of the LHCb ECAL. On the other hand, the production price is prohibitive for large volumes and cost-effective scintillators radiation tolerant to a few hundreds of kGy are sought after.

In Part III, commercial plastic scintillating fibres (Kuraray SCSF-78) were employed to assemble SPACAL prototypes. Although the target performance was achieved, the polystyrene core casts doubts on the radiation tolerance of these fibres. An option to mitigate the effects of radiation damage is using wavelength-shifters with larger Stokes shift e.g. 3-hydroxyflavone, although this comes at the expense of lower light yield and slower scintillation rate, as in Kuraray SCSF-3HF [91]. Another solution would be to find a radiation tolerant host material to replace Polystyrene.

Polysiloxane polymers were observed to undergo minimal changes in transmission upon exposure to $\sim$100 kGy dose with ^{60}Co γ source [92]. They were studied aiming at the fabrication of elastomeric organic scintillators for the detection of ionizing particles and neutrons with good light yield, mechanical robustness, and radiation resistance [93, 94].

The Si-O bond of these polymers offer mechanical flexibility and a dissociation energy of 452 kJ mol^{-1} larger than C-C (347 kJ mol^{-1}) or C-O (358 kJ mol^{-1}) bonds. Samples irradiated with ^{60}Co γ source up to 54 kGy were found to lose light yield over time like samples not irradiated, owing to stability of the chemical compositions; conversely, commercial PS-based plastics were found to lose light yield exponentially as function

of the irradiation dose. Finally, ion beam induced luminescence (IBIL) was used to study the radiation damage with 2 MeV proton beams optimising different resins. [95]

Polysiloxane-based scintillators are a promising solution for moderate radiation environments and R&D was started in collaboration with multiple partners to produce compositions matching the requirements of the LHCb ECAL UII project. Although the collaboration is still in a preliminary phase, a few samples from the Laboratori Nazionali di Legnaro are discussed in the next section.

TABLE 7.1: Scintillation parameters of the LNL samples. Uncertainty on the light output is ±3%, on decay time 0.3 ns, on the rise time 25 ps.

Sample	Light Output [photons/MeV]	τ_d [ns]	$\tau_{r,1}$ [ps]	R_1 %	$\tau_{r,2}$ [ps]	R_2 %
PSS100 PPO 2% LV 0.02%	4 320	7.7	5	60	1 380	40
PSS100 PPO 1% LV 0.01%	4 080	8.3	8	46	1 400	54
PVP-MPS	4 160	8.3	50	50	1 420	50
ASP 1120	2 880	7.2	70	54	1 420	46

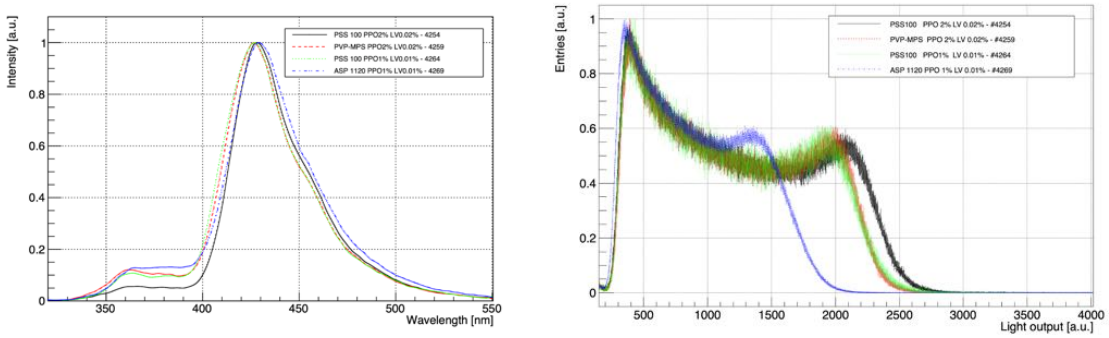

FIGURE 7.1: Samples from the LNL. Left: Photoluminescence spectra with excitation light at 300 nm. Visible are the LV emission (∼425 nm) and the PPO emission (<400 nm). Right: light output spectra. Due to the low effective atomic number Z of the materials, no photopeak is observed. See also Table 7.1.

7.2 Polysiloxane Scintillators of the Laboratori Nazionali di Legnaro

The set of samples comprised cubes of 10x10x10 mm^3 with 2 opposite faces mirror-like for the transmission measurements produced by Dr. Carturan (Laboratori Nazionali di Legnaro). Three different resins were tested – PSS100, PVP-MPS, and ASP 1120 – with PPO and Lumogen Violet (LV) as dyes. The samples had 2 opposite mirror-like faces for the transmission measurements and the remaining ones ground.

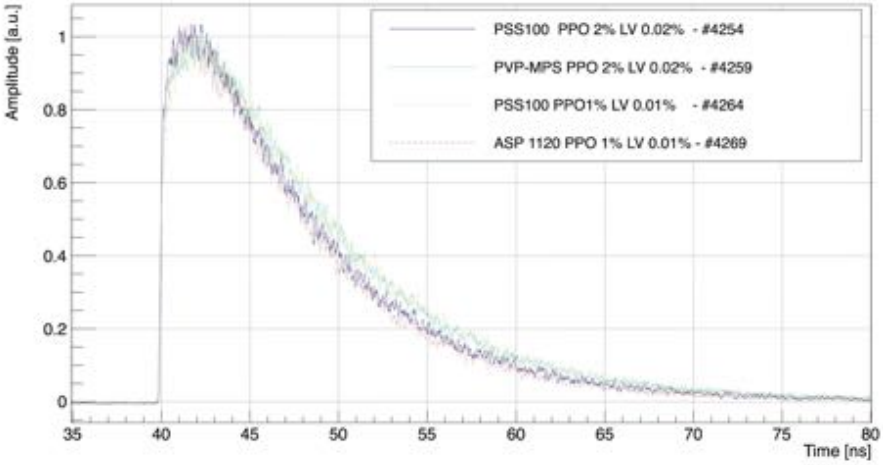

FIGURE 7.2: Scintillation kinetics of the samples under X-rays excitation.

7.2.1 Absorption and Photoluminescence Spectra

Photoluminescence with excitation at 300 nm is reported in Fig. 7.1, left. The LV emission is peaked at approximately 425 nm, whereas the first dye emission is visible below 400 nm. ASP resin's emission is the most red-shifted. Increasing the PPO levels in PSS100 from 1% to 2%, leads to a red-shift of a few nm. A similar red-shift is observed in transmission. The surface state of the ASP sample was more ground than the others.

7.2.2 Light Output

The light output of the samples wrapped in Teflon and coupled with glycerine (n=1.47) to the PMT was measured with a ^{137}Cs source, identifying the position of the Compton edge peak (477 keV) instead of the photopeak (see Table 7.1 and Fig. **??**, right). All the samples showed a light output above 4000 photons/MeV but for the ASP resin (2880 photons/MeV).

7.2.3 Scintillation Kinetics

The scintillation kinetics with the pulsed X-rays TCSPC set-up (Fig. 7.2) was well described by a single decay time of about 8 ns and two rise times, a fast one below 100 ps and a slow one of the ns order at least partially caused by the optical photons travel spread due to the large geometry of the samples.

7.2.4 Preliminary Conclusions

The samples tested have light output and decay time in the same order of magnitude of commercial PVT-based plastics like EJ-200. Amongst them, the PSS 100 samples with 2% PPO features larger light output and more light emitted with fast rise time, suggesting better timing. The results are very preliminary but just as much promising. Further R&D is necessary to tune the scintillation parameters in order to improve timing properties, and radiation hardness of the samples to MIP hadrons is to be experimentally validated.

Part III

Testbeam Campaign

Testbeam Campaign

Testing prototypes is a crucial step to develop particle detectors. Facilities like DESY or CERN offer particle beams, said testbeams, with known momentum, composition, and rate to assess the prototypes' performance.

The following chapters present the studies on SPACAL prototypes performed in over 18 weeks of beam time for the LHCb ECAL Upgrade:

- Chapter 8 describes the testbeam facilities, the experimental set-up, and the data analysis techniques employed;
- Chapter 9 presents the results on the SPACAL made of Tungsten absorber and Garnet crystal fibres;
- Chapter 10 presents the results on the SPACAL made of Tungsten absorber and polystyrene fibres;
- Chapter 11 presents the results on the SPACAL made of Lead absorber and polystyrene fibres.

The LHCb upgrade timeline demanded a prioritisation of the layouts to test and the studies to perform.These chapters do not aim to be a comprehensive nor systematic study of the performance of the SPACALs. Instead, their content mirrors the *in itinere* evolution in the understanding of the prototypes and of the R&D focus in order to demonstrate the SPACAL being a valid baseline solution for the upgrade.

Part of Chapter 9 has been published in Nuclear Instruments and Methods in Physics Research Section A, *"Performance of a spaghetti calorimeter prototype with tungsten absorber and garnet crystal fibres"*, reference [96].

The solutions employed and performance here obtained are relevant for detectors at future colliders and fixed-target experiments at the intensity frontier. [97, 98, 99, 100]

Chapter 8

Materials and Methods

8.1 Testbeam Facilities

Few facilities worldwide provide beams with particles and momenta in the range faced by the LHCb ECAL. The measurements discussed in the next chapters were performed at DESY II and CERN SPS, here described.

8.1.1 DESY II

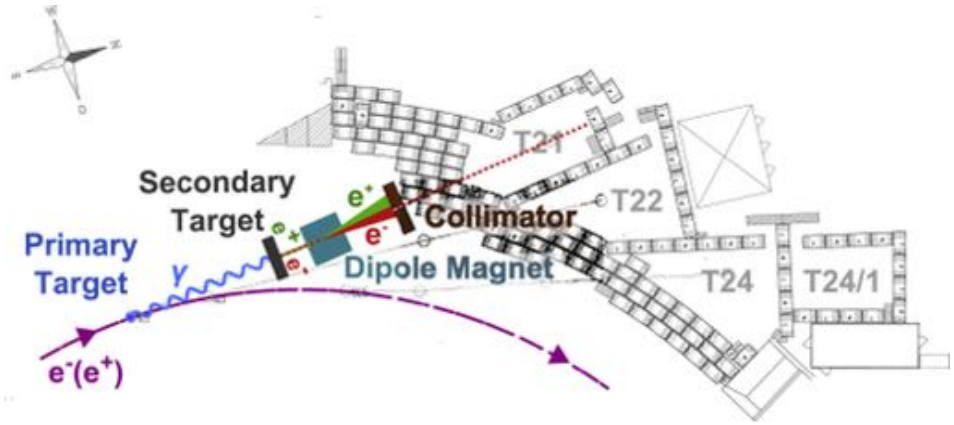

FIGURE 8.1: Schematics view of the DESY II Test beam facility. From reference [101].

The Deutsches Elektronen-Synchrotron (DESY) in Hamburg operates a testbeam facility with 3 beam lines: TB21, TB22, TB24 [101]. The DESY II synchrotron provides the primary beam. Bremmstrahlung radiation produced interacting with a target is steered

towards a secondary target, generating a continuous flux of electrons or positrons of 1-6 GeV/c momentum (see Fig. 8.1).

A dipole magnet is used to select the momentum desired. The momentum spread $\frac{\Delta p}{p}$ in TB21 was measured to be constant at (158 $\pm$ 6) MeV/c. Unlike the other lines, TB24 features two dipole magnets. This is expected to reduce significantly the momentum spread, although the facility never measured it. All the testbeams in DESY were performed at the TB24 beamline.

8.1.2 CERN SPS

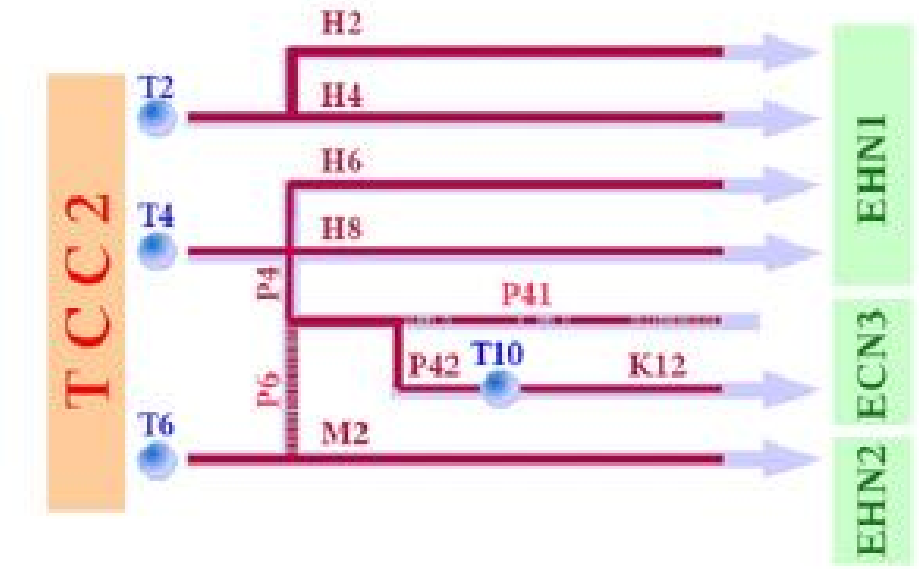

FIGURE 8.2: Schematics of the CERN SPS North Area beamlines, showing the three targets (T2,4,6) and the test beamlines they feed (H2, H4, H6, H8).

The CERN SPS is employed both as injector for the LHC and to supply the North Area on Prevessin with several testbeams. The SPS primary proton beam collides with targets, and the secondaries produced are selected with a series of magnet spectrometers (see Fig. 8.2). This allows the facility to offer numerous particle beams including leptons ($e^{\pm}$, $\mu^{\pm}$) and hadrons ($\pi^{\pm}, K^{\pm}, p$) with momenta ranging from a few tens up to several hundreds Gev/c. The particles are provided in spills of a few seconds.

The momentum spread $\frac{\Delta p}{p}$ can vary significantly amongst beamlines and particle types. Electron beams with spread below $\pm 1\%$ at 100 Gev/c are achievable in H2 and H4.

8.2 Testbeam Set-up

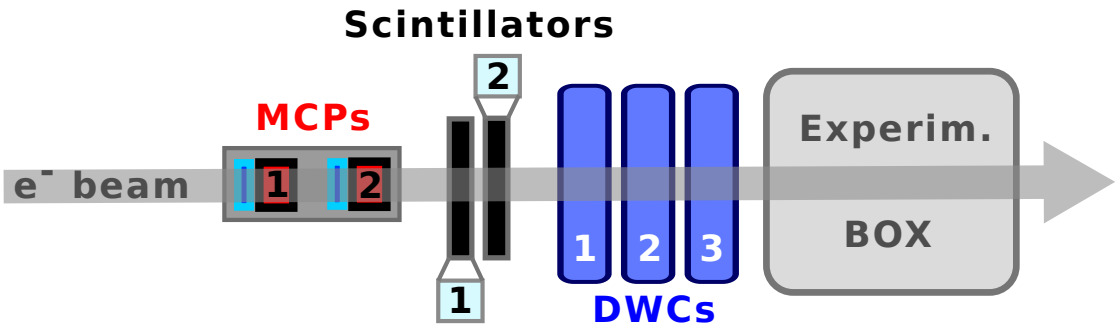

FIGURE 8.3: Test beam setup. The electron beam moves from left to right, two MCPs provide the time reference, two scintillating pads the trigger signal, and three DWCs the tracking information. The experimental box contains the prototype and the rotating steppers.

The testbeam setup is sketched in Fig. 8.3 and shown in Fig 8.4 at SPS H2.

The prototype was mounted on two steppers allowing it to rotate horizontally (yaw) and vertically (pitch). The rotation of the prototype is defined as yaw + pitch hereafter, e.g. 3°+3°. The assembly was placed inside a light-tight box installed on a table moving in the plane orthogonal to the beam. The uncertainty on the incidence angle was estimated to be $\pm 0.15°$ both horizontally and vertically in DESY thanks to a laser system aligned with the beam provided by the facility. Cables of 0.8 m were employed inside the box to connect the prototype to a patch panel on the box surface. Cables of 3 m were used from the patch panel to the electronics rack.

The Data Acquisition system (DAQ) comprised several electronics module. The trigger logic was managed via NIM modules. A high voltage power supply by CAEN was employed to bias the detectors and controlled remotely via the CAEN GECO2020 interface. The photodetectors' signals of the prototype was input to 2 VME modules alternatively:

LeCroy 1182 ADC module employed to integrate the input signals over a 400 ns gate for the energy measurements.

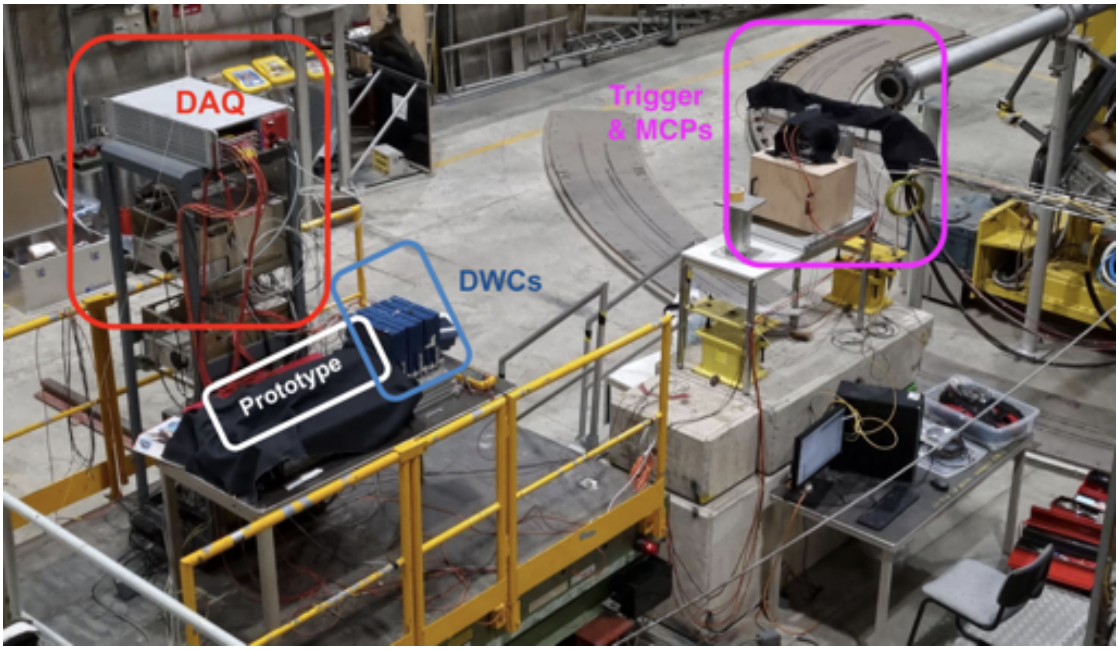

FIGURE 8.4: Picture of the testbeam set-up of Fig. 8.3 taken in SPS North Area beamline H2. The experimental box is missing but its position is highlighted in white.

CAEN V1742 Digitiser module based on the DRS4 chip [69] sampling the waveforms with a rate up to 5 Gs/s and 500 MHz bandwidth for timing measurements; a custom calibration based on [102] reduced the interchannel time jitter < 5 ps.

Attenuators ranging from 10 to 70dB were used if needed to match the input dynamic range of the electronics.

Beside – and in front of – the experimental box:

The hardware trigger was provided by 2 plastic scintillating pads in coincidence.

The tracking was given by 3 delay wire chambers (DWC) employing a mixture of Ar/CO_2 gas and read out by a CAEN TDC V1290N.

The time reference was given by 2 microchannel plate detectors (MCP) along the beam line. The timestamp of each MCP was computed by constant fraction discrimination (CFD, see Sec. 8.4) at 30% on the digitised waveform and the average of the 2 timestamps was used as time reference. The time resolution of the reference was

measured run by run with the two MCPs in coincidence, ranging from 13 to 15 ps (standard deviation).

8.3 Photomultipliers

TABLE 8.1: Table of the PMTs used. All the PMTs are from Hamamatsu Photonics K.K.

PMT	Type	Size	Dynode stages
R12421	Linear-focused	⌀ 14.3 mm	10
R7899-20	Linear-focused	⌀ 25 mm	10
R7600U-20	MCD	30x30 mm^2	10
R11187	MCD	26x26 mm^2	8
R14755U-100	MCD	⌀ 16 mm	6

The photomultiplier (PMT) converts optical photons into an electronic signal. Numerous PMTs were employed throughout the testbeams (Table 8.1).

Linear-focused PMTs offer excellent linearity with fast time response, thus being suitable for energy resolution measurements [19]. The R7899-20 – the PMT of the current LHCb ECAL – fits the cell size of the Lead/Polystyrene SPACAL (see Chap. 11.2). The smaller cell size of the Tungsten/GAGG prototype required using the R12421 PMT (see Chap. 9.2).

Timing measurements could be carried out equipping only 1 cell per side, thus relaxing the geometrical requirements of the PMTs. Metal channel dynode (MCD) PMTs feature a dynode structure consisting of extremely thin electrodes stacked in close proximity to keep the electron path length very short, thus ensuring excellent time characteristics and stable gain [19]. The first MCD tested was the R7600U-20. Its 10 dynodes generated pulses of several volts. It was replaced by the R11187, a custom version of the R7600U-20 with only 8 dynodes. The R14755U-100 was tested, being the narrower MCD PMT: its diameter very close to the Tungsten/GAGG cell size makes it a promising candidate for the Tungsten region.

8.4 Data Analysis

8.4.1 Tracking

The DWCs provide tracking information with a resolution of 200 μm. The positions of the DWC planes and their distance from the prototypes is measured before data taking. The DWCs are instrumental to identify the hit position on the prototype and to clean the dataset from early-showering particles. If 3 hits in the DWCs are recorded for an event, a line per coordinate is fitted through them. If the fit χ^2 exceeds 3 in x or y, or a DWC did not output, the event is discarded. The large cut on the χ^2 is necessary due to mechanical misalignment of the DWCs.

8.4.2 Constant Fraction Discrimination

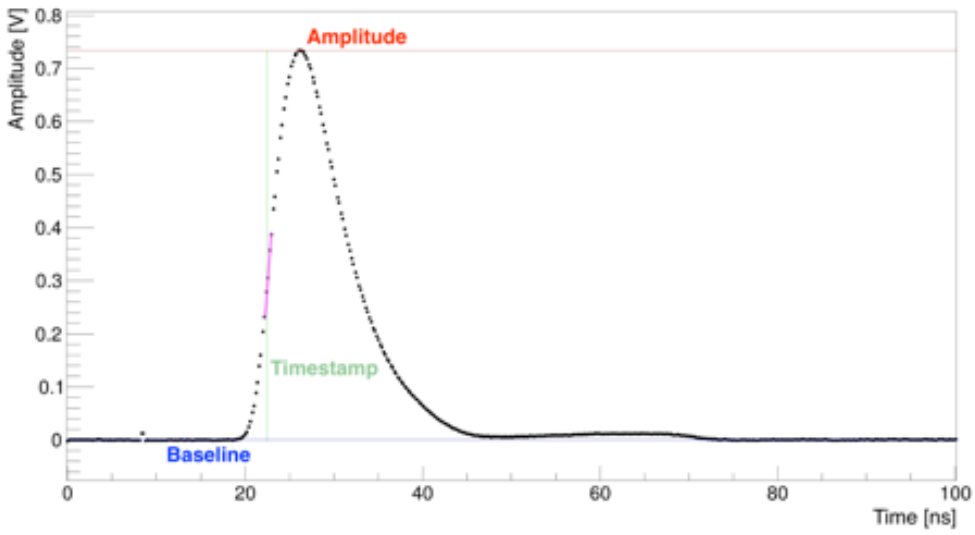

FIGURE 8.5: Example of a waveform illustrating the time pick-off algorithm. It was taken with the Tungsten Polystyrene prototype read out by a R14755U-100 MCD-PMT. Highlighted are the baseline (blue), amplitude (red), the linear approximation of the leading edge (magenta) and the timestamp at 30% of the amplitude (green).

The default technique employed for time pick-off was an offline constant fraction discrimination (CFD). CFD compensates the time walk induced in the timestamp by amplitude fluctuations. [103]

An example pulse is shown in Fig. 8.5. Negative pulses were inverted for simplicity. The baseline was computed as the average of the first 50 to 100 samples, depending on the pulse position within the digitisation window. The sample with the highest voltage determined the pulse amplitude. The crossing time of the threshold was computed interpolating between the sample above and the one below. Employing 2 samples reduces the noise contribution[1] by $\sqrt{\frac{2}{3}}$ [42].

8.4.3 Timestamps combination

If the shower develops over an area read out by more than a PMT, combining the timestamps of each PMT can improve the time resolution.

The technique to combine 2 timestamps used by default is a weighted average with inverse-variance weighting:

$$t_{comb} = \frac{w_1 t_1 + w_2 t_2}{w_1 + w_2} = \frac{\frac{t_1}{\sigma_1^2} + \frac{t_2}{\sigma_2^2}}{\frac{1}{\sigma_1^2} + \frac{1}{\sigma_2^2}}, \tag{8.1}$$

being σ_i the time resolution of the i-th cell alone. The inverse-variance weighting has the least variance amongst the weightings for independent observations. If the two timestamps are (anti)correlated – as in the case of unsegmented prototypes read out from both ends – the Gauss-Markov theorem gives the weighting:

$$\begin{cases} w_1 = \frac{\sigma_2^2 - \sigma_{1,2}}{\sigma_1^2 + \sigma_2^2 - 2\cdot\sigma_{1,2}}, \\ w_2 = \frac{\sigma_1^2 - \sigma_{1,2}}{\sigma_1^2 + \sigma_2^2 - 2\cdot\sigma_{1,2}}, \end{cases} \tag{8.2}$$

where $\sigma_{1,2}$ is the covariance between the set of timestamps t_1 and t_2.

8.4.4 Energy Calibration

Longitudinally-segmented calorimeters pose additional challenges for calibration, as discussed in Sec. 2.3.

Calibrating both front and back sections simultaneously with only electromagnetic showers would increase the response non-linearity. A solution would be to intercalibrate the longitudinal section with MIPs, e.g. muons [8]. However, no MIP beam was available

[1] This improvement is obtained if the noise is uncorrelated between the 2 samples, whereas there is no improvement for fully correlated noise (e.g. white noise oversampled).

in DESY, while at SPS the dynamic range of the electronics was not wide enough to detect MIP signals *and* electrons from 20 to (more than) 100 GeV.

The choice taken was to calibrate the two sections independently. First, the front PMTs' bias voltages were tuned to achieve the same peak position of the charge histograms of each cell with the electron beam hitting the centre of that cell. Afterwards, the front section was removed and the same procedure was repeated for the back section. Then, selecting only events hitting in a 20×20 mm^2 square in the centre of the back section, a set of 9 calibration coefficients c_j for the back cells was found by minimising the residuals [104]:

$$\sum_{i_{ev}=1}^{N_{ev}} \left[E_{beam} - \sum_{j=1}^{9} c_{b,j} S_{b,j} \right]^2 = \min, \tag{8.3}$$

where $S_{b,j}$ and $c_{b,j}$ are the integrated charge and the calibration coefficient of the j-th cell in the back section, E_{beam} equals 3 GeV and i_{ev} the i-th event of the dataset. Afterwards, the front section was reinstalled, and the procedure was repeated for the whole module keeping the calibration coefficients of the back constant:

$$\sum_{i_{ev}=1}^{N_{ev}} \left[E_{beam} - \sum_{j=1}^{9} \left(c_{f,j} S_{f,j} + c_{b,j} S_{b,j} \right) \right]^2 = \min, \tag{8.4}$$

where $S_{f,j}$ and $c_{f,j}$ are the integrated charge and the calibration coefficient of the j-th cell in the front section.

The procedure was tested in Monte-Carlo simulations for the Tungsten/GAGG prototype over the 1-5 GeV range (see Sec. 9), without observing any statistically-significant increase of the non-linearity.

Chapter 9

Tungsten Garnet SPACAL

9.1 The Prototype

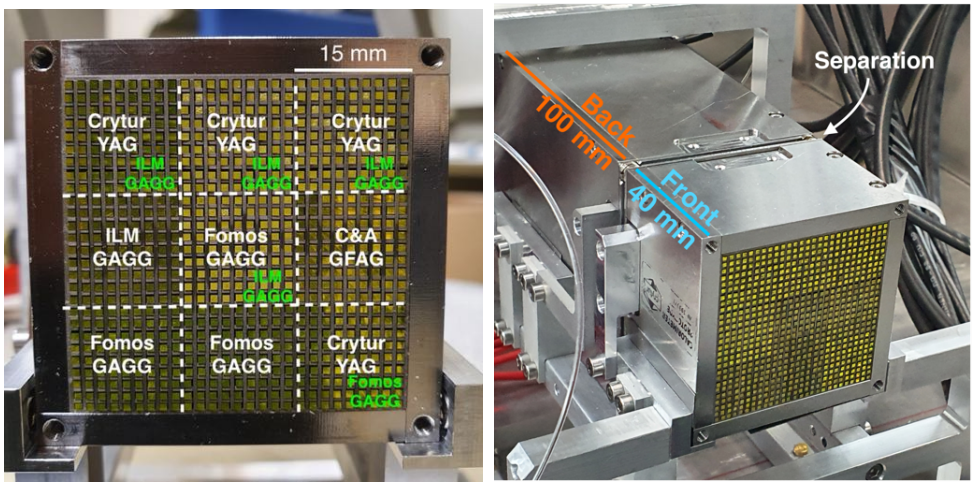

(A) Front view (B) Three-quarter view

FIGURE 9.1: Pictures of the Tungsten-Crystal SPACAL prototype without readout. On the left, the 9 cells with different garnets and producers are highlighted. This configuration was employed for the energy resolution measurements. The layout was modified in 2021 and the new materials are labelled in green. On the right, the front and the back sections are visible, with the small gap between the two and the mechanics holding the prototype.

The SPACAL with a Tungsten absorber and garnet crystal fibres is shown in Fig. 9.1. It was the first assembled and tested in the frame of the LHCb ECAL Upgrade II. Many

studies, such as the dependence of the energy resolution on the beam incidence angle (Sec. 9.2), served as basis for all the following prototypes.

The scintillating fibres are Cerium-doped garnet crystals, namely $Gd_3Al_2Ga_3O_{12}$ (GAGG) and $Y_3Al_5O_{12}$ (YAG). The materials are discussed in detail in Part II. Each section of the prototype was equipped with 1 cell of GAGG from Institut Lumière Matière (ILM, France), 3 of GAGG from Fomos (Russia), 1 of Gadolinium Fine Aluminum Gallate (GFAG), a commercial name for the fast-timing GAGG by C&A (Japan), and the remaining 4 with YAG fibres from Crytur spol. s.r.o. (Czech Republic). The fibres were arranged in the cells as shown in Fig. 9.1, with the same crystal type in the front and in the back sections. This layout was employed for the energy resolution measurements. Later in 2021 a few cells were replaced (see green labels in Fig. 9.1), removing YAG altogether.

The absorber, produced by Crytur[1], is made of pure Tungsten plates 0.5 mm thick and 19 g/cm^3 dense. Rows of 0.5 mm were carved with an interfibre distance of 1.7 mm in the planes for half of their length, resembling a comb. Half of the planes could be inserted into the other half rotated by 90°, thus forming a grid of rows with 0.5 mm thick tungsten walls and squared holes of 1.2 mm side, wherein the fibres could be inserted. Therefore, the interfibre distance between adjacent fibres is 1.7 mm.

The prototype is longitudinally segmented into a front and a back section close to the average shower maximum. The cell size is loosely matching the Molière radius.

The front and the back sections are 40 mm and 100 mm long, respectively. With a radiation length X_0 of 6 mm, the first section accounts for about 7 X_0, corresponding to the position of the average shower maximum for 20 GeV electrons. The front section was read out from the front, the back one from the back. On the side opposite to the readout, a thin 3M Enhanced Specular Reflector (ESR) film layer was pressed against the fibres by a stainless steel plate to reflect the light towards the readout. These plates were 1.50 mm and 1.05 mm thick for the front and the back sections, respectively. The sections were made independent to allow inserting a large area picosecond photodetector (LAPPD) as an optional timing layer, discussed in [105].

Each section is divided into 9 cells of 15×15 mm^2 surface. The Molière radius is 14.3 mm and 15.2 mm for the GAGG and YAG cells, respectively, computed as the volume-weighted average of the materials' radii. The shower containment predicted by Monte Carlo simulations (see Part IV) for electrons hitting the central cell is above 90%.

[1] In 2022 Crytur patented the idea of comb-like W planes to produce a SPACAL (Application EP-4071518-A1). Bear it in mind.

9.2 Energy Measurements

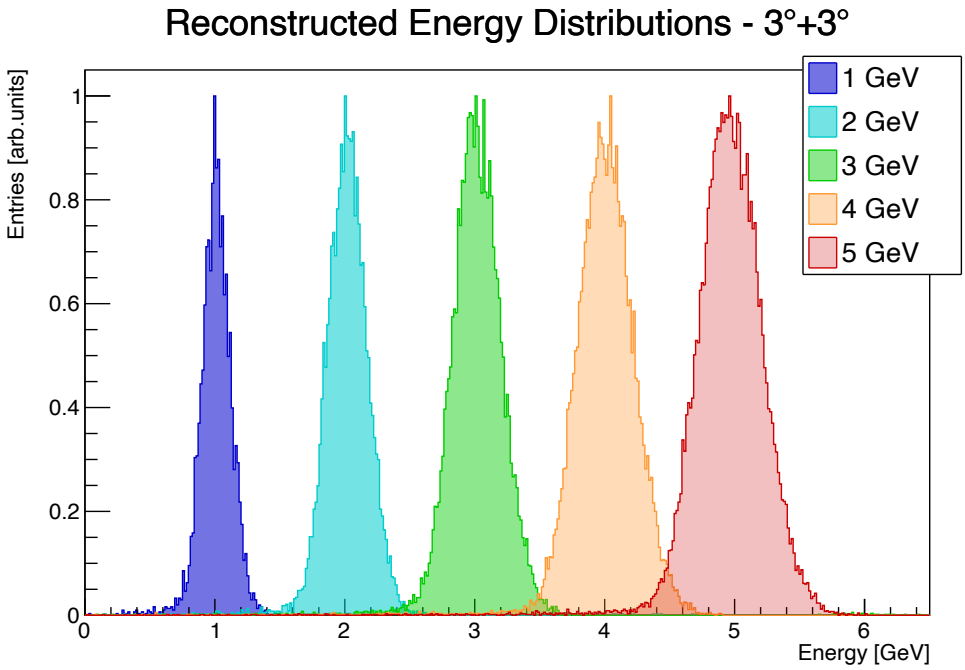

FIGURE 9.2: Distributions of the reconstructed energy at 3°+3° incidence angle rescaled to the same height. From reference [96].

The energy resolution was measured by coupling all the 18 cells to the R12421 PMTs via 30 mm long PMMA light guides in dry contact, i.e. without optical grease or glue.

The measurements were carried out with electrons of 1 to 5 GeV hitting the centre of the prototype in a 5×5 mm^2 square. Between 5000 and 25000 events were used for each energy and angle. The reconstructed energy was computed summing the integrated charge of the 18 cells weighted by the calibration coefficients. The calibration (see Sec. 8.4.4) was performed with electrons of 3 GeV. The distributions of reconstructed energy at 3°+3° incidence angle are visible in Fig. 9.2. These were fitted with a Gaussian function whose standard deviation divided by its mean is the energy resolution. The Gaussian fit describes well the energy distributions for incidence angles greater than 1°+1°. The non-linearity over the range tested was within $\pm1\%$.

The measured resolutions (see Fig. 9.3) against the beam energy were fitted with Eq. 2.16 employing one sampling and one constant term per incidence angle, and one common

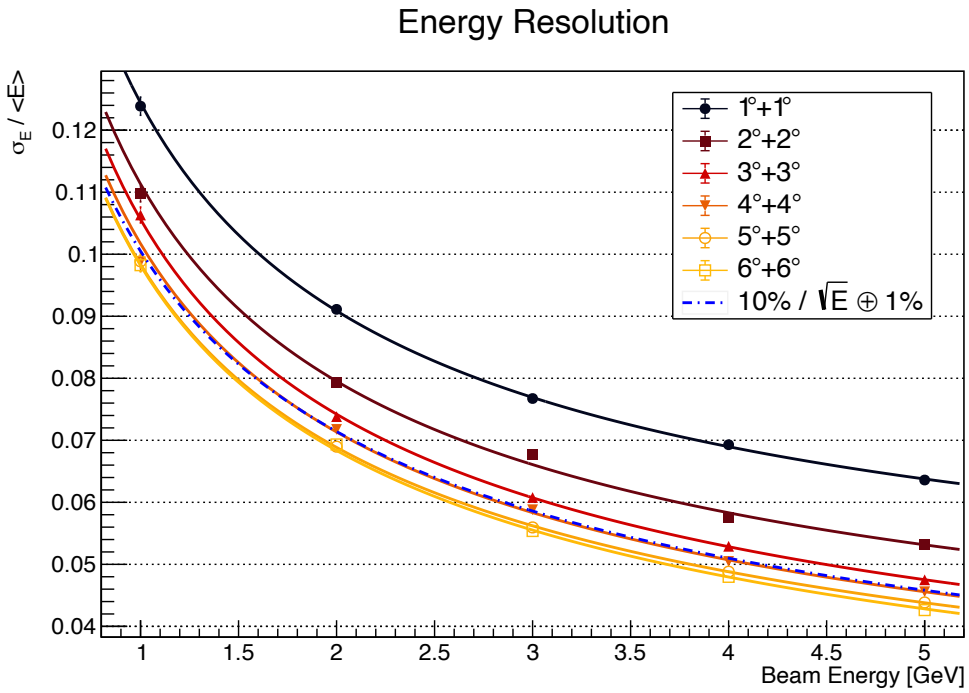

FIGURE 9.3: Energy resolution of the prototype measured at different incidence angles of the electron beam. The lines are fits of Eq. 2.16 to the datapoints. The common noise term is (0.024 ± 0.004) GeV. The resolution improves with increasing incidence angle. This effect fades above 3°+3°. The blue dotted line is the resolution reached with 10% sampling and 1% constant terms. From reference [96].

noise term for the six angles, which was (0.024 ± 0.004) GeV.

The energy resolution improves increasing the incidence angle, with the effect fading above 3°+3°. At 3°+3° and 6°+6° the sampling terms are (10.2 ± 0.1)% and (9.5 ± 0.1)%, respectively. The shower is transversally narrower than the interfibre distance at the beginning of its development, giving rise to large differences in energy deposit and longitudinal fluctuations in its start position depending on whether the primary electron first hits the absorber or a fibre, as already observed in [106]. Tilting the prototype offers a higher sampling rate along the direction of the primary electron, thus reducing the above fluctuations and improving energy resolution.

The constant term and its statistical error at 3°+3° are found to be (1.2 ± 0.3)%. Several

potential sources of systematic uncertainty were investigated. First, the impact on the constant and sampling terms of a misalignment up to 0.15° (see Sec. 8.2) is smaller than the statistical uncertainty. Secondly, the momentum spread of the beam is unknown (see Sec. 8.1.1); for illustration, an uncertainty of 50 MeV on the beam energies added to the fit doubles the statistical uncertainties on the constant terms. As a third test, the constant terms at 3°+3° and larger incidences were assumed to be up to 2% and a fit to extract the sampling and noise terms was performed; compared to the nominal procedure, the sampling terms decreased maximally by 1%. Finally, a variation on the calibration method was tested applying a weight to the back section's calibration factors to minimise the non-linearity over the energy range instead of the resolution; the constant term at 3°+3° increases to (1.9 ± 0.2)% and similar values are found at larger angles, whereas the sampling terms are unaffected within the statistical uncertainty.

In conclusion, whilst the sampling terms can be reliably determined in the energy range available, a precise measurement of the constant terms and their systematic uncertainties requires data at higher energies.

9.3 Time Resolution

Sec 9.3.1 discusses the timing results obtained in DESY until 2021. The focus is on achieving uncompromised timing performance, in particular exploring the optical coupling contribution. The results were published in [96].

Sec. 9.3.2 shows the latest timing results. The testbeam campaign in 2022 was dedicated to moving towards a realistic solution for the upgrade, which included photomultipliers closer to or matching the cell size and employing light guides.

9.3.1 Time Resolution at DESY with R7600U-20

The time measurements were carried out instrumenting 1 front and 1 back cell with R7600U-20 PMTs. Approximately 2000 events were used per data point. The optimal CFD threshold was found with a scan to be 15%. All the measurements were performed with a beam incidence angle of 3°+3° and selecting tracks hitting the centre of the front cell in a 4×4 mm^2 square. The difference between a cell timestamp and the time reference was computed and the distributions of this difference for each beam energy were then fitted with a Gaussian function whose standard deviation, after subtracting quadratically the reference's contribution, is the time resolution. The sources of systematic errors for the energy measurements discussed in Sec. 9.2 were found negligible with respect to the statistical uncertainties for the timing measurements.

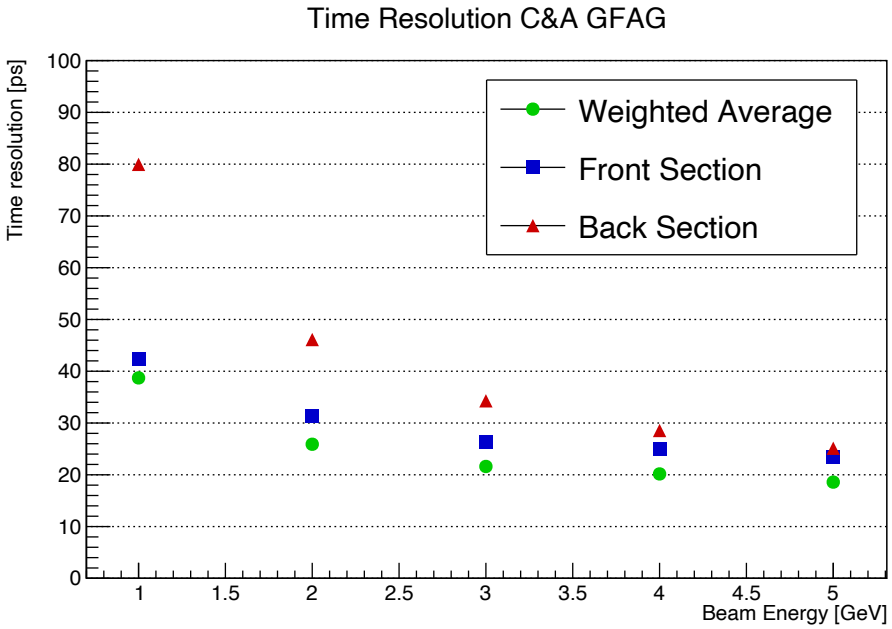

FIGURE 9.4: Time resolution of the GFAG cells with Hamamatsu MCD R7600U-20 PMTs in direct dry contact. The three set of resolutions are obtained using the front cell, the back one, and the inverse-variance weighted average of the two timestamps. From reference [96].

Fig. 9.4 shows the time resolution of the GFAG cells. The front one provides better time resolution than the back one, with the spread between the two diminishing with increasing energy. This is expected for electrons of a few GeV which produce a relatively short shower and deposit on average the larger fraction of their energy in the front cell. The time resolution reaches down to (18.5 $\pm$ 0.2) ps at 5 GeV combining the front and the back cells.

In agreement with the laboratory tests (see Part II), the fibres from ILM and C&A show a similar resolution, whereas those from Fomos are a few ps worse (see later Fig. 9.6 and Sec. 9.3.1). No degradation of time resolution within the experimental uncertainty is visible when using 12.8 m instead of 3.8 m of total cable length to connect the PMTs to the digitiser.

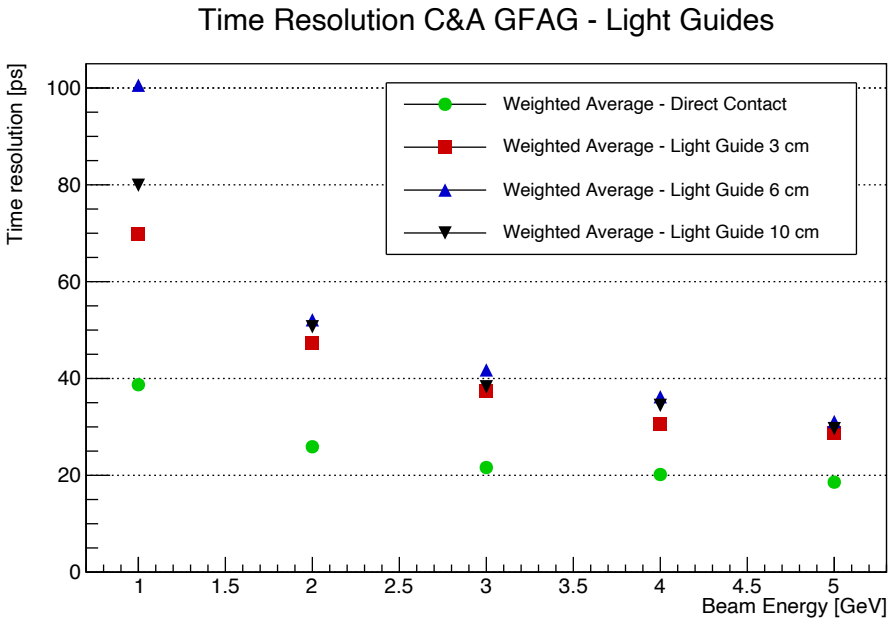

FIGURE 9.5: Time resolution of C&A GFAG combining the front and the back cells in direct dry contact with the MCD PMTs or using PMMA light guides. Employing a light guide worsens time resolution, but the deterioration depends little on the length. From reference [96].

Time resolution and Optical Coupling

Achieving fast timing with light-based detectors requires maximising the amount of optical photons detected in the first nanoseconds of the scintillation process, i.e. the photon time-density [67, 66].

The time resolution of the GFAG cells was compared placing the PMT in direct dry contact with the fibres or via a PMMA light guide of length 30, 60, or 100 mm (Fig. 9.5). With the light guides, the resolution is degraded by a factor 1.5 to 2 in the energy range considered, being close to 30 ps at 5 GeV. The light guides length has little influence on the resolution or on the pulse amplitude, therefore light absorption inside the light guides cannot account for the loss of performance. The discrepancy at 1 GeV between the dataset with 60 and 100 mm light guides could be explained by the lack of electronic attenuation.

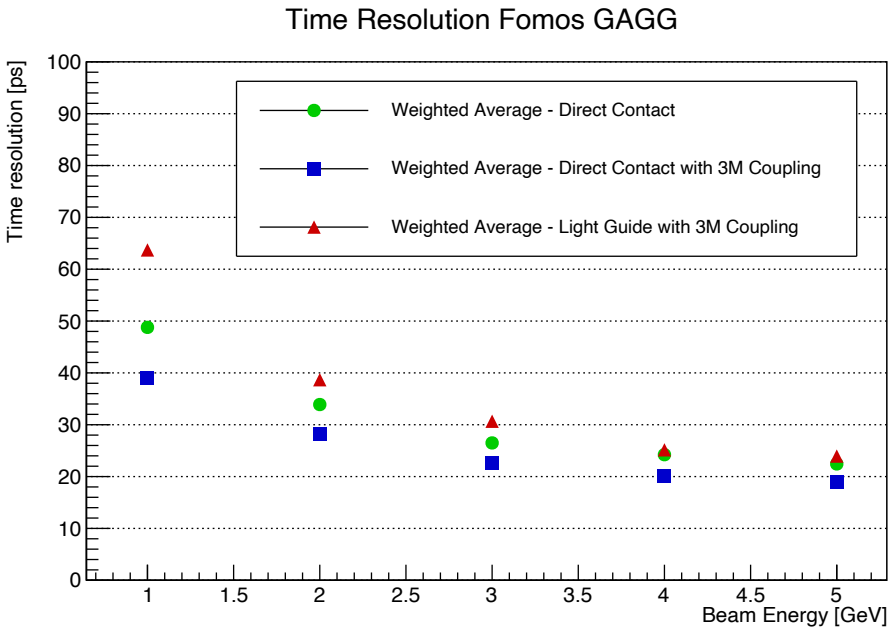

FIGURE 9.6: Time resolution of Fomos GAGG combining the front and the back cells coupled to the PMTs using a 3M optical adhesive with an index of refraction of 1.47. From reference [96].

Another source of light loss is given by the Fresnel reflections taking place at each optical interface between media with mismatching indices of refraction. The entrance and exit face of a light guide constitute such an interface with the surrounding air. Gluing the light guide to the photocathode and the crystal fibres with some high-refractive-index optical coupling removes air from the optical chain, thus reducing Fresnel reflections. Moreover, the high index of refraction of GAGG crystals (almost 1.90 at the peak emission wavelength [107]) produces a light extraction cone of approximately 32° when surrounded by air; raising the index of refraction at the crystal end face replacing air with an optical grease widens the extraction cone and, thus, increases the light output.

The time resolution of a Fomos GAGG cell was measured in direct contact and with 30 mm long light guides using 3M optical adhesives (index of refraction 1.47) between fibres, light guides, and the PMTs (Fig. 9.6). In this way, the timing deterioration moving from direct dry contact to using a light guide is almost entirely mitigated. In addition to that, gluing the PMT photocathode directly to the crystal fibres improves further the time resolution, reaching better than 20 ps at 5 GeV.

9.3.2 Time Resolution in SPS 2022

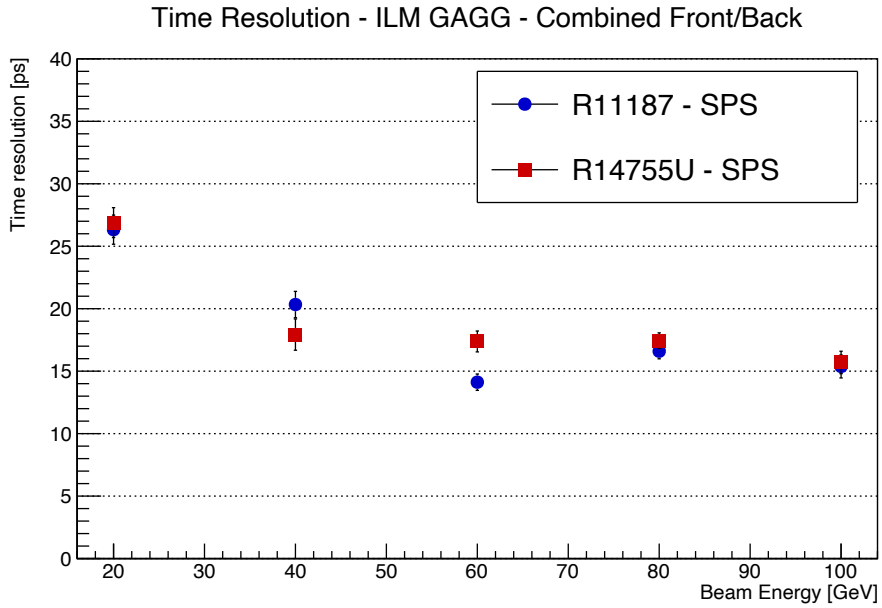

FIGURE 9.7: Time resolution of the ILM GAGG cell at SPS combining front and back sections, with R11187 and R14755U PMTs.

In 2022 the time resolution was studied with optical light guides and other PMTs. The PMTs were the R11187 and the R14755U-100, coupled to the cells via the same light guides of Sec. 9.2. The R1187 PMTs were biased a 500/450 V (front/back) at SPS, while the R14755U at 600 V.

Fig. 9.7 shows the resolution to electrons with an incidence angle of 3°+3°. The cell is the central one containing ILM GAGG and the timestamps front and back are combined with a weighted average. Both PMTs perform similarly reaching 15 ps at high energy. The degradation in performance with respect to the best values of Sec 9.3.1 is given by the additional Fresnel reflections introduced by the light guides and .

Chapter 10

Tungsten Polystyrene SPACAL

10.1 The Prototypes

(A) Single cell 3D printed prototype (B) 45x45 mm^2 3D printed prototype

FIGURE 10.1: Pictures of the Tungsten-Polystyrene SPACAL prototypes. On the left, the first 3D printed absorber, 15x15 mm^2. On the right, the 45x45 mm^2 3D printed absorber.

Two SPACAL prototypes were assembled of pure Tungsten absorber and polystyrene scintillating fibres (Fig. 10.1). The Molière radius is 18 mm, computed as the volume-weighted average of the materials' radii, thus the target cell size was 20x20 mm^2.

The scintillating fibres are Kuraray SCSF-78, squared with cross section 1x1 mm^2, non-S type to reduce the light attenuation. The core is made of polystyrene and there is a

single cladding layer of PMMA. The emission peak is at 450 nm and the decay time 2.8 ns. [91]

Both absorbers are 3D printed pure Tungsten, targeting the same geometry of Chap. 9. The squared holes size is 1.2 mm and the wall thickness 0.5 mm, thence a interfibre distance of 1.7 mm. The roughness of the external surfaces was measured at the CERN metrology laboratory, finding an average roughness (R_a) of 5 μm and a peak-to-peak maximum distance (R_t) of 51 μm, sufficiently low to accomodate 1x1 mm^2 fibres in the 1.2x1.2 mm^2 holes. The first prototype was made of 1 block of 15x15x40 mm^3 (front section) and 2 blocks of 15x15x50 mm^3 (back section).

The second and larger absorber was produced after the successful testing of the first one. It was made of 3 blocks of 45x45x50 mm^3 and 1 of 45x45x40 mm^3 for a total length of 190 mm. The blocks were enclosed in a 3D printed plastic frame to keep them in place. This prototype was not segmented longitudinally: the plastic fibres were inserted for the whole length of the absorber and left sticking out from both side by a couple of cm. They were glued to a plastic frame and the whole assembly was diamond milled to polish the fibres end and reduce the excess length. The prototype was large enough to equip 2x2 cells of 20x20 mm^2. The remaining holes on the sides were not read out and masked. No energy resolution measurements were performed since the cells were not enough to produce a 3x3 cluster. A new prototype is being produced in 2023 which will serve this purpose.

10.2 Single-cell Prototype

The time resolution of the single-cell prototype was measured at DESY in 2 configurations (Fig. 10.2): with continuous fibres 140 mm long, a mirror in front and readout at the back ("Continuous" configuration); longitudinally segmented with 40 mm long (front) and 100 mm long (back) fibres, mirrors between the 2 sections and readout at the front and at the back ("Split" configuration). The R7600U-20 MCD was placed in direct dry contact with the prototype, i.e. without light guides or optical grease. The electron beam was aimed at the centre of the prototype and events within a 3x3 mm^2 square were selected.

In the split configuration, the front section performs better than the back one at lower energies because the shower is short and most of the deposition takes place in the front section. The two section cross between 3 and 4 GeV. Combining the two sections pushes the resolution below 20 ps at 5 GeV.

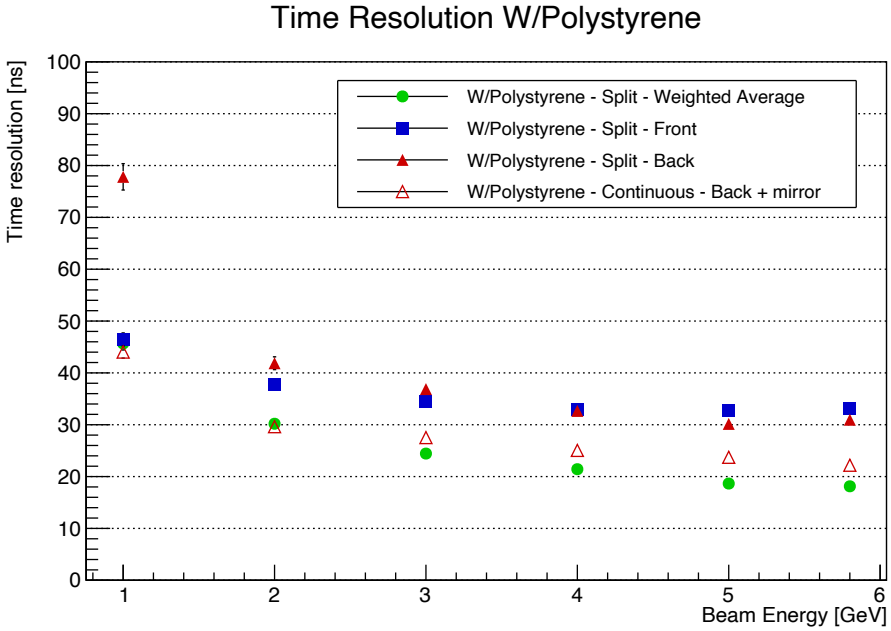

FIGURE 10.2: Time resolution of the first 3D printed Tungsten/Polystyrene prototype. Comparison between the configuration longitudinally segmented into 2 sections 40 and 100 mm long, and the one with continuous fibres read out at the back and mirror in front.

In continuous configuration, time resolution is in line with the Split one. Above 3 GeV the resolution is only a few ps worse. The mirror in front allows collecting with the back PMT most of the light which would be read out at the front.

The successful results prompted the construction of the larger prototype, whose performance is discussed in the next section.

10.3 Large Prototype

Time resolution was measured with R11187 PMTs and R14755U PMTs both with one PMT at the back and a mirror in front (single side readout), and with PMTs in front and in the back (double side readout). Fig. 10.3 illustrates the difference between the two configurations.

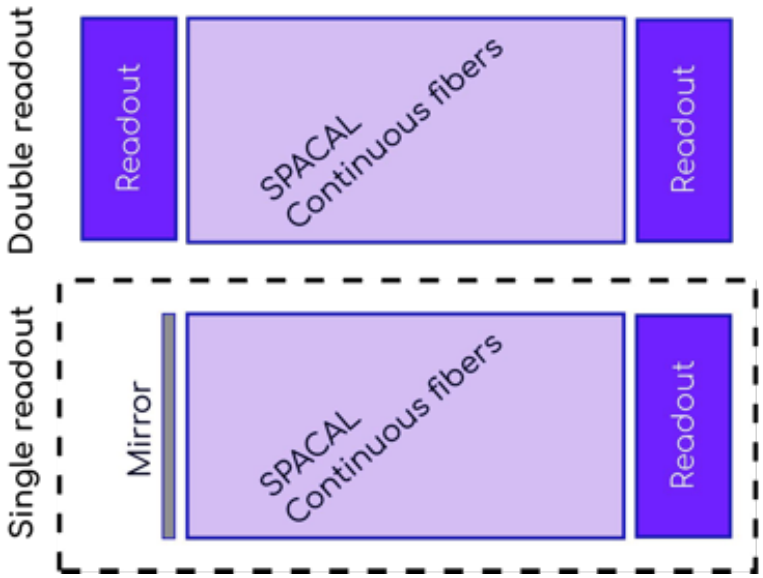

FIGURE 10.3: Illustrative drawing of the single side and double side readout configurations. Front is on the left, back on the right. Courtesy of M. Salomoni.

Unlike the case of longitudinally-segmented prototypes, with continuous fibres the front section's resolution is limited at about 100 ps, significantly worse than the back. No improvement comes from the inverse variance weighted average of Eq. 8.1. This is explained by the fact that the front and back timestamp show a strong correlation, making necessary using the covariance weighting described in Eq. 8.2. This technique has been used to combine front and back throughout the rest of the chapter.

Time resolution with R11187 PMTs is shown in Fig. 10.4. The PMTs were dry coupled via a 20x20 mm^2 fishtail light guide. The bias voltage was 600-620 V at DESY and 410 V at SPS. The resolution in single and double side readout at SPS was measured in two different testbeam two weeks apart. In particular, for the latter configuration there were available electron beams up to 150 GeV. Both configurations achieve resolutions below 20 ps above 20 GeV, and down to about 10 ps. Single side readout performs systematically slightly better than double side readout[1].

[1]Note: these results cannot be compared to Fig. 10.2. The large prototype has continuous fibres, 20x20 mm^2 cells, different PMTs, and it is longer.

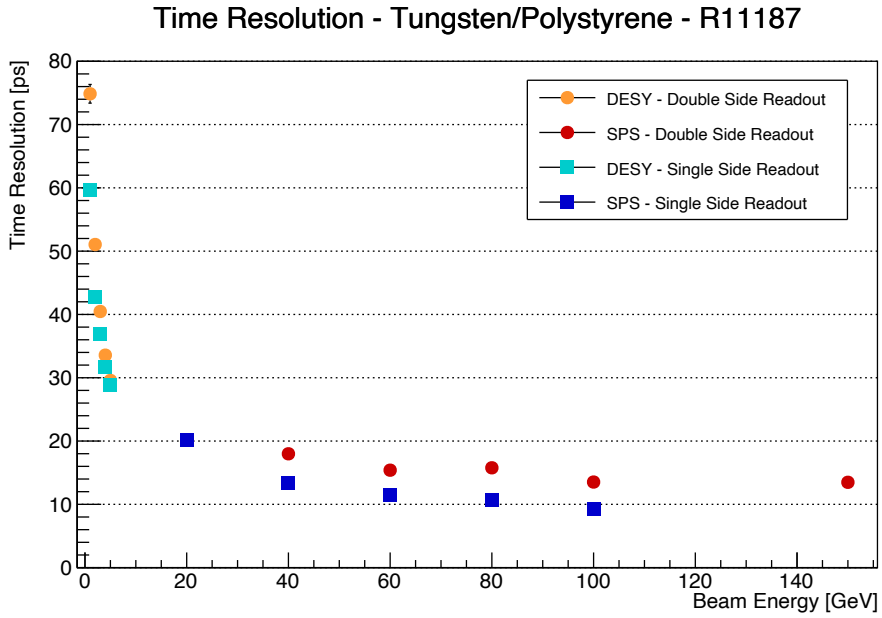

FIGURE 10.4: Time resolution of the large Tungsten/Polystyrene prototype combining front and back as in Eq. 8.2 at DESY and SPS with R11187 PMTs and 3°+3° incidence angle.

Time resolution with R14755U PMTs is shown in Fig. 10.5. The PMTs were dry coupled via a 15x15 mm^2 fishtail light guide[2]. The bias voltage was 600 V at SPS. The small gain of this PMT did not provide a sufficient S/N ratio below 5 GeV, hence resolution was not measured at DESY. Unlike R11187, single side readout is limited above 20 ps, whereas in double side readout the resolution is about 10 ps above 40 GeV.

10.3.1 Optimum CFD Threshold

The optimal CFD threshold for the time resolution was determined with a scan for each PMT (Fig. 10.6).

In single side readout, the optimum threshold for R11187 was between 40% and 45%. Conversely the optimum for the R14755U PMT ranged from 65% at 20 GeV to 80% at

[2]Unfortunately there was no 20x20 mm^2 light guide available with a diameter matching the PMT's photocathode.

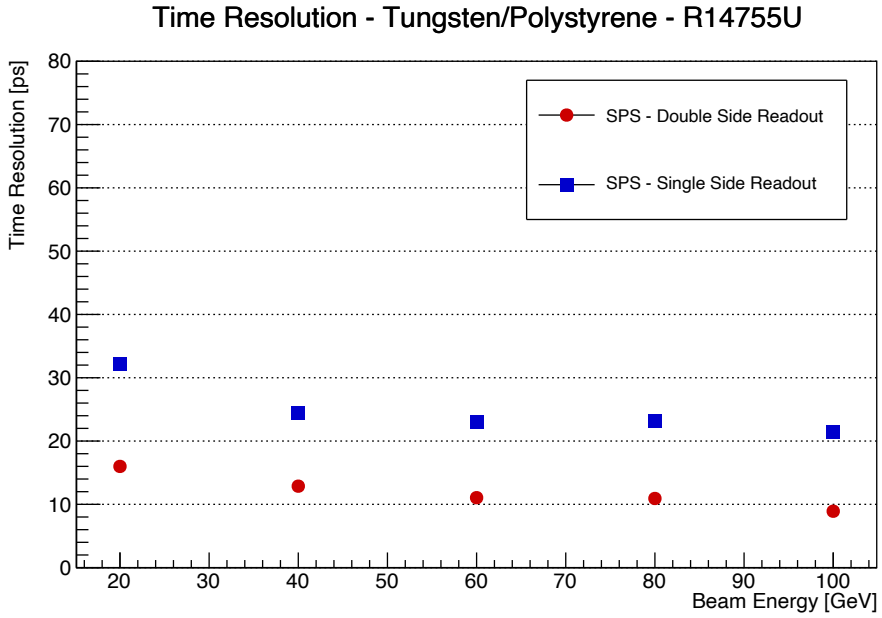

FIGURE 10.5: Time resolution of the large Tungsten/Polystyrene prototype combining front and back as in Eq. 8.2 at SPS with R14755U PMTs and 3°+3° incidence angle.

100 GeV. In both cases the optimum was not at the maximum slew rate, showing that the electronic noise contribution was of second order in the testbeam configuration.

The higher optimum threshold for the R14755U PMT could be related to its single photoelectron pulse, being as narrow as 680 ps, compared to 3 ns of R11187[3]: the narrow single photoelectron pulse could resolve features in the distribution of the photons time of arrival on the PMT, e.g. direct and reflected waves, shifting the ideal threshold with respect to a PMT with wider single photoelectron pulses. Alternatively, saturation of the PMT could reduce the pulse amplitude, thus increasing the optimum threshold. Further studies are planned, including Monte Carlo Simulations.

TABLE 10.1: Rise time 10-90% of the Tungsten/Polystyrene prototype with R11187 and R14755U PMTs in single side readout.

PMT	Rise Time 10-90% [ns]
R11187	3.6
R14755U	1.8

10.3.2 Average Pulse Shape

The effect of the narrower single photoelectron pulse is visible in the average pulse shape (Fig. 10.7, (A)), measured in the same configuration barring the different light guides. They were computed using 2000 pulses. The time alignment was obtained computing the timestamp at the threshold with optimum time resolution and subtracting it. The average pulses were rescaled to 1 and aligned at the crossing time of 0.01.

The R11187 pulse takes 3.6 ns to rise from 10% to 90%, whereas the R14755U only 1.8 ns. A short rise time reduces the effect of the noise jitter which could significantly deteriorate time resolution for low-amplitude pulses. Moreover, the R14755U pulse is well contained within 25 ns, avoiding signal spillover into the next bunch at 40 MHz rate.

Another difference was observed between single side and double side readout (Fig. 10.7, (B)). The narrowest pulse is the back one in double side readout. The front PMT has a wider pulse due to the additional time spread of the light transport inside the fibres. The pulse of the back PMT in single side readout is the widest, since it mixes both light emitted towards the back and towards the front but reflected back by the mirror.

[3]Precise information on the single photoelectron pulse width is not available for the R11187. However, the R11187 is derived from the R7600U-20. According to the datasheet, the R7600U-20 has a single photoelectron pulse width FWHM of 3.2 ns. For both the R11187 and the R7600U-20 the rise time is 1.6 ns. It is reasonable to assume that the single photoelectron pulse does not differ significantly.

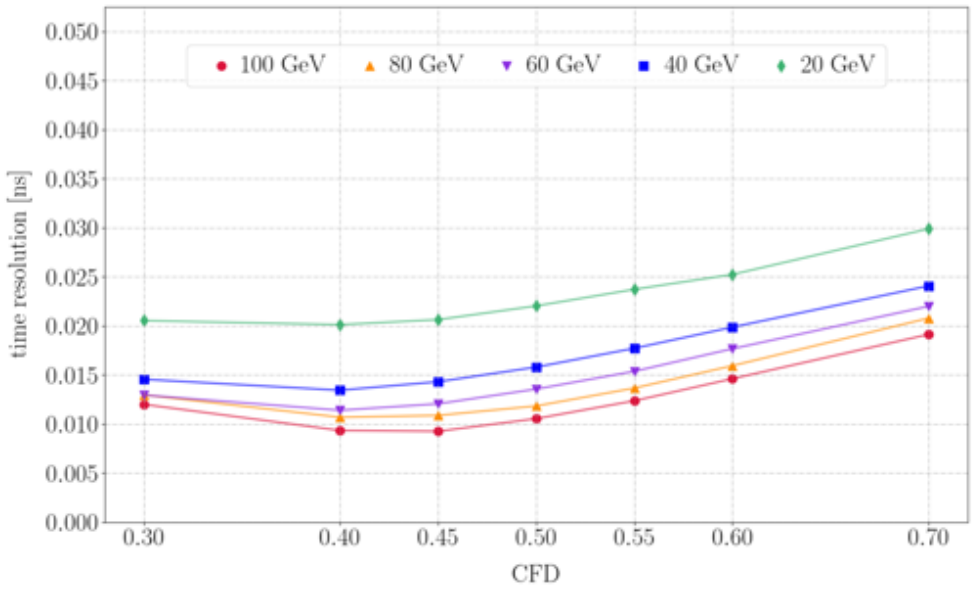

(A) R11187.

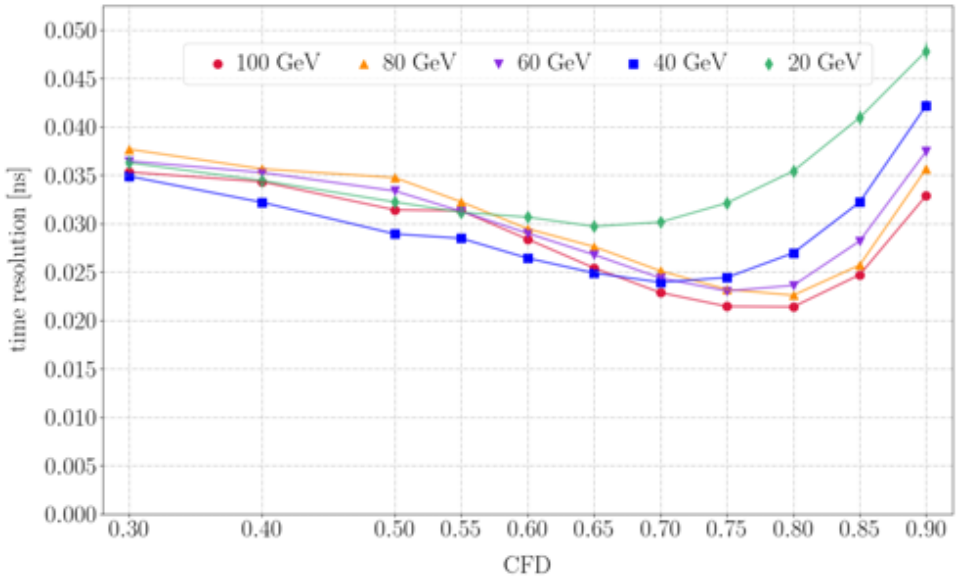

(B) R14755U.

FIGURE 10.6: CFD threshold scan in single side readout for R11187 (A) and the R14755U PMT (B).

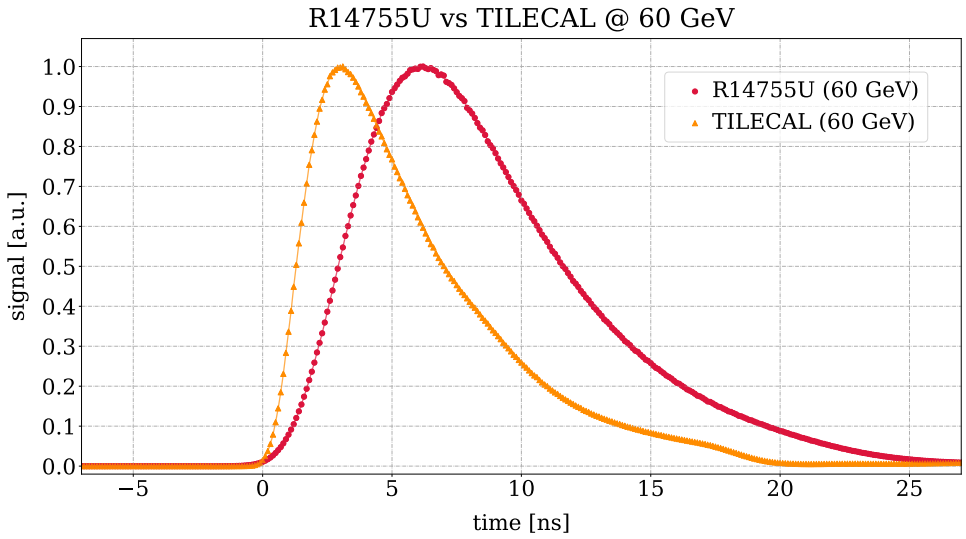

(A) R14755U vs R11187 PMTs.

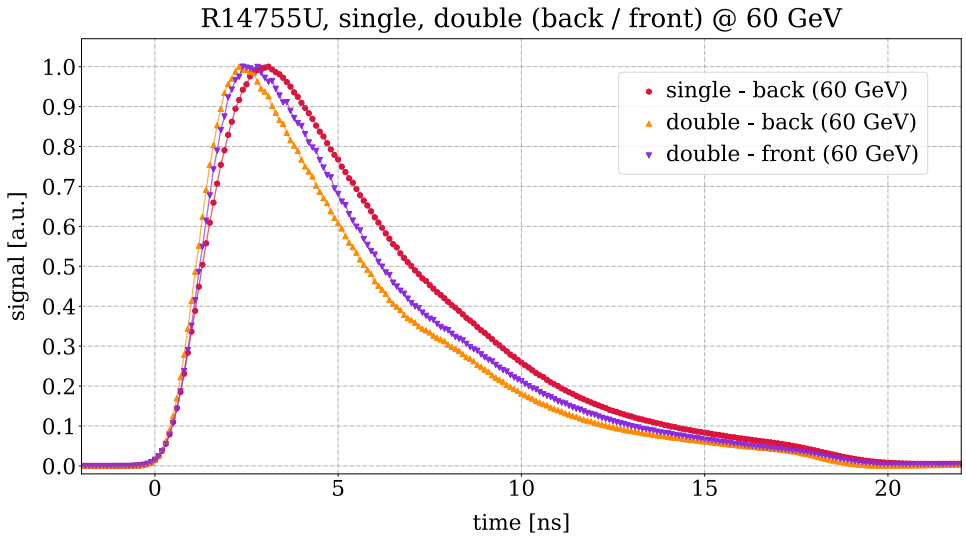

(B) Single vs double side readout.

FIGURE 10.7: Average waveforms of the Tungsten/Polystyrene prototype rescaled to 1 for different configurations. (A) comparison between R14755U and R11187 in single side readout for 60 GeV electrons. (B) comparison between single side readout and the front and back sections in double side readout for 60 GeV electrons.

Chapter 11

Lead Polystyrene SPACAL

11.1 The Prototype

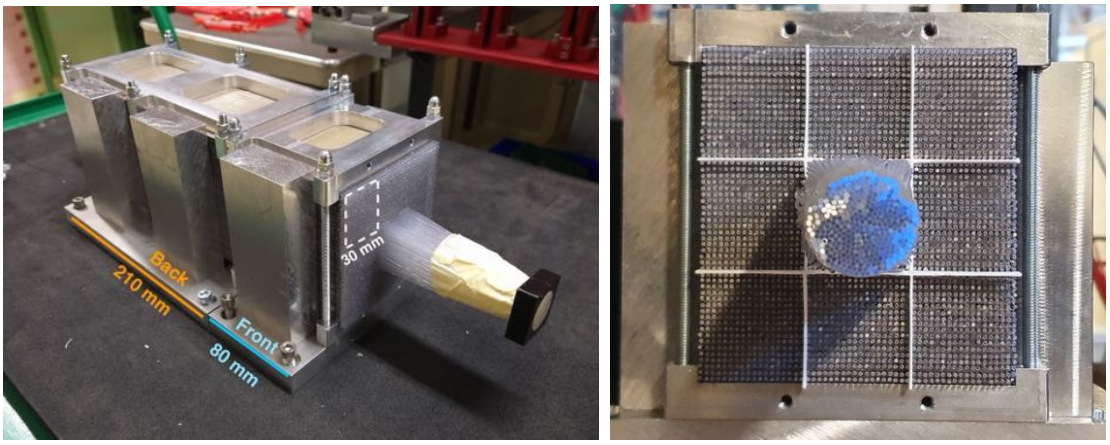

(A) Three-quarter view (B) Front view

FIGURE 11.2: Picture of the Lead/Polystyrene prototype inside the aluminium jig. The central cell is visible with the 100 mm extra length of fibres bundled together.

The prototype was made of Lead absorber and polystyrene scintillating fibres (Fig. 11.2). The Molière radius is 25 mm, computed as the volume-weighted average of the materials' radii. The prototype was divided into cells of 30 mm.

The scintillating fibres are Kuraray SCSF-78[1], round with a diameter of 1 mm, double-cladded and with a polystyrene core. The fibres are non-S type to reduce the attenuation. The emission peak is at 450 nm and the decay time 2.8 ns. [91]

The absorber was made of stacked Lead plates. The plates were rolled to produce half-circular grooves of diameter 1.2 mm on both surfaces. The wall thickness between two horizontal grooves was 0.5 mm, thus making for a interfibre distance of 1.7 mm. The width groomed was 90 mm, with a few mm extra ungroomed. The plates were covered in plastic to allow handling without direct exposure to Lead. An aluminium jig held the stack in place. It was made of a base and a top plate pressed against each other by long screws and a lateral frame.

The assembled prototype accounted for 3x3 cells, each of 30x30 mm^2. It was longitudinally segmented into a front section of 80 mm (7 X_0)and a back section of 210 mm (18 X_0). Both sections were terminated with an ESR mirror foil at the junction. The scintillating fibres were sticking out a few mm to allow cutting and polishing them to the same length. In both sections, the central cell had the fibres sticking out by 100 mm and bundled together.

11.2 Energy resolution

The energy resolution was measured by coupling all 18 cells to Hamamatsu R7899-20 PMTs in direct dry contact with the 2 central bundles, and via 100 mm long PMMA fish-tail light guides for the others. The calibration procedure (see Sec. 8.4.4) was performed with 40 GeV electrons.

The measurements were carried out with electrons of 20 to 80 GeV hitting the centre of the prototype in a 5x5 mm^2 square with an incidence angle of 3°+3°. Between 5000 and 25000 events were used for each energy. The distributions of the reconstructed energy were fitted and well-described by Gaussian functions (see also Sec. 9.2), whose standard deviation divided by its mean is the energy resolution.

The measured resolutions as a function of the beam energy are in Fig. 11.3. The orange curve is a fit of Eq. 2.16 to the data. The fit returns a sampling term of (10.0 $\pm$ 0.6)% and a constant term of (1.16 $\pm$ 0.06)%.

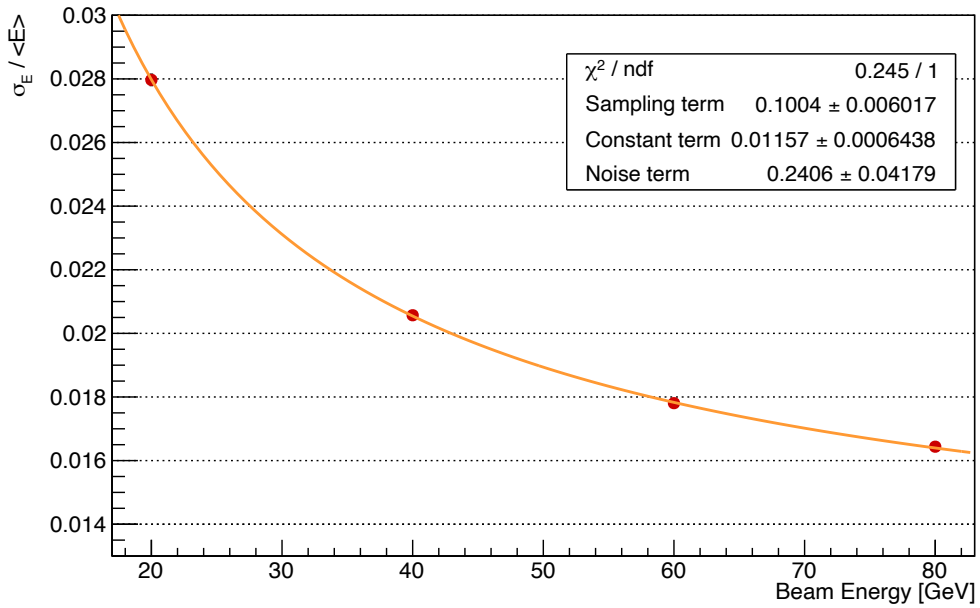

FIGURE 11.3: Energy resolution of the Lead/Polystyrene prototype measured at 3°+3° incidence angle of the electron beam. The line is a fit of Eq. 2.16 to the data.

11.3 Time resolution

Time resolution was studied both at DESY and SPS with electron beams hitting the centre of the prototype in a 6x6 mm^2 square with an incidence angle of 3°+3°. The cells were equipped with R11187 PMTs in direct dry contact with the central bundles. In DESY, the PMTs were biased at 480 V (front) and 540 V (back); at SPS, 400 V (front) and 410 V(back).

The prototype achieves a resolution down to 30 ps at 5 GeV, below 20 ps above 20 GeV, and down to 8 ps at 100 GeV. The front performs worse than the back. From 60 GeV, the resolution is dominated by the back section.

The performance of the cells coupled via light guides was similar to the bundles. In view of the upgrade, it must be noted that hadronic showers starting in the ECAL

[1]The fibres are the same of Sec. 10.1, but round and double-cladded.

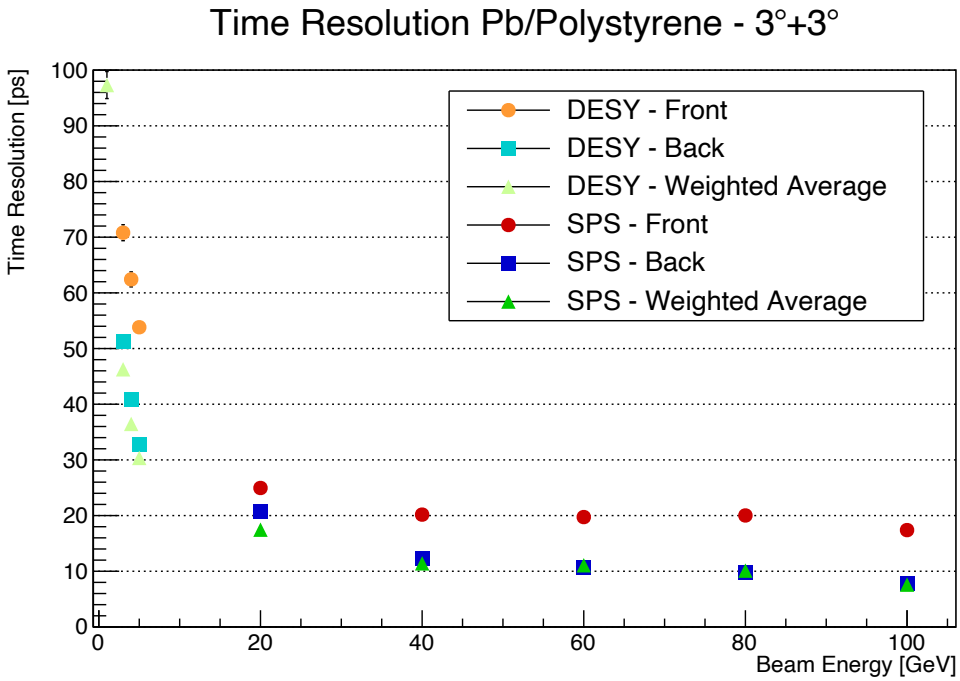

FIGURE 11.4: Time resolution of the Lead/Polystyrene prototype measured at 3°+3° incidence angle of the electron beam with R11187 PMTs.

and developing to the HCAL could induce large signals in a fibre bundle in the back section. Moreover, the light produced in 1 fibre in the prototype is transported via the bundle to a single point on the PMT photocathode, whereas the light guide distributes the light from a fibre over an area of the photocathode, which helps averaging out its inhomogeneities – e.g. in quantum efficiency and in transit time.

11.3.1 Time resolution at the border of different cells

To evaluate the performance away from the cell centre, time resolution was studied scanning the prototype surface between the centre of the central and top cells with a 60 GeV electron beam (Fig. 11.5). The beam was moved in 3 positions – centre of the central cell, separation central-top cell, centre of the top cell. The space between the 2 centres was divided into 7 bins 5x5 mm^2 (see the orange slices in Fig. 11.5, left) and time resolution was computed in each of them for both cells interested. Additionally,

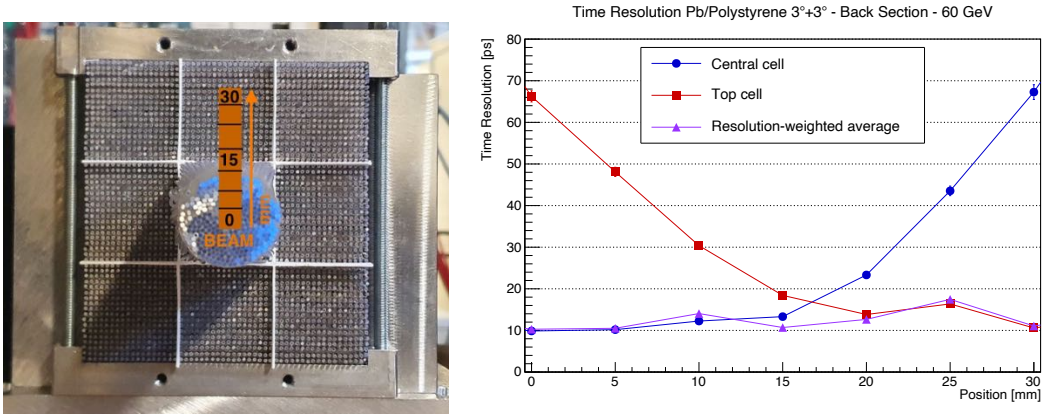

(A) Prototype (B) Time resolution

FIGURE 11.5: Time resolution of the back section of the Lead/Polystyrene prototype measured in different positions between the central and top cells with 60 GeV electrons. A) Front picture of the prototype, highlighting the 7 positions wherein the time resolution was measured. B) Time resolution for the central and top cell of the back section, and for the resolution-weighted average of the cells timestamps.

the resolution was studied using as timestamp the resolution-weighted average of each cell in the corresponding space bin.

Fig 11.5 right shows the results of the back section alone: Time resolution is below 20 ps – mostly at 10 ps level – as long as the electron enters the prototype within the cell's boundaries, degrading significantly outside; combining the information from both cells keeps the resolution closer to 10 ps throughout the scan. Note that the resolution is asymmetric between the 2 cells. The effect is not explained, but notable points are the light guide at the top, and the incidence angle (front lifted). A systematic study between identical cells is required, but the current test suggests that the prototype has the same resolution independently of the electron hit point.

Part IV

Monte Carlo Simulations

Monte Carlo Simulations

Monte Carlo methods are mathematical techniques that use random number extractions to approximate exact calculations. Such methods are often employed to simulate complex systems with many degrees of freedom whose evolution cannot be predicted analytically.

Monte Carlo simulations are critical in designing particle detectors, allowing testing new ideas and monitoring quantities normally not accessible empirically, e.g. the true energy deposition. However, simulations of complex systems require validation by tuning their free parameters to match observations.

The following chapters are dedicated to the development and application of Monte Carlo simulations in the frame of the LHCb ECAL UII:

- Chapter 12 describes the development and validation of the Hybrid Monte Carlo simulation framework;
- Chapter 13 presents studies on the effect of the Upgrade II background on the timing performance of a Tungsten/GAGG prototype.

The framework is in use by the whole LHCb ECAL UII collaboration. It was instrumental in the design of the prototypes and the study of the ECAL performance with physics benchmarks, testified by its use in the production of the Upgrade II Framework Technical Design Report. [32]

Chapter 12

The Hybrid Monte Carlo Simulation Framework

The simulation framework was developed with Dr Marco Pizzichemi of Milano-Bicocca and CERN. It is a C++ Monte Carlo software based on the GEANT4 toolkit [13] to study the response of Shashlik and SPACAL of arbitrary geometry, as well as of the whole LHCb ECAL to arbitrary particle fluxes.

The software simulates the energy deposition in the calorimeter, the production and transport of Cherenkov and Scintillation light, the photodetector response, and the time pick-off. This open-source code runs on linux machines and it comes with a set of scripts to submit jobs on batch systems as HTCondor or the LHCb Grid. The steps of the simulations are sketched in Fig. 12.1 and discussed in the rest of the chapter. The CERN Gitlab repository can be found here [108].

12.1 Geometry, Input, and Radiation-Matter Interaction

The framework reproduces in GEANT4 calorimeter modules of SPACAL and Shashlik with arbitrary geometry – e.g. length, size, inter-fibre distance – and are built using elementary geometries available in GEANT4. Single modules are utilised to validate the simulation with testbeam data, to design prototypes, and to study their performance.

Once a module is defined it can be replicated in space until it fills up a volume. Different modules occupy different volumes, defined by the user. This allows simulating the several configurations of the present and future LHCb ECAL.

The framework takes in input both single or multiple particles, for instance to study decay channels over a background. The default physics list for the radiation-matter

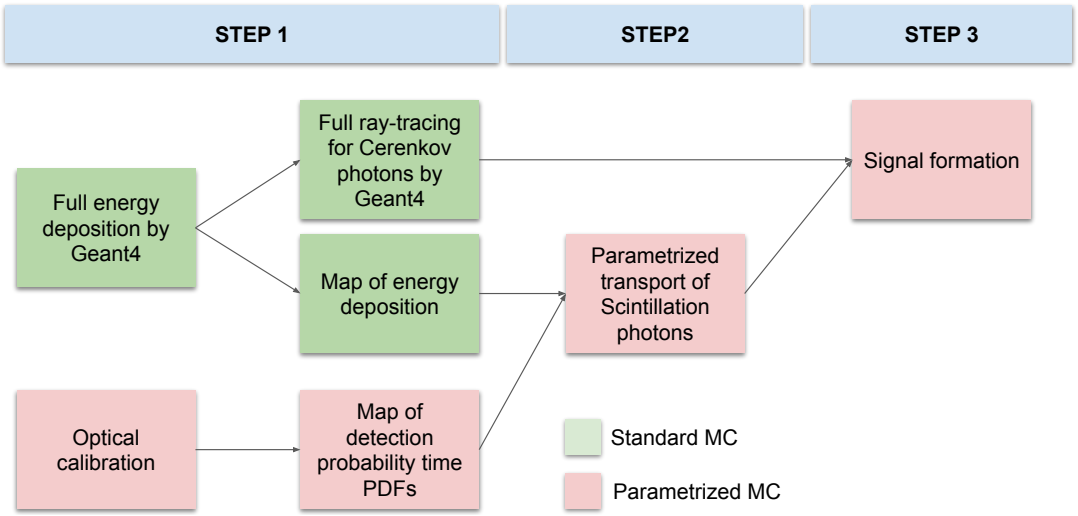

FIGURE 12.1: Chart of the Hybrid Monte Carlo simulation steps.

interaction is FTFP_BERT. GEANT4 simulates the interaction of the incident particle(s) with the detector, producing a map (x, y, z) of the energy deposits (see Fig. 12.3, left). The map is saved to disk along with other information, e.g. the incident particle's initial momentum.

Beside the energy deposits, the particles interacting with the detector can produce Cherenkov photons. The simulation of these photons is performed by GEANT 4, using its raytracing library. Raytracing is a technique to simulate the travel of optical photons in a medium by describing them in terms of rays and propagating them by discrete amounts relying on the laws of Geometrical optics. Raytracing is crucial to reproduce with accuracy the light transport, including the effects of surface non-idealities [109]. The photon-surface interaction in GEANT4 is based on the UNIFIED model [110]. The UNIFIED model describes the interaction of an optical photon with a non-ideal surface. The surface is divided into micro facets oriented according to a distribution whose average is the direction of the ideal surface; the narrower the distribution, the more the surface behaves as polished.

The Cherenkov light is generated inside the active material of the calorimeter and propagated towards the face coupled to the PMT. If a photon is refracted out, it is stopped and the timestamp saved, along with information on the position generation and wavelength.

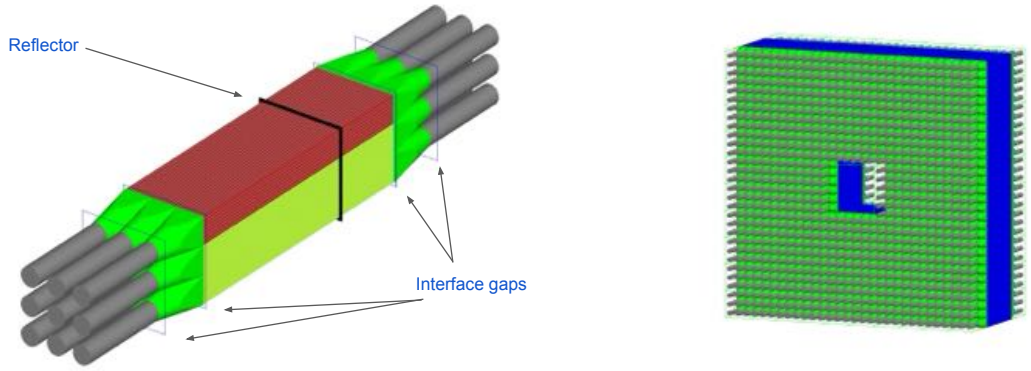

FIGURE 12.2: Example of simulated geometries. On the left, a Tungsten/GAGG prototype as the one tested in Chap. 9. The 2 sections are split by a reflector, the prototype is filled with 2 materials (red and yellow) and the cells are coupled to the PMTs via light guides. 100 μm air gaps are added to simulate Fresnel reflections at the interfaces between media. On the right, a series of such modules reproduced to simulate part of the LHCb ECAL.

The scintillation parameterisation is discussed in the next section.

12.2 Scintillation Photons: the Hybrid Simulation

The large energy deposits simulated in HEP can produce several millions and more of scintillation photons per interacting particle, making raytracing computationally expensive.

The solution proposed is a hybrid simulation: the light propagation inside a fibre is studied separately to produce a parameterisation, called optical calibration (see Fig. 12.1), which is employed to simulate the photons reaching the photodetector. The optical calibration consists of producing scintillation photons in several positions of a SPACAL fibre or a Shashlik tile, to calculate a spatial map of probability of light extraction and a time-spread distribution due to the light travel. Both these quantities are wavelength-dependent.

The energy deposits produced in the first step of the simulation are transformed into scintillation photons according to the scintillation parameters of the active material, e.g. light yield, emission spectrum, kinetics. The information of the calibration is used as probability distribution to produce a list of photons extracted, with their timestamp.

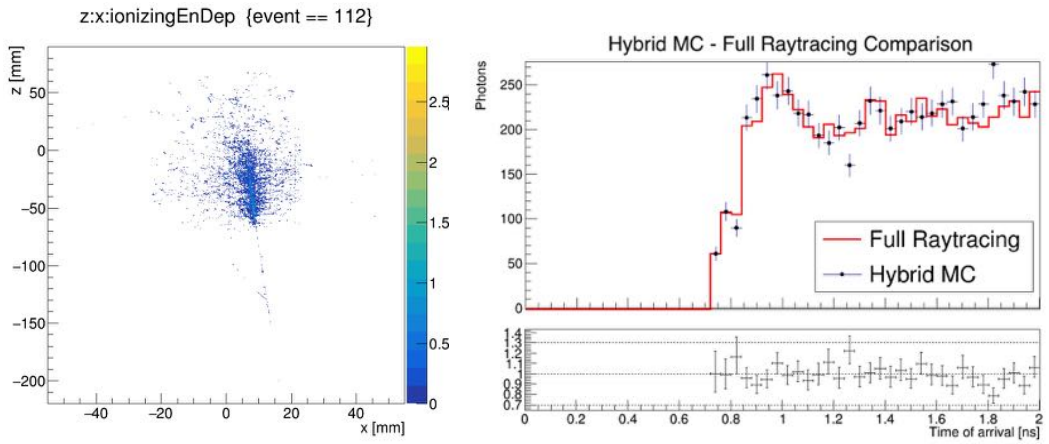

FIGURE 12.3: Left: map (x, z) of the energy deposits by an electron hitting a Tungsten/GAGG SPACAL, for illustrative purpose. Right: time distribution of the scintillation photons exiting a GAGG fibre produced by a 1 GeV electron obtained by full raytracing and Hybrid Monte Carlo.

The calibration must be performed only once per geometry configuration, thus cutting down significantly the computation time of a simulation: raytracing is not performed for every photon but the realism of the simulation is maintained.

Several tests were performed simulating 1 GeV electrons on SPACAL modules and propagating the produced light with full raytracing and with the hybrid approach. The distributions of the time of detection of the photons were compared (e.g. Fig. 12.3, right). The Kolmogorov test validated quantitatively the comparison, demonstrating that the hybrid approach maintains the realism of a full raytracing optical simulation.

12.3 Pulse Production and Time Pick-off

The output of the previous steps is a list of photons containing information such as the wavelength, the timestamp of exit from the fibres, and the cell of the prototype. The last simulation step builds the waveform of the photodetector starting from the photons assigned to it. First, the quantum efficiency of the photodetector is applied to reject part of the photons according to their wavelength. An additional fraction of the photons can be deleted to simulate losses due to a light guide. A digitised pulse is initialised with a user-defined sampling and length, by creating an array of zero voltages. The electronic

noise can be added by summing to each sample a random voltage value distributed according to a Gaussian function with a width defined by the user.

A time smearing is applied to each photon detected to account for the transit time spread of the photodetector. Then, for each of them, the single photoelectron pulse is computed and summed to the digitised pulse.

The detectors are assumed to behave linearly, and the dynamic range of the electronics is considered infinite. Multiple photodetectors are implemented, each with a characteristic QE, TTS, and single photoelectron response. When no detailed information was available, the datasheet figures were used.

For example, the R7899-20 underwent a detailed characterisation, and the single photoelectron response was parameterised as:

$$A(t) = A_0 t^2 e^{-\frac{t}{\tau}}, \tag{12.1}$$

where $\tau = 1$ ns, and A_0 was found to be a random variable with a distribution well described by as a Gamma pdf:

$$p(x) = \frac{1}{\Gamma(\alpha)\theta^\alpha} x^{\alpha-1} e^{-\frac{x}{\theta}}, \tag{12.2}$$

where $\alpha = 6$ and $\theta = \frac{1}{6}$.

The framework can save the raw pulses produced. A utility program is offered to apply a configurable digital CFD and obtain a timestamp, as described in Sec. 8.4.2.

12.4 Energy Resolution: Measurement-Simulations Matching

The Hybrid Monte Carlo framework has become a staple in the LHCb ECAL UII group, being currently used throughout the collaboration for design optimisation and physics benchmarking. [32]

This section compares the energy resolution obtained in testbeam and simulations, the first of a series of validation tests performed.

12.4.1 Tungsten/GAGG SPACAL

The energy resolution of the Tungsten/GAGG SPACAL to electrons at multiple incidence angles was compared to the measurements performed in testbeam, discussed

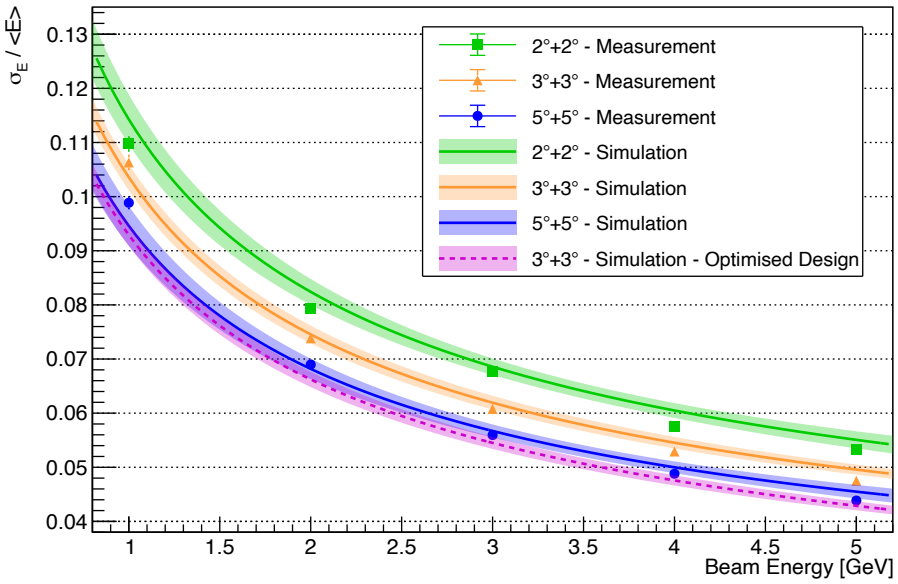

FIGURE 12.4: Energy resolution to electrons at multiple incidence angles in a Tungsten/GAGG SPACAL. Comparison between testbeam measurements (Fig. 9.3) and Hybrid Monte Carlo simulations. Simulations points are fitted with Eq. 2.16 and drawn with a 2-standard-deviation error band. The magenta line is the energy resolution to electrons at 3°+3° incidence angle for an optimised design (see text).

in Sec. 9.2. Fig. 12.4 shows the agreement between the two. Simulation data points in the range of 1 to 6 GeV were fitted with Eq 2.16 and the fit function is drawn with a 2-standard-deviation error band. The trend with increasing incidence angle is reproduced and the incidence angles are distinguished, albeit with some discrepancy. As discussed in section 9.2, underestimated systematics could explain the mismatch towards higher energies, thus requiring SPS data and light yield measurements to finely-tune the framework.

The framework was then employed to simulate a module of 121.2×121.2 mm^2 with the optimised design foreseen for the LHCb Upgrade II, discussed in the Framework Technical Design Report [32]. Differences are: a shorter interfibre distance of 1.67 mm, longer sections of 45 and 105 mm, and less material budget between the two removing the stainless steel plates needed for making the sections independent. This optimised

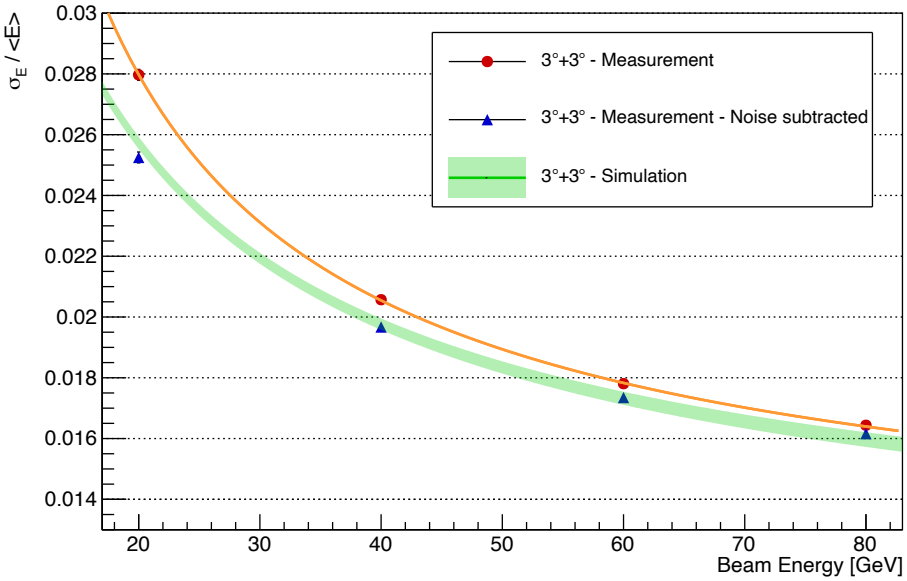

FIGURE 12.5: Energy resolution to electrons at 3°+3° incidence angle in a Lead/Polystyrene SPACAL. Comparison between testbeam measurements (Fig. 11.3) and Hybrid Monte Carlo simulations. The blue markers are the measurements but subtracting in quadrature the noise term contribution (see Sec. 11.2). Simulations points are fitted with Eq. 2.16 and drawn with a 1-standard-deviation error band.

design achieved at 3°+3° incidence angle sampling and constant terms of (9.2 ± 0.1)% and (1.18 ± 0.03)%, respectively (magenta curve in Fig. 12.4).

12.4.2 Lead/Polystyrene SPACAL

Similarly to the previous section, the energy resolution of the Lead/Polystyrene SPACAL to electrons at 3°+3° incidence angle was compared to the measurements performed in testbeam, discussed in Sec. 11.2. Fig. 12.5 is an update of Fig. 11.3 with simulated resolutions: these points, in the range of 1 to 100 GeV, were fitted with Eq 2.16 and the fit function is drawn with a 1-standard-deviation error band. The simulations were performed without noise, which explains the discrepancy with the measurements: subtracting in quadrature from the latter the noise contribution observed in Fig. 11.3 gives the blue markers, agreeing with the simulations.

Chapter 13

Spillover in a Tungsten/GAGG SPACAL

In the LHC protons are packed into bunches separated by 25 ns, a distance called bunch spacing. Collisions take place when two opposite bunches cross every 25 ns, or, in other words, at 40 MHz rate. Spillover is the situation in which the response of a detector induced by one proton interaction extends over multiple bunch crossings.

Chapter 6 demonstrates the timing capabilities of GAGG inorganic crystals, while 9 shows that a SPACAL of Tungsten/GAGG achieves excellent timing performance down to tens of ps. Nonetheless, commercial GAGG crystals scintillate with a fast decay component of about 40 ns and a slow one of hundreds of nanoseconds, making spillover an issue to investigate.

13.1 Simulation Details

The study aimed to assess the effect of spillover in a Tungsten/GAGG module, focusing on only 1 front and 1 back cells located as in Fig. 13.1. It was performed in collaboration with Dr Stefano Perazzini and Dr Vincenzo Vagnoni, INFN Bologna.

Proton collisions were simulated with Gauss, part of the general LHCb simulation framework [111, 112]. A total of 20000 bunch crossing were simulated with an instantaneous luminosity of $1.5\text{x}10^{34}$ $\text{cm}^{-2}\text{s}^{-1}$, corresponding to an average of 56 proton-proton collisions (or primary vertices, PVs) per bunch crossing[1]. The software simulates also

[1]The dataset was employed for other studies which required forcing in each bunch crossing the presence of at least one PV generating a $B^0 \to \pi^+\pi^-\pi^0$ decay. Doing that raises the average PV to 57, increasing the occupancy by up to $1/56 \leq 2\%$, an effect totally negligible for this study.

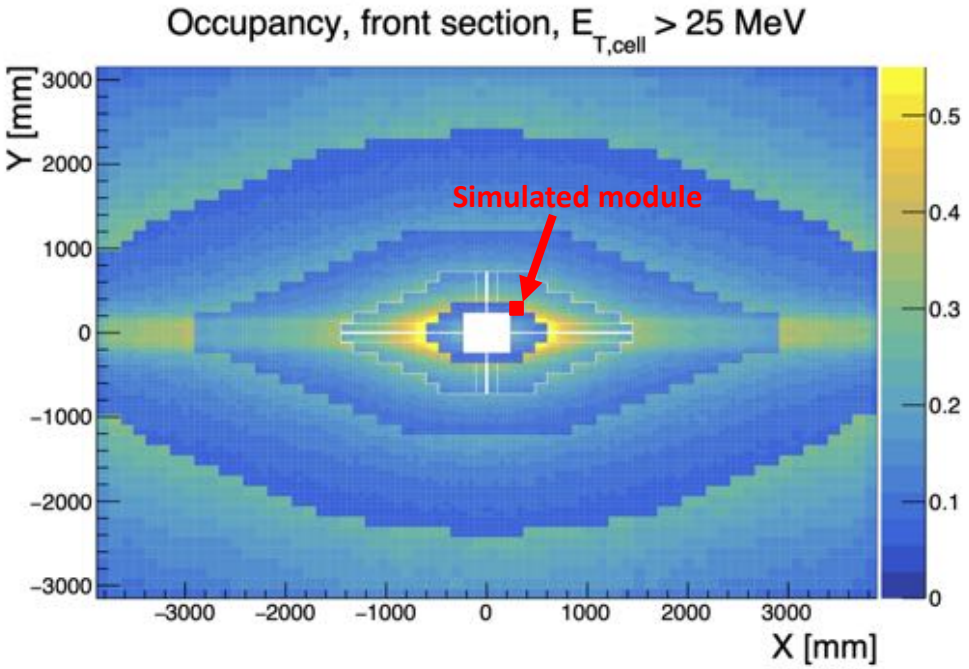

FIGURE 13.1: Map of the expected occupancy at the LHCb Upgrade II ECAL showing the position of the simulated Tungsten/GAGG module. From reference [32].

the interaction of all the produced particles with the material of the LHCb Upgrade I detector upstream of the ECAL. The Hybrid Monte Carlo was employed to simulate the interaction of particles with the SPACAL modules and the consequent responses of the DAQ and the digitised waveforms. The digitised pulses pulses were chained shifting each bunch crossing by 25 ns later with respect to the previous one. The output of this procedure constitutes what in the following will be referred to as background.

To assess the performance of the calorimeter in a known configuration, single electrons were simulated hitting the centre of the interested cells with $1.4° \oplus 1.4°$ incidence angle, as if coming from the LHCb interaction point. The resulting pulses were summed to the background every 50 bunches. To profit from all the statistics available, once the electron pulses reached the end of the chain, the latter was duplicated and the electron pulses were again summed to the background every 50 events, but starting one event later, and so on for 50 chains. The exercise was repeated for electrons of 5, 10, 25, and 50 GeV. These electron pulses will be referred to as signal in the following.

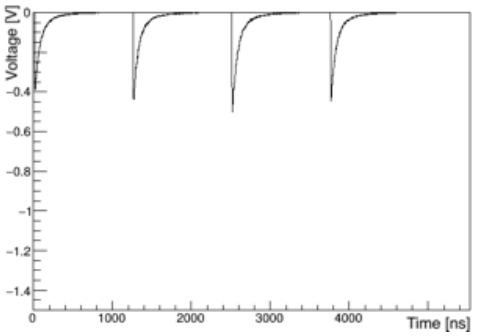

(A) Front cell - signal only

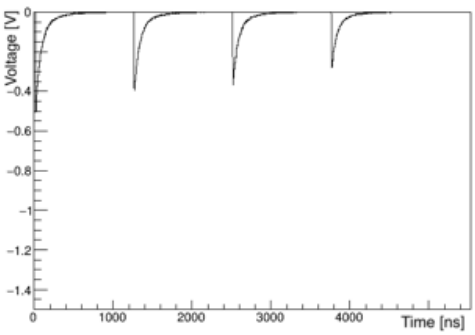

(B) Back cell - signal only

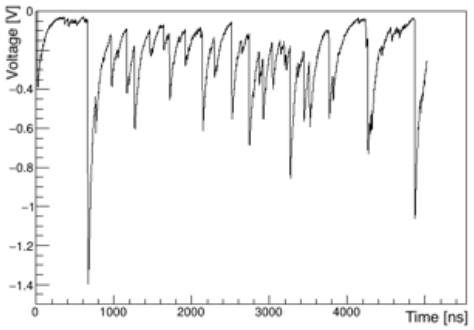

(C) Front cell - signal and background

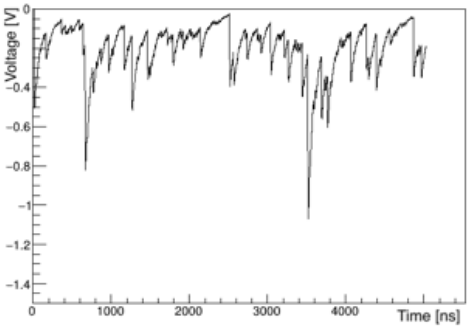

(D) Back cell - signal and background

FIGURE 13.2: Snapshot of the chained pulses. The signal produced by a 5 GeV electron is superimposed to the background (see text for details).

The pulses were produced using the R7899-20 PMT and digitised with a 5 GS/s rate. No limits were imposed on the input dynamic range and the electronic noise was set to zero. The PMTs response was assumed to be linear. Examples of the pulse chains are visible in Fig. 13.2. Timestamps were computed by applying CFD to the bunches containing the electron signal, with and without background. The latter configuration was used as reference.

A constant electronic delay was added to each event to make sure that no interaction with the calorimeter could happen within 6 ns from the bunch crossing. These first samples were used to compute the baseline for the CFD algorithm. Two pulse shaping solutions were tested to compensate for spillover: a single delay line (SDL) clipping and the subtraction of an exponential function fitted to the baseline.

The SDL shaping consists in having part of the signal connected to a cable of known length and termination resistor. Such arrangement produces for an incoming signal a

reflection of polarity and amplitude proportional to the resistor value, which is then summed to the original signal delayed by the cable length. Tuning the resistor and cable length allows shortening the original electronic signal. The SDL clipping was mimicked taking the amplitude value of the pulse at time t, scaling it and inverting the sign, and adding it to the pulse with a delay δ_t:

$$V_{out}(t) = \frac{1}{2}\left(V_{in}(t) - \frac{R_{clip} - Z_0}{R_{clip} + Z_0} V_{in}(t - 2t_{clip})\right) = \frac{1}{2}\left(V_{in}(t) - r\, V_{in}(t - \delta_t)\right) \quad (13.1)$$

where R_{clip} and t_{clip} are the end resistance and the delay of the line and $Z_0 = 50\ \Omega$ the line impedance. For simplicity, the parameters used were δ_t and r. The parameter δ_t was chosen 4 ns and the scale factor r tuned to match the pulse attenuation due to the exponential decay time of the scintillation, i.e. $r = e^{-\frac{\delta_t}{\tau_d}}$; in case of multiple decay components, the effective decay time was selected unless otherwise specified.

The exponential subtraction consisted in fitting with an exponential function the samples otherwise used to compute the baseline. The fitted function was then subtracted from all the samples of the event and the default CFD algorithm applied.

13.2 Spillover in Commercial GAGG

Time resolution was studied combining front and back sections for a commercial-like GAGG crystals (Fig. 13.3, Table 13.1). The blue circles show the resolution without background, which lies below 20 ps. Adding the background (black squares) degrades it significantly, reaching up to 30 ps at 50 GeV, more than 4 times worse, and 115 ps at 5 GeV, almost 6 times worse. Larger degradation at lower energies is expected: the slew rate of the leading edge is proportional to the pulse amplitude, which is lower at lower energies; the decaying spillover pulse causes a mismeasurement of the signal amplitude, displacing the CFD threshold; the mismeasurement is reduced if the pulse leading edge is much shorter than the decay time constant of the spillover.

The shaping techniques mitigate partially the degradation induced by the background. The exponential subtraction is more effective than the SDL, in particular at the lower energies.

The timestamp distributions for the shaped pulses showed a Gaussian core with tails (similar to Fig. 13.4, left). The Gaussian fit to the distribution for the exponential subtraction mitigates almost completely the deterioration at energies above 10 GeV.

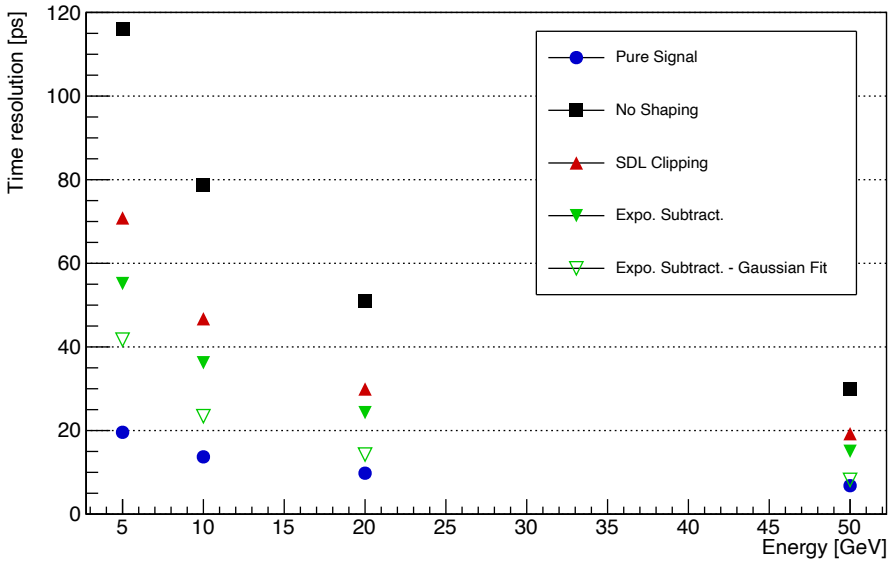

FIGURE 13.3: Time resolution with Commercial GAGG combining the front and back sections for electrons of different energy and all the shaping technique tested. The blue circles are only the signal electrons without background, the black squares are without any shaping, the others are with SDL clipping or exponential fit of the baseline.

13.3 Spillover in Faster GAGG

The effect of spillover was studied varying the light output and decay time of GAGG, according to Table 13.1. The time resolution combining front and back sections is shown in Fig. 13.5 and Fig. 13.6.

The Fast GAGG features a single decay component of 15 ns. The light output was decreased to keep the decay time to light output ratio equal to the Commercial GAGG's one. Although faster than the Commercial GAGG, the decay component causes spillover and a significant deterioration of resolution, such that no major difference is observed without shaping. On the other hand, the effect of the shaping is more pronounced but still not sufficient to compensate for the performance loss. The Gaussian fit to the distribution for the exponential subtraction mitigates almost completely the deterioration at all energies.

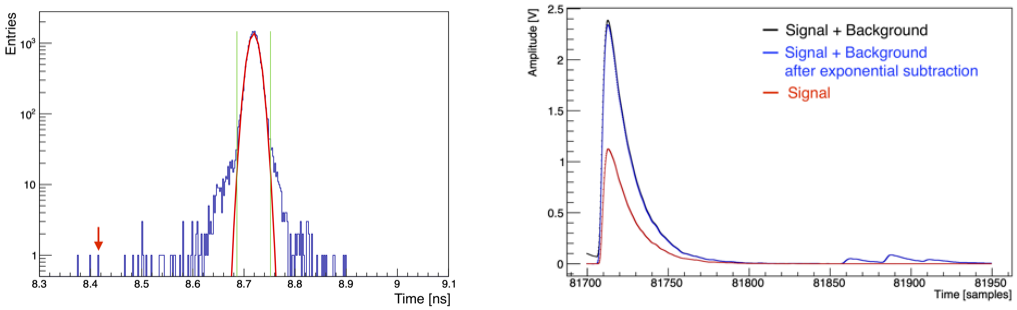

(A) Timestamp distribution (B) Illustrative pulse

FIGURE 13.4: (A) Timestamp distribution combining front and back sections applying the exponential subtraction shaping. The red line is a Gaussian fit and the green vertical lines mark 3σ from the distribution mean. The tails are caused by pile-up within the same bunch crossing. The red arrow points at the event shown in (B). Note that some spillover is visible before the signal pulse which is compensated for by the exponential fit of the baseline.

The Ultrafast GAGG is an even faster GAGG along the lines of the samples characterised in Sec. 6.2. About 92% of the total charge produced is contained within the 25 ns bunch spacing, significantly reducing spillover. Time resolution without background worsens – due to the reduction in light output being larger than the acceleration of the effective decay time $\tau_{d,eff}$ – but the deterioration with background is significantly less than for the other materials. However, even for this material, adding the background degrades the resolution, and the shaping techniques bring no improvement.

This loss of resolution in absence of spillover is caused by pile-up within the same bunch. When a second particle hits the cell with a delay such that the pulse induced overlaps with the leading edge of the first, the 2 pulses merge and the CFD algorithm returns a combination of the 2 timestamps. The effect is predominant at low energy, because when the energy deposited by the two particles differs significantly the pulse amplitudes differ accordingly and the highest dominates the CFD algorithm. Fig. 13.4 left shows the timestamp distribution for the Fast GAGG at 50 GeV with exponential subtraction. It is visible the Gaussian fit and the tails. An example event of the left tail (see the red arrow) is visible in Fig. 13.4, right. Adding the background more than doubles the pulse amplitude due to pile-up on the leading edge. Conversely, some spillover is removed by the exponential subtraction shaping. The fraction of events outside 3 σ of the Gaussian fit (indicated by the 2 vertical lines) decreases from 4.2% at

TABLE 13.1: Table of the simulated materials discussed in this chapter. $\tau_{d,i}$ is the decay time and R_i the abundance of the i-th component. The photon yields for the Commercial and the 4 Fast GAGG are chosen to keep constant the ratio of photon yield to effective decay time and, thus, the intrinsic time resolution of the material (see Eq. 4.9).

	Photon Yield [MeV^{-1}]	$\tau_{d,1}$ [ns]	ρ_1 %	$\tau_{d,2}$ [ns]	$\tau_{d,eff}$ [ns]
Commercial GAGG	35 000	40.0	66	153	53.3
Fast GAGG	9 853	15	100	-	15
Fast GAGG$_{15,40}$	13 137	15	60	40	20.0
Fast GAGG$_{15,60}$	14 075	15	60	60	21.4
Fast GAGG$_{15,150}$	15 395	15	60	150	23.4
Ultrafast GAGG	1 000	1.7	60	15	2.6

5 GeV to 3.1% at 50 GeV.

The effect of pile-up is irreducible using the shaping techniques mentioned. Studies are ongoing to identify such events by pulse shape discrimination, e.g. via the slew rate of the leading edge, and possibly extract timing of both particles with template fitting [113] or machine learning.

13.3.1 Effect of a Long Decay Time Component

The scintillation kinetics of GAGG crystals is usually well described by 2 decay time components: a faster and slower one in the hundreds of ns range. The impact of a second slow component on time resolution was evaluated by adding to the Fast GAGG second decay times of 40, 60 and 150 ns (see Table 13.1). Fig. 13.7 shows the time resolution for signal electrons of 5 GeV, chosen to be more sensitive to the effect of the background. The resolution combining front and back sections without any shaping is independent of the second decay component. When applying shaping techniques, reducing the decay time from 150 ns to 0 ns improves the resolution by about 6% for the SDL clipping and 3% for the exponential subtraction. This could be due to the fact that both shaping techniques are designed for single exponential pulses.

The slow component does not influence the resolution for the reason mentioned in Sec. 13.2: the decay constant of the second component is much slower than the rise time of the pulses, hence the spillover is approximately constant during the leading

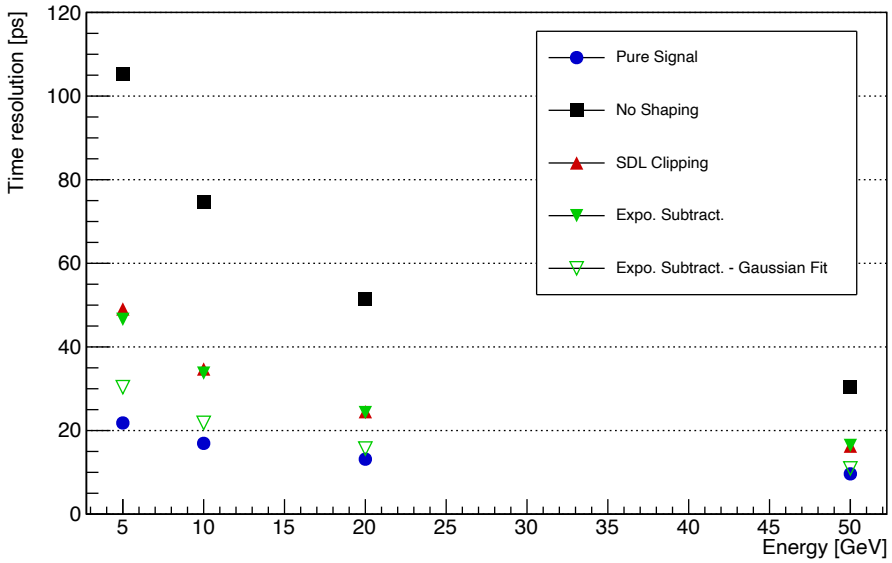

FIGURE 13.5: Time resolution achieved by the Fast GAGG (see Table 13.1) combining the front and back sections for electron signal of varying energy and with all the shaping technique tested. The blue circles are only the signal electrons without background, the black squares are without any shaping, the others are with SDL clipping or exponential fit of the baseline.

edge of the signal. The mismeasurement of the signal pulse amplitude with respect to the baseline caused by the decaying spillover pulse is, thus, negligible.

A simple exercise shows the reasoning behind this conclusions. A pulse of 1 V at $t = 0$ of the Fast GAGG set is described by:

$$f(t) = A_0 \left(\frac{0.6}{\tau_{d,1}} e^{-\frac{t}{\tau_{d,1}}} + \frac{0.4}{\tau_{d,2}} e^{-\frac{t}{\tau_{d,2}}} \right) = f_1(t) + f_2(t), \tag{13.2}$$

where $A_0 = 20$, $\tau_{d,1}$ and $\tau_{d,2}$ are 15 and between 40 and 150 ns, respectively. Modelling the baseline drift caused by the decreasing spillover pulse as noise, assuming a signal pulse of amplitude 1 V and a rise time $\delta_r = 5$ ns, and approximating its slew rate as

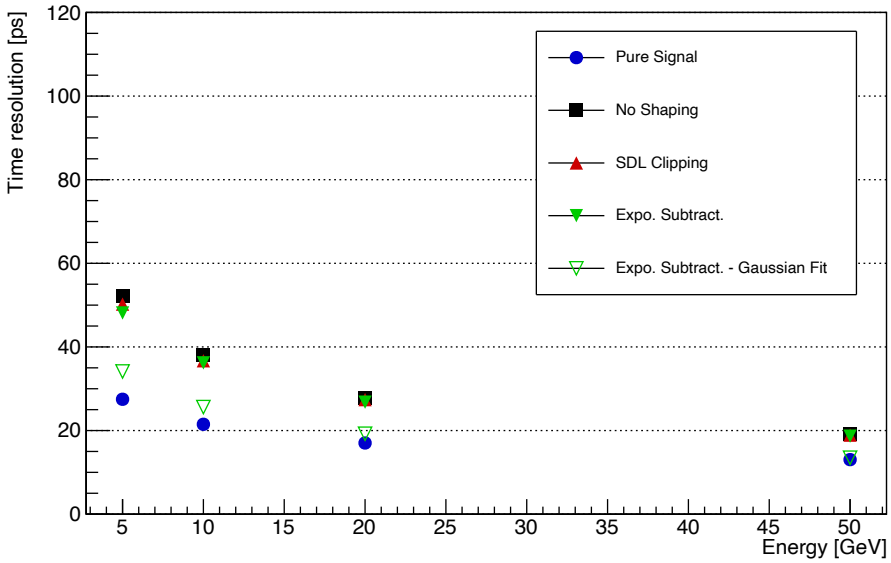

FIGURE 13.6: Time resolution achieved by the Ultrafast GAGG (see Table 13.1) combining the front and back sections for electron signal of varying energy and with all the shaping technique tested. The blue circles are only the signal electrons without background, the black squares are without any shaping, the others are with SDL clipping or exponential fit of the baseline.

$\frac{dV}{dt} \simeq \frac{\text{amplitude}}{\text{rise time}} = \frac{1}{5}$ [V/ns], the contribution to the time resolution is:

$$\sigma_t \propto \frac{\sigma_N}{dV/dt} \simeq \frac{f(t) - f(t+\delta_r)}{1/\delta_r}, \tag{13.3}$$

and plugging some numbers shows how decay times of hundreds of ns produce second-order jitters compared to the fast component in the first bunch spacings.

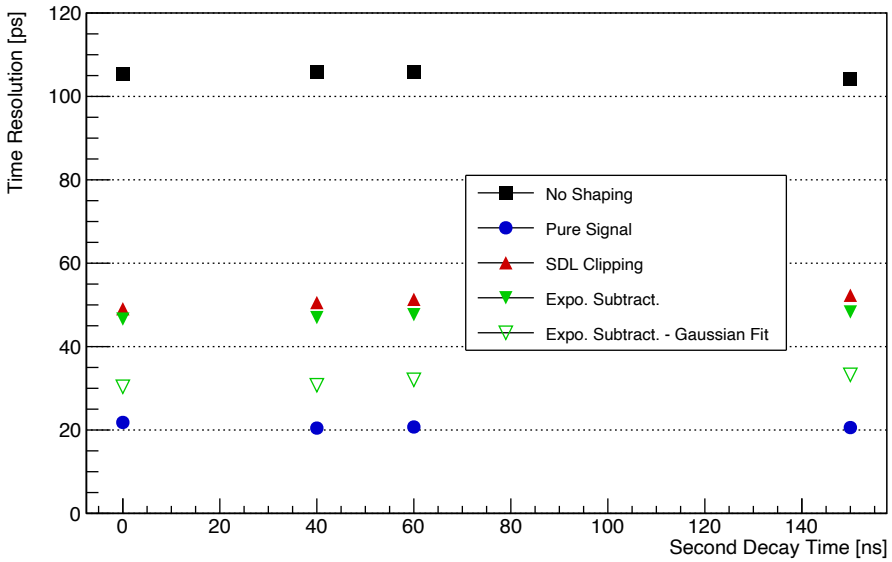

FIGURE 13.7: Time resolution front and back combined achieved by the set of Fast GAGG with various second component (see Table 13.1) for 5 GeV electron signal and with all the shaping technique tested. The blue circles are only the signal electrons without background, the black squares are without any shaping, the others are with SDL clipping or exponential fit of the baseline.

Part V

Conclusions and Outlook

Conclusions

The goal of this PhD thesis was to search, develop, and test a solution for the upgrade of the LHCb ECAL.

This work was the outset of what is now the LHCb ECAL Upgrade II, or PicoCal project. For – and thanks to – this reason, it covered a broad spectrum of topics: development and characterisation of scintillating crystals, designing and testing of prototypes, programming of a Monte Carlo framework and its use for further optimisation.

Part II was dedicated to the characterisation and development of new scintillating materials. The research focused mainly on the centremost part of the calorimeter which will face order of 1 MGy radiation dose. Cerium-doped GAGG withstands this radiation level. Samples from worldwide producers were characterised achieving timing performance close to LYSO:Ce, the current standard for timing. The most promising samples were selected to be used for prototypes.

Nonetheless, even the fastest GAGG featured a decay time too long for the rate of interactions of the LHC. The LUMDETR 2021 conference and the Crystal Clear Collaboration meetings were ideal grounds to call for help, and a collaboration with FZU Prague led to a set of GAGG samples with decay time reduced by up to a factor 40, but keeping competitive time resolution.

For the lower-dose regions, plastic fibres are available commercially but might not be radiation-hard enough. Polysiloxane scintillators could be the solution, and the preliminary samples tested in collaboration with INFN Legnaro obtained promising results.

Part III was dedicated to the three technologies of SPACAL: Tungsten/Crystal, Tungsten/Plastic, and Lead/Plastic.

The energy resolution of the Tungsten/Crystal and Lead/Plastic SPACAL are in line with the 10% sampling and 1% constant terms for electrons with an incidence angle of $\geq 3^\circ$ both horizontally and vertically. Although not discussed here, the spatial resolution of these prototypes ranged from 2 mm to 0.6 mm with increasing energy for both prototypes. Part of the PhD work was supervising this study [114].

The resolution of Tungsten/Polystyrene was not tested since no prototype sufficiently large to achieve good containment was produced, yet.

Time resolution is at the level of 15 ps or better at high energies for all these prototypes. Using a light guide degrades the resolution due to the additional optical interfaces. However, optical couplings can mitigate these losses. Moreover, the time resolution was found stable moving from one cell to another in a Lead/Plastic SPACAL.

Part IV illustrated the Monte Carlo simulation framework developed during this PhD for the optimisation of the prototypes and for studies of physics performance. Thanks to its hybrid approach, it keeps the realism of a raytracing light simulation but saves orders of magnitude of CPU time. The framework is now in use by the whole LHCb ECAL UII collaboration to design prototypes and study the ECAL performance with physics benchmarks.

The framework was employed to study the time resolution of a Tungsten/GAGG prototype with the expected Upgrade II background. Due to the long decay time of GAGG, spillover of signals from previous bunch crossings degrades the resolution, effect that can be only partially mitigated by pulse shaping techniques. Reducing the decay time is mandatory to preserve the time resolution measured in testbeam.

Outlook

This PhD thesis offers an affordable solution to the needs of LHCb. The results were acknowledged by the whole collaboration and they are considered the baseline option, as shown in the Upgrade II Framework Technical Design Report [32]. It now starts a whole new chapter of R&D towards the production of the calorimeter. A few steps are outlined below.

Regarding GAGG, it is paramount identifying the requirements of light yield and decay time, via Monte Carlo simulations. Further R&D is also needed to produce large-size and homogeneous ingots of the accelerated GAGG.

However, even eliminating spillover, pile-up within the same bunch crossing is a limiting factor to the time resolution, which cannot be resolved by accelerating the scintillation. Techniques must be investigated to identify such situations and possibly reconstruct the two particles. One example could be studying the shape of the rising edge of the pulses exploiting a detailed knowledge of the expected pulse or using machine learning techniques.

The prototyping effort is now directed towards the production and testing of a fully-fledged module that could fit the ECAL. A new Tungsten absorber is under production via 3D-printing. It will comprise blocks of 121x121 mm^2 size and 50 or 40 mm length and will be assembled and tested in 2023. Similarly, a new Lead absorber made with low-pressure casting is being studied and is expected in 2023.

The right PMT in terms of linearity, timing, and geometrical shape is still to be found. R11187 provided excellent timing performance, but their geometry fits only 30 mm cell size. With its 16 mm diameter, R14755U would fit 20 mm but not 15 mm cells. Additionally, some light guide must be designed. PMMA loses transparency due to radiation damage. A solution is to produce only the external frame of the light guide and to coat it with reflective material. Preliminary tests were promising and the solution will be investigated further.

Finally, the electronics employed in testbeam cannot cope with the LHC 40 MHz rate and custom electronics is under study in the collaboration.

In conclusion, only high-quality R&D combining laboratory measurements, testbeams, and Monte Carlo simulations will be able to face these and all the challenges yet to come before the installation of the Upgrade II LHCb ECAL.

Bibliography

[1] C. W. Fabjan and F. Gianotti, "Calorimetry for particle physics", *Rev. Mod. Phys.*, vol. 75, pp. 1243–1286, 4 2003. DOI: 10.1103/RevModPhys.75.1243.

[2] R. Wigmans, *Calorimetry: Energy Measurement in Particle Physics*. Oxford University Press, Sep. 2017. DOI: 10.1093/oso/9780198786351.001.0001.

[3] M Adinolfi *et al.*, "The KLOE electromagnetic calorimeter", *Nuclear Instruments and Methods in Physics Research Section A: Accelerators, Spectrometers, Detectors and Associated Equipment*, vol. 482, no. 1, pp. 364–386, 2002. DOI: https://doi.org/10.1016/S0168-9002(01)01502-9.

[4] *ATLAS liquid-argon calorimeter: Technical Design Report* (Technical design report. ATLAS). Geneva: CERN, 1996. DOI: 10.17181/CERN.FWRW.FOOQ.

[5] G. L. Bayatian *et al.*, *CMS Physics: Technical Design Report Volume 1: Detector Performance and Software* (Technical design report. CMS). Geneva: CERN, 2006, There is an error on cover due to a technical problem for some items.

[6] B. Adeva *et al.*, "The construction of the L3 experiment", *Nuclear Instruments and Methods in Physics Research Section A: Accelerators, Spectrometers, Detectors and Associated Equipment*, vol. 289, no. 1, pp. 35–102, 1990. DOI: https://doi.org/10.1016/0168-9002(90)90250-A.

[7] *The CMS electromagnetic calorimeter project: Technical Design Report* (Technical design report. CMS). Geneva: CERN, 1997.

[8] O. Ganel and R. Wigmans, "On the calibration of longitudinally segmented calorimeter systems", *Nucl. Inst. Meth. A*, vol. 409, no. 1, pp. 621–628, 1998. DOI: https://doi.org/10.1016/S0168-9002(97)01337-5.

[9] R. L. Workman and Others, "Review of Particle Physics", *PTEP*, vol. 2022, p. 083C01, 2022. DOI: 10.1093/ptep/ptac097.

[10] B. B. Rossi, *High-energy particles* (Prentice-Hall physics series). New York, NY: Prentice-Hall, 1952.

[11] S. Lee, M. Livan, and R. Wigmans, "Dual-readout calorimetry", *Rev. Mod. Phys.*, vol. 90, p. 025 002, 2 2018. DOI: 10.1103/RevModPhys.90.025002.

[12] E. Longo and I. Sestili, "Monte carlo calculation of photon-initiated electromagnetic showers in lead glass", *Nuclear Instruments and Methods*, vol. 128, no. 2, pp. 283–307, 1975. DOI: https://doi.org/10.1016/0029-554X(75)90679-5.

[13] S Agostinelli *et al.*, "Geant4—a simulation toolkit", *Nucl. Inst. Meth. A*, vol. 506, no. 3, pp. 250–303, 2003. DOI: https://doi.org/10.1016/S0168-9002(03)01368-8.

[14] R. Wigmans, "New developments in calorimetric particle detection", *Progress in Particle and Nuclear Physics*, vol. 103, pp. 109–161, 2018. DOI: https://doi.org/10.1016/j.ppnp.2018.07.003.

[15] D. Acosta *et al.*, "Results of prototype studies for a spaghetti calorimeter", *Nuclear Instruments and Methods in Physics Research Section A: Accelerators, Spectrometers, Detectors and Associated Equipment*, vol. 294, no. 1, pp. 193–210, 1990. DOI: https://doi.org/10.1016/0168-9002(90)91833-W.

[16] U. Amaldi, "Fluctuations in calorimetry measurements", *Physica Scripta*, vol. 23, no. 4A, p. 409, 1981. DOI: 10.1088/0031-8949/23/4A/012.

[17] R. Wigmans, "On the calibration of segmented calorimeters", *AIP Conference Proceedings*, vol. 867, no. 1, pp. 90–97, 2006. DOI: 10.1063/1.2396942.

[18] R. Wigmans and M. T. Zeyrek, "On the differences between calorimetric detection of electrons and photons", *Nuclear Instruments and Methods in Physics Research Section A: Accelerators, Spectrometers, Detectors and Associated Equipment*, vol. 485, no. 3, pp. 385–398, 2002. DOI: https://doi.org/10.1016/S0168-9002(01)02141-6.

[19] Hamamatsu K.K., *Photomultiplier Tubes: Basics and Applications*. 2017.

[20] G. F. Knoll, *Radiation detection and measurement*. John Wiley & Sons, 2010.

[21] The LHCb Collaboration, "The LHCb Detector at the LHC", *Journal of Instrumentation*, vol. 3, no. 08, S08005, 2008. DOI: 10.1088/1748-0221/3/08/S08005.

[22] E. P. Olloqui and (on behalf ofthe LHCb Collaboration), "Lhcb preshower(ps) and scintillating pad detector (spd): Commissioning, calibration, and monitoring", *Journal of Physics: Conference Series*, vol. 160, no. 1, p. 012 046, 2009. DOI: 10.1088/1742-6596/160/1/012046.

[23] R. Aaij *et al.*, "Observation of photon polarization in the $b \to s\gamma$ transition", *Phys. Rev. Lett.*, vol. 112, p. 161 801, 16 2014. DOI: 10.1103/PhysRevLett.112.161801.

[24] R. Aaij *et al.*, "Measurement of CP violation in the decay $B^+ \to K^+\pi^0$", *Phys. Rev. Lett.*, vol. 126, p. 091 802, 9 2021. DOI: 10.1103/PhysRevLett.126.091802.

[25] R. Aaij *et al.*, "Test of lepton universality with b0 →k*0+decays", *Journal of High Energy Physics*, vol. 2017, no. 8, p. 55, 2017. DOI: 10.1007/JHEP08(2017)055.

[26] E. Picatoste, "Lhcb calorimeter upgrade electronics", Tech. Rep., 22-25 April 2013.

[27] R. Aaij *et al.*, "Expression of Interest for a Phase-II LHCb Upgrade: Opportunities in flavour physics, and beyond, in the HL-LHC era", CERN, Geneva, Tech. Rep., 2017.

[28] C. Abellán Beteta *et al.*, "Calibration and performance of the LHCb calorimeters in Run 1 and 2 at the LHC", Tech. Rep., 2020, All figures and tables, along with any supplementary material and additional information, are available at http://lhcbproject.web.cern.ch/lhcbproject/Publications/LHCbProjectPublic/LHCb-DP-2020-001.html (LHCb public pages).

[29] S Barsuk *et al.*, "Design and construction of electromagnetic calorimeter for LHCb experiment", CERN, Geneva, Tech. Rep., 2000.

[30] Y. Guz, "The lhcb calorimeter system: Design, performance and upgrade", *Journal of Instrumentation*, vol. 12, no. 07, p. C07024, 2017. DOI: 10.1088/1748-0221/12/07/C07024.

[31] A Arefev *et al.*, "Beam Test Results of the LHCb Electromagnetic Calorimeter.", CERN, Geneva, Tech. Rep., 2008, revised version submitted on 2008-05-15 09:09:53.

[32] LHCb Collaboration, "Framework TDR for the LHCb Upgrade II - Opportunities in flavour physics, and beyond, in the HL-LHC era ", CERN, Geneva, Tech. Rep., 2021.

[33] I Bediaga *et al.*, "Framework TDR for the LHCb Upgrade: Technical Design Report", Tech. Rep., 2012.

[34] M. T. Lucchini, "Evolution of the CMS ECAL Performance and R&D Studies for Calorimetry Options at High Luminosity LHC", Presented 03 Dec 2014, 2014.

[35] P. Lecoq, A. Gektin, and M. Korzhik, "Scintillation and inorganic scintillators", in *Inorganic Scintillators for Detector Systems: Physical Principles and Crystal Engineering*. Cham: Springer International Publishing, 2017, pp. 1–41. DOI: 10.1007/978-3-319-45522-8_1.

[36] K. B. Ucer, G. Bizarri, A. Burger, A. Gektin, L. Trefilova, and R. T. Williams, "Electron thermalization and trapping rates in pure and doped alkali and alkaline-earth iodide crystals studied by picosecond optical absorption", *Phys. Rev. B*, vol. 89, p. 165 112, 16 2014. DOI: 10.1103/PhysRevB.89.165112.

[37] G. Tamulaitis *et al.*, "Improvement of the timing properties of ce-doped oxyorthosilicate lyso scintillating crystals", *Journal of Physics and Chemistry of Solids*, vol. 139, p. 109 356, 2020. DOI: https://doi.org/10.1016/j.jpcs.2020.109356.

[38] M. Lucchini *et al.*, "Measurement of non-equilibrium carriers dynamics in ce-doped yag, luag and gagg crystals with and without mg-codoping", *Journal of*

Luminescence, vol. 194, pp. 1–7, 2018. DOI: https://doi.org/10.1016/j.jlumin.2017.10.005.

[39] K. Pauwels, E. Auffray, S. Gundacker, A. Knapitsch, and P. Lecoq, "Effect of aspect ratio on the light output of scintillators", *IEEE Transactions on Nuclear Science*, vol. 59, no. 5, pp. 2340–2345, 2012. DOI: 10.1109/TNS.2012.2183890.

[40] K Pauwels *et al.*, "Single crystalline luag fibers for homogeneous dual-readout calorimeters", *Journal of Instrumentation*, vol. 8, no. 09, P09019, 2013. DOI: 10.1088/1748-0221/8/09/P09019.

[41] M. Korzhik, G. Tamulaitis, and A. Vasil'ev, *Physics of Fast Processes in Scintillators*. Jan. 2020. DOI: 10.1007/978-3-030-21966-6.

[42] E. Delagnes, *What is the theoretical time precision achievable using a dcfd algorithm ?*, 2016. DOI: 10.48550/ARXIV.1606.05541.

[43] B. Sigfridsson, "Theoretical analysis of time resolution in scintillation detectors", *Nuclear Instruments and Methods*, vol. 54, no. 1, pp. 13–28, 1967. DOI: https://doi.org/10.1016/S0029-554X(67)80003-X.

[44] S Gundacker *et al.*, "Time of flight positron emission tomography towards 100ps resolution with l(y)so: An experimental and theoretical analysis", *Journal of Instrumentation*, vol. 8, no. 07, P07014, 2013. DOI: 10.1088/1748-0221/8/07/P07014.

[45] J. B. Birks, "Scintillations from organic crystals: Specific fluorescence and relative response to different radiations", *Proceedings of the Physical Society. Section A*, vol. 64, no. 10, p. 874, 1951. DOI: 10.1088/0370-1298/64/10/303.

[46] P. A. Rodnyi, P. Dorenbos, and C. W. E. van Eijk, "Energy loss in inorganic scintillators", *physica status solidi (b)*, vol. 187, no. 1, pp. 15–29, 1995. DOI: https://doi.org/10.1002/pssb.2221870102.

[47] A. Belsky *et al.*, "Mechanisms of luminescence decay in yag-ce,mg fibers excited by - and x-rays", *Optical Materials*, vol. 92, pp. 341–346, 2019. DOI: https://doi.org/10.1016/j.optmat.2019.04.054.

[48] M. Nikl, "Wide band gap scintillation materials: Progress in the technology and material understanding", *physica status solidi (a)*, vol. 178, no. 2, pp. 595–620, 2000. DOI: https://doi.org/10.1002/1521-396X(200004)178:2<595::AID-PSSA595>3.0.CO;2-X.

[49] M. Nikl *et al.*, "Development of luag-based scintillator crystals - a review", *Progress in Crystal Growth and Characterization of Materials*, vol. 59, pp. 47–72, 2 Jun. 2013. DOI: 10.1016/j.pcrysgrow.2013.02.001.

[50] A. V. Gektin, A. N. Belsky, and A. N. Vasil'ev, "Scintillation efficiency improvement by mixed crystal use", *IEEE Transactions on Nuclear Science*, vol. 61, no. 1, pp. 262–270, 2014. DOI: 10.1109/TNS.2013.2277883.

[51] N. Rebrova *et al.*, "Effects of europium concentration on luminescent and scintillation performance of cs0.2rb0.8ca1xeuxbr3 (0 x 0.08) crystals", *Journal of Rare Earths*, vol. 40, no. 1, pp. 29–33, 2022. DOI: https://doi.org/10.1016/j.jre.2020.08.012.

[52] O. Sidletskiy, "Trends in search for bright mixed scintillators", *physica status solidi (a)*, vol. 215, no. 13, p. 1 701 034, 2018. DOI: https://doi.org/10.1002/pssa.201701034.

[53] M. Korzhik *et al.*, "Engineering of a new single-crystal multi-ionic fast and high-light-yield scintillation material (gd0.5–y0.5)3al2ga3o12:ce,mg", *CrystEngComm*, vol. 22, pp. 2502–2506, 14 2020. DOI: 10.1039/D0CE00105H.

[54] G. Tamulaitis *et al.*, "Improvement of response time in gagg:ce scintillation crystals by magnesium codoping", *Journal of Applied Physics*, vol. 124, no. 21, p. 215 907, 2018. DOI: 10.1063/1.5064434.

[55] G. Tamulaitis *et al.*, "Improvement of the time resolution of radiation detectors based on gd3al2ga3o12 scintillators with sipm readout", *IEEE Transactions on Nuclear Science*, vol. 66, no. 7, pp. 1879–1888, 2019. DOI: 10.1109/TNS.2019.2919898.

[56] L. M. Bollinger and G. E. Thomas, "Measurement of the time dependence of scintillation intensity by a delayed-coincidence method", *Review of Scientific Instruments*, vol. 32, no. 9, pp. 1044–1050, 1961. DOI: 10.1063/1.1717610.

[57] S Seifert, J. H. L. Steenbergen, H. T. van Dam, and D. R. Schaart, "Accurate measurement of the rise and decay times of fast scintillators with solid state photon counters", *Journal of Instrumentation*, vol. 7, no. 09, P09004, 2012. DOI: 10.1088/1748-0221/7/09/P09004.

[58] S. Derenzo, M. Weber, W. Moses, and C. Dujardin, "Measurements of the intrinsic rise times of common inorganic scintillators", *IEEE Transactions on Nuclear Science*, vol. 47, no. 3, pp. 860–864, 2000. DOI: 10.1109/23.856531.

[59] L. Martinazzoli, N. Kratochwil, S. Gundacker, and E. Auffray, "Scintillation properties and timing performance of state-of-the-art Gd3Al2Ga3O12 single crystals", *Nuclear Instruments and Methods in Physics Research, Section A: Accelerators, Spectrometers, Detectors and Associated Equipment*, vol. 1000, Jun. 2021. DOI: 10.1016/j.nima.2021.165231.

[60] S. Gundacker, R. Turtos, E. Auffray, and P. Lecoq, "Precise rise and decay time measurements of inorganic scintillators by means of x-ray and 511 kev excitation", *Nuclear Instruments and Methods in Physics Research Section A: Accelerators, Spectrometers, Detectors and Associated Equipment*, vol. 891, pp. 42–52, 2018. DOI: https://doi.org/10.1016/j.nima.2018.02.074.

[61] F. Anghinolfi, P. Jarron, F. Krummenacher, E. A. Usenko, and M. C. S. Williams, "NINO: an ultrafast low-power front-end amplifier discriminator for the time-of-flight detector in the ALICE experiment", *IEEE Transactions on Nuclear Science*, vol. 51, pp. 1974–1978, 2004.

[62] N. Kratochwil, S. Gundacker, and E. Auffray, "A roadmap for sole cherenkov radiators with sipms in tof-pet", *Physics in Medicine & Biology*, vol. 66, no. 19, p. 195 001, 2021. DOI: 10.1088/1361-6560/ac212a.

[63] S. Gundacker, E. Auffray, K. Pauwels, and P. Lecoq, "Measurement of intrinsic rise times for various L(Y)SO and LuAG scintillators with a general study of prompt photons to achieve 10 ps in TOF-PET", *Physics in Medicine & Biology*, vol. 61, no. 7, p. 2802, 2016. DOI: 10.1088/0031-9155/61/7/2802.

[64] M. Conti, "State of the art and challenges of time-of-flight pet", *Physica Medica: European Journal of Medical Physics*, vol. 25, no. 1, pp. 1–11, 2009. DOI: 10.1016/j.ejmp.2008.10.001.

[65] P. Lecoq *et al.*, "Roadmap toward the 10 ps time-of-flight pet challenge", *Physics in Medicine & Biology*, vol. 65, no. 21, 21RM01, 2020. DOI: 10.1088/1361-6560/ab9500.

[66] S. Vinogradov, "Approximations of coincidence time resolution models of scintillator detectors with leading edge discriminator", *Nuclear Instruments and Methods in Physics Research, Section A: Accelerators, Spectrometers, Detectors and Associated Equipment*, vol. 912, pp. 149–153, Dec. 2018. DOI: 10.1016/j.nima.2017.11.009.

[67] S. Gundacker *et al.*, "Experimental time resolution limits of modern sipms and tof-pet detectors exploring different scintillators and cherenkov emission", *Physics in Medicine & Biology*, vol. 65, no. 2, p. 025 001, 2020. DOI: 10.1088/1361-6560/ab63b4.

[68] S. Gundacker *et al.*, "State of the art timing in tof-pet detectors with luag, gagg and l(y)so scintillators of various sizes coupled to fbk-sipms", *Journal of Instrumentation*, vol. 11, no. 08, P08008, 2016. DOI: 10.1088/1748-0221/11/08/P08008.

[69] S. Ritt, "Design and performance of the 6 ghz waveform digitizing chip drs4", in *2008 IEEE Nuclear Science Symposium Conference Record*, 2008, pp. 1512–1515. DOI: 10.1109/NSSMIC.2008.4774700.

[70] S. Gundacker, R. M. Turtos, E. Auffray, M. Paganoni, and P. Lecoq, "High-frequency sipm readout advances measured coincidence time resolution limits in tof-pet", *Physics in Medicine & Biology*, vol. 64, no. 5, p. 055 012, 2019. DOI: 10.1088/1361-6560/aafd52.

[71] M. T. Lucchini *et al.*, "Effect of Mg2+ ions co-doping on timing performance and radiation tolerance of Cerium doped Gd3Al2Ga3O12 crystals", *Nuclear Instruments and Methods in Physics Research, Section A: Accelerators, Spectrometers, Detectors and Associated Equipment*, vol. 816, pp. 176–183, Apr. 2016. DOI: 10.1016/j.nima.2016.02.004.

[72] K. Kamada *et al.*, "Scintillator-oriented combinatorial search in Ce-doped (Y,Gd) 3(Ga,Al) 5O 12 multicomponent garnet compounds", *Journal of Physics D: Applied Physics*, vol. 44, 50 Dec. 2011. DOI: 10.1088/0022-3727/44/50/505104.

[73] K. Kamada *et al.*, "Composition Engineering in Cerium-Doped (Lu,Gd)3(Ga,Al)5O12 Single-Crystal Scintillators", *Crystal Growth & Design*, vol. 11, no. 10, pp. 4484–4490, 2011. DOI: 10.1021/cg200694a.

[74] K. Kamada *et al.*, "Alkali earth co-doping effects on luminescence and scintillation properties of ce doped gd3al2ga3o12 scintillator", *Optical Materials*, vol. 41, pp. 63–66, Mar. 2015. DOI: 10.1016/j.optmat.2014.10.008.

[75] M. T. Lucchini *et al.*, "Effect of mg2+ ions co-doping on timing performance and radiation tolerance of cerium doped gd3al2ga3o12 crystals", *Nuclear Instruments and Methods in Physics Research, Section A: Accelerators, Spectrometers, Detectors and Associated Equipment*, vol. 816, pp. 176–183, Apr. 2016. DOI: 10.1016/j.nima.2016.02.004.

[76] P. Dorenbos, "Fundamental limitations in the performance of Ce^{3+}–, Pr^{3+}–, and Eu^{2+} –activated scintillators", *IEEE Transactions on Nuclear Science*, vol. 57, no. 3, pp. 1162–1167, 2010. DOI: 10.1109/TNS.2009.2031140.

[77] I. V. Khodyuk, J. T. M. de Haas, and P. Dorenbos, "Nonproportional response between 0.1–100 kev energy by means of highly monochromatic synchrotron x-rays", *IEEE Transactions on Nuclear Science*, vol. 57, no. 3, pp. 1175–1181, 2010. DOI: 10.1109/TNS.2010.2045511.

[78] K. Kamada *et al.*, "Cz grown 2-in. size Ce:Gd3(Al,Ga)5O12 single crystal; Relationship between Al, Ga site occupancy and scintillation properties", vol. 36, Elsevier B.V., 2014, pp. 1942–1945. DOI: 10.1016/j.optmat.2014.04.001.

[79] A. Belsky *et al.*, "Mechanisms of luminescence decay in yag-ce,mg fibers excited by - and x-rays", *Optical Materials*, vol. 92, pp. 341–346, Jun. 2019. DOI: 10.1016/j.optmat.2019.04.054.

[80] S. Gundacker and A. Heering, "The silicon photomultiplier: Fundamentals and applications of a modern solid-state photon detector", *Physics in Medicine & Biology*, vol. 65, no. 17, 17TR01, 2020. DOI: 10.1088/1361-6560/ab7b2d.

[81] S. Gundacker, A. Knapitsch, E. Auffray, P. Jarron, T. Meyer, and P. Lecoq, "Time resolution deterioration with increasing crystal length in a tof-pet system", *Nuclear Instruments and Methods in Physics Research Section A: Accelerators, Spectrometers, Detectors and Associated Equipment*, vol. 737, pp. 92–100, 2014. DOI: https://doi.org/10.1016/j.nima.2013.11.025.

[82] V. Alenkov *et al.*, "Irradiation studies of a multi-doped gd3al2ga3o12 scintillator", *Nuclear Instruments and Methods in Physics Research, Section A: Accelerators, Spectrometers, Detectors and Associated Equipment*, vol. 916, pp. 226–229, Feb. 2019. DOI: 10.1016/j.nima.2018.11.101.

[83] R.-Y. Zhu, "A very compact crystal shashlik electromagnetic calorimeter for future hep experiments", *Journal of Physics: Conference Series*, vol. 928, no. 1, p. 012 015, 2017. DOI: 10.1088/1742-6596/928/1/012015.

[84] L. Martinazzoli *et al.*, "Compositional engineering of multicomponent garnet scintillators: Towards an ultra-accelerated scintillation response", *Mater. Adv.*, vol. 3, pp. 6842–6852, 17 2022. DOI: 10.1039/D2MA00626J.

[85] A. Belsky, A. Gektin, and A. N. Vasil'ev, "Influence of disorder in scintillating solid solutions on thermalization and recombination of electronic excitations", *physica status solidi (b)*, vol. 257, no. 8, p. 1 900 535, 2020. DOI: https://doi.org/10.1002/pssb.201900535.

[86] V. Babin, P. Herman, M. Kucera, M. Nikl, and S. Zazubovich, "Effect of Mg2+ co-doping on the photo- and thermally stimulated luminescence of the (Lu,Gd)3(Ga,Al)5O12:Ce epitaxial films", *Journal of Luminescence*, vol. 215, p. 116 608, 2019. DOI: https://doi.org/10.1016/j.jlumin.2019.116608.

[87] V. Babin, P. Boháček, K. Jurek, M. Kučera, M. Nikl, and S. Zazubovich, "Dependence of Ce3+ - related photo- and thermally stimulated luminescence characteristics on Mg2+ content in single crystals and epitaxial films of Gd3(Ga,Al)5O12:Ce,Mg", *Optical Materials*, vol. 83, pp. 290–299, 2018. DOI: https://doi.org/10.1016/j.optmat.2018.05.087.

[88] A. Gektin and A. Vasil'ev, "Scintillator energy resolution and a way to improve it by kinetic waveform analysis", *Radiation Measurements*, vol. 122, pp. 108–114, 2019. DOI: https://doi.org/10.1016/j.radmeas.2019.02.004.

[89] M Nikl *et al.*, "Decay kinetics of Ce3+ ions under gamma and KrF excimer laser excitation in CeF3 single crystals", *Journal of Physics: Condensed Matter*, vol. 7, no. 31, p. 6355, 1995. DOI: 10.1088/0953-8984/7/31/018.

[90] V. Pankratova *et al.*, "Radiation effects in Gd3(Al,Ga)5:O12:Ce3+ single crystals induced by swift heavy ions", *Optical Materials: X*, vol. 16, p. 100 217, 2022. DOI: https://doi.org/10.1016/j.omx.2022.100217.

[91] Kuraray, *Plastic scintillating fibres*, https://www.kuraray.com/products/psf, Accessed in December 2022.

[92] M. Bowen, S. Majewski, D. Pettey, J. Walker, R. Wojcik, and C. Zorn, "A new radiation-hard plastic scintillator", *Nuclear Instruments and Methods in Physics Research Section A: Accelerators, Spectrometers, Detectors and Associated Equipment*, vol. 276, no. 1, pp. 391–393, 1989. DOI: https://doi.org/10.1016/0168-9002(89)90657-8.

[93] A. Quaranta *et al.*, "Radiation hardness of polysiloxane scintillators analyzed by ion beam induced luminescence", *Nuclear Instruments and Methods in Physics Research Section B: Beam Interactions with Materials and Atoms*, vol. 268, no. 19, pp. 3155–3159, 2010, Radiation Effects in Insulators. DOI: https://doi.org/10.1016/j.nimb.2010.05.077.

[94] T. Marchi *et al.*, "Optical properties and pulse shape discrimination in siloxane-based scintillation detectors", *Scientific Reports*, vol. 9, no. 1, p. 9154, 2019. DOI: 10.1038/s41598-019-45307-8.

[95] A. Quaranta *et al.*, "Characterization of polysiloxane organic scintillators produced with different phenyl containing blends", *Materials Chemistry and Physics*, vol. 137, no. 3, pp. 951–958, 2013. DOI: https://doi.org/10.1016/j.matchemphys.2012.10.041.

[96] L. An *et al.*, "Performance of a spaghetti calorimeter prototype with tungsten absorber and garnet crystal fibres", *Nuclear Instruments and Methods in Physics Research Section A: Accelerators, Spectrometers, Detectors and Associated Equipment*, vol. 1045, p. 167 629, 2023. DOI: https://doi.org/10.1016/j.nima.2022.167629.

[97] A. Abada *et al.*, "FCC-hh: The Hadron Collider: Future Circular Collider Conceptual Design Report Volume 3", *Eur. Phys. J. ST*, vol. 228, no. 4, pp. 755–1107, 2019. DOI: 10.1140/epjst/e2019-900087-0.

[98] R. Alemany *et al.*, "Summary Report of Physics Beyond Colliders at CERN", J. Jaeckel, M. Lamont, and C. Vallée, Eds., Feb. 2019.

[99] S. Jindariani *et al.*, "Promising Technologies and R&D Directions for the Future Muon Collider Detectors", Mar. 2022.

[100] M. Aleksa, F. Bedeschi, R. Ferrari, F. Sefkow, and C. G. Tully, "Calorimetry at FCC-ee", *The European Physical Journal Plus*, vol. 136, no. 10, p. 1066, 2021. DOI: 10.1140/epjp/s13360-021-02034-2.

[101] R. Diener *et al.*, "The DESY II test beam facility", *Nuclear Instruments and Methods in Physics Research Section A: Accelerators, Spectrometers, Detectors and Associated Equipment*, vol. 922, pp. 265–286, 2019. DOI: https://doi.org/10.1016/j.nima.2018.11.133.

[102] D. Stricker-Shaver, S. Ritt, and B. J. Pichler, "Novel Calibration Method for Switched Capacitor Arrays Enables Time Measurements With Sub-Picosecond Resolution", *IEEE Transactions on Nuclear Science*, vol. 61, no. 6, pp. 3607–3617, 2014. DOI: 10.1109/TNS.2014.2366071.

[103] D. Gedcke and W. McDonald, "A constant fraction of pulse height trigger for optimum time resolution", *Nuclear Instruments and Methods*, vol. 55, pp. 377–380, 1967. DOI: https://doi.org/10.1016/0029-554X(67)90145-0.

[104] L. Martinazzoli, "Crystal Fibers for the LHCb Calorimeter Upgrade", *IEEE Transactions on Nuclear Science*, vol. 67, no. 6, pp. 1003–1008, 2020. DOI: 10.1109/TNS.2020.2975570.

[105] S. Perazzini, F. Ferrari, V. M. Vagnoni, and on behalf of the LHCb ECAL Upgrade-2 R&D Group, "Development of an MCP-Based Timing Layer for the LHCb ECAL Upgrade-2", *Instruments*, vol. 6, no. 1, 2022. DOI: 10.3390/instruments6010007.

[106] N. Akchurin *et al.*, "Electron detection with a dual-readout calorimeter", *Nuclear Instruments and Methods in Physics Research Section A: Accelerators, Spectrometers, Detectors and Associated Equipment*, vol. 536, no. 1, pp. 29–51, 2005. DOI: https://doi.org/10.1016/j.nima.2004.06.178.

[107] N. S. Kozlova *et al.*, "Optical characteristics of single crystal $Gd_3Al_2Ga_3O_{12}$: Ce", *Modern Electronic Materials*, vol. 4, no. 1, pp. 7–12, 2018. DOI: 10.3897/j.moem.4.1.33240.

[108] *LHCb ECAL UII simulation repository*, https://gitlab.cern.ch/spacal-rd/spacal-simulation, Accessed: 2023-01-30.

[109] M. Janecek and W. W. Moses, "Simulating scintillator light collection using measured optical reflectance", *IEEE Transactions on Nuclear Science*, vol. 57, no. 3, pp. 964–970, 2010. DOI: 10.1109/TNS.2010.2042731.

[110] A. Levin and C. Moisan, "A more physical approach to model the surface treatment of scintillation counters and its implementation into detect", in *1996 IEEE Nuclear Science Symposium. Conference Record*, vol. 2, 1996, 702–706 vol.2. DOI: 10.1109/NSSMIC.1996.591410.

[111] M Clemencic *et al.*, "The LHCb Simulation Application, Gauss: Design, Evolution and Experience", *Journal of Physics: Conference Series*, vol. 331, no. 3, p. 032 023, 2011. DOI: 10.1088/1742-6596/331/3/032023.

[112] I Belyaev *et al.*, "Handling of the generation of primary events in Gauss, the LHCb simulation framework", *Journal of Physics: Conference Series*, vol. 331, no. 3, p. 032 047, 2011. DOI: 10.1088/1742-6596/331/3/032047.

[113] W. Cleland and E. Stern, "Signal processing considerations for liquid ionization calorimeters in a high rate environment", *Nuclear Instruments and Methods in Physics Research Section A: Accelerators, Spectrometers, Detectors and Associated*

Equipment, vol. 338, no. 2, pp. 467–497, 1994. DOI: https://doi.org/10.1016/0168-9002(94)91332-3.

[114] G. Bonomelli, "Study of spatial and Angular Resolution of SPACAL Prototypes for the LHCb ECAL Upgrade II", Presented 05 Jul 2022, 2022.